Journal Homepage : http://dergipark.gov.tr/ejens
EJENS
European Journal of Engineering and Natural Sciences
CODEN: EJENS
DergiPark AKADEMİK

Removal of Ammonium Nitrogen from the DAF-Pretreated Poultry Slaughterhouse Wastewater by *Lemna minor*

F. Ilter Turkdogan[1]*, Kaan Yetilmezsoy[1], Bulent I. Goncaloglu[1], Necmiye Keskintimur[1], Melike Gungordu[1], Cagri Akyol[1]

[1]*Yildiz Technical University, Department of Environmental Engineering, 34220, Esenler/Istanbul, Turkey.*

**Corresponding Author e-mail: ilter@yildiz.edu.tr*

Abstract

In this study, ammonium, COD, color and turbidity removal with using *Lemna minor* (duckweed) was searched in Poultry Slaughterhouse (PS) wastewaters. Reason of Poultry Slaughterhouse Wastewaters (PSW) contains high concentration of organic compounds, ammonia and fats. Wastewater was taken from effluent of Dissolved Air Flotation (DAF) unit, then using MAP process, upper phase was given to reactor which *Lemna minor* was being. COD, ammonia, color, turbidity parameters were analyzed after hydraulic retention time of 7 days. The result of the study showed that *Lemna minor* is effective in treatment of poultry slaughterhouse wastewaters. In this study especially ammonia removal was investigated. At the same time COD, color and turbidity removal were researched. In this study, ammonia removal efficient was around % 30.08 ± 4.67, *Lemna minor* was effective in COD, color and turbidity removal as 26.58 ± 8.35; 35.06 ± 15:20; and 51.07 ± 18.77 respectively removal.

Key words

Lemna minor (duckweed), Poultry slaughterhouse wastewater

1. INTRODUCTION

The poultry slaughtering industry has enormous economic importance as the quickly developed among Turkey's other industries. According to the Ministry of Food, Agriculture and Livestock, consumption has grown from 10.5 kg/person in 2002 to 20.3 kg/person in 2015 [1].

The poultry slaughtering industries generate large volume of wastewaters containing very high concentrations of organic matter [2] and [3]. Slaughterhouse wastewaters contain different kinds of chemical substances, including dissolved organic compounds and total suspended solids (TSS) including fat, grease, feather, manure, flesh, grit, hair, and undigested feed as well [4] and [5]. Slaughterhouse wastewaters contain high concentrations of ammonia with many pollutants and direct discharge of these waters cause serious environmental problems. Discharge of such wastewater leads to undesirable aquatic growth and eutrophication. For this reason, these wastewaters should be given receiving conditions after the appropriate criteria are provided according to the characteristics and legislation to be discharged by the treatment.

Biological processes are economical and effective in this type of wastewater treatment. But it needs large area and long hydraulic retention time. Physico-chemical treatments are sometimes preferred for some wastewater treatment, due to the shorter hydraulic retention time. Physico-chemical processes such as dissolved air flotation (DAF) and coagulation–flocculation (CF) are widely used for the removal of TSS, colloids, and fats from slaughterhouse wastewaters [6]. In PS wastewaters, which are also very rich in nitrogen concentration, lowering nitrogen concentrations can prevent possible eutrophication problems in the receiving environment. If PS wastewater is kept in "polishing units" as *Lemna minor* pools in the last stage of the process, nitrogen levels could be decreased to much lower levels. Duckweed is a low-cost process and efficient method for the treatment of water and wastewater. The purpose of this work is to use duckweed in treating poultry slaughterhouse wastewater after DAF and MAP process. Purification mechanisms such as sedimentation, adsorption, bacterial decomposition and vegetal use are effective in the treatment process with water plants. Organic matter removal is increased by providing surface area for both oxygen and bacterial growth by *Lemna minor* [7]. Ammonium is the primary source of nitrogen in *Lemna minor* [8]. Earlier studies have shown the possibility of simultaneously removing of TSS, BOD and COD from slaughterhouse wastewaters. It was tested successfully removal rate of NH4 and COD 41-48% and 17-20%, respectively [9]. In another study conducted with urban wastewater, the COD removal rates in three parallel units were 61%, 72% and 63%, respectively and TSS removal rate of 82% and 80% was observed [10]. Reference [8] investigated *Lemna minor* activity was at laboratory scale in the treatment of campus wastewater. The last settling basin in *Lemna minor* was compared to the last settling basin in which there is no *Lemna minor* basin. In the last sedimentation pool located in *Lemna minor*; COD removal yield was found to be 15%, BOD5 removal yield 25%, ammonium removal yield 35%, and phosphate removal yield 45% higher [11]. Although studies have been carried out to remove a wide range of wastewater with *Lemna minor*, there is not yet a study in the literature on PS wastewater.

In the present work, *Lemna minor* was used to treat the polishing units and to remove the fine oxide particles. Experimental conditions of the process and effluent wastewater quality before and after treatment were determined. The main objective of the present study was to examine the feasibility of *Lemna minor* after the DAF unit process in treating PS effluent before discharge into urban sewer.

2. MATERIALS AND METHODS

2.1. Characterization of PS Wastewater

PS wastewater was obtained from a local poultry processing plant (Mudurnu Pilic) located in Dilovasi, Izmit (TURKEY). The wastewater samples were taken from the effluent of the dissolved air flotation (DAF) unit at the poultry processing plant (Table 1).

Table 1. Characteristics of the DAF pretreated PSW

Constituent	**Value (mean ± S.D.)**
Total Chemical Oxygen Demand, TCOD (mg/L)	1032.57 ± 5.35
Volatile Suspended Solids, VSS (mg/L)	49 ± 17.4
Total Suspended Solids, TSS (mg/L)	58 ± 15.63
Alkalinity (mg $CaCO_3$/L)	205 ± 12.8
Ammonium Nitrogen, NH_4^+-N (mg/L)	123.75 ± 4.23
pH	7.1 ± 0.20

2.2. $MgNH_4PO_4.6H_2O$ (MAP) Precipitation Tests

Due to high NH_4^+-N and COD in PS wastewater may causes some toxic effect on the *Lemna minor*, in order to the toxic effect was studied MAP precipitation. After the precipitation of the MAP, the values of COD 300-350 mg/L and NH_4^+-N 60-70 mg /L were obtained.

Amounts of chemicals used to precipitate the ammonium nitrogen in the wastewater of slaughterhouse in MAP form were determined according to Equations (1) - (3) and as a source of magnesium and phosphate were added to the PSW at stoichiometric ratio (Mg^{2+}: NH_4^+-N: PO_4^{3-} P = 1: 1: 1).

$$MgCl_2.6H_2O + KH_2PO_4 + NH_4^+ \rightarrow MgNH_4PO_4.6H_2O^- + K^+ + 2Cl^- + 2H^+ \quad (1)$$

$$MgSO_4.7H_2O + Na_2H_2PO_4.2H_2O + NH_4^+ \rightarrow MgNH_4PO_4.6H_2O^- + Na^+ + SO_4^{2-} + 2H^+ + 7H_2O \quad (2)$$

$$MgOHCO_3 + 85\%\, H_3PO_4 + NH_4^+ \rightarrow MgNH_4PO_4.6H_2O^- + H_2O + HCO_3^- \quad (3)$$

2.3. *Lemna minor*

Lemna minor was collected from Istanbul University Botanical Garden, Istanbul-Turkey (Figure 1). Working with the *Lemna minor* plant was started immediately, but it was kept in a container with the original water for one day before starting to work.

Figure 1. Image of Lemna minor with stereomicroscope (Prior-James Swift, 240V.AC, F80 mA)

2.4. Analytical Procedure

The pH of wastewater samples was measured by a pH meter (Jenway 3040 Ion Analyser). Ammonium nitrogen (NH_4^+-N), total chemical oxygen demand (TCOD), total suspended solids (TSS), volatile suspended solids (VSS), and alkalinity were conducted by the procedures described in the Standard Methods [12]. Samples were ignited at 550°C by using an ashing furnace (Lenton) for VSS analyses. Absorbance values were recorded at 425 nm by using a spectrophotometer (Pharmacia Biotech LKB Novaspec® II) for NH_4^+-N analysis. Color and Turbidity were measured by the HACH LANGE DR5000 spectrometer.

2.5. System Design

In the study, a reactor with a volume of 6 L and an active volume of 5.6 L was used from Plexiglas material. A weir structure has been placed between the wastewater so that the wastewater can be delivered equally to the system. Sluice was placed in order to ensure mixing and better distribution in the reactor. At the exit of the reactor, a wire plate was placed in the outlet pipe to prevent the *Lemna minor* escaping. During the study conducted under this work, a modulated fluorescent lamp (Panlight daylight lamps, 3011 T8 36W) was used as artificial light in the cultivation experiment setting. The system was operated in a daily continuous mode by feeding with a SEKO® peristaltic pump. Hydraulic retention time (HRT) was set to 7 days for reactor. A detailed schematic of the experimental set-up is depicted in Fig. 2.

Fig.2. A detailed schematic of the experimental set-up.

3. RESULTS AND DISCUSSION

3.1 NH_4^+-N and COD Removal of MAP

Table 2 shows the NH_4^+-N and COD values obtained as a result of MAP sedimentation in the samples taken from the DAF unit of slaughterhouses wastewater.

Table 2. NH_4^+-N and COD values of MAP

Parameter	***MAP Inffluent***	***MAP Effluent***	***Removal Rate %***
NH_4^+-N	*123.75±4.23*	*83,6±23,1*	*32.44±3.97*
COD	*1032.57±5.35*	*348,1±40*	*66.29±2.58*

3.2. NH_4-N, COD, Color and Turbidity Removal of Lemna Minor

Table 3 shows the NH_4^+-N, COD, color and Turbidity values after *Lemna minor.*

Table 3. NH_4^+-N, COD, Color and Turbidity values of Lemna Minor

Parameter	***Inffluent***	***Effluent***	***Removal Rate %***
COD	*348,1±40*	*255.57±25.07*	*26.58±8.35*
NH_4^+-N	*83,6±23,1*	*58.45±5.06*	*30.08±4.67*
Color	*72.83±12.29*	*24.33±16.62*	*35.06±15.20*
Turbidity	*25.01±2.72*	*12.22±4.54*	*51.07±18.77*

4. CONCLUSIONS

High ammonia concentrations are a problem for wastewater if the receiving environment standards are low. This type of wastewater needs to be well treated before the discharge. Existing methods add cost in the treatment plants. Low-cost systems added to the output of existing plants are getting interest. The use of *Lemna minor* pools, which is a natural method, provides an important treatment without energy cost. With this study, it was demonstrated that *Lemna minor* pools can be used as a "polishing" step.

ACKNOWLEDGEMENTS

The authors would like to thank Istanbul University Botanical Garden, Istanbul-Turkey for supplying the *Lemna minor* used in this work.

REFERENCES

[1]. (2016) Webpage on Republic of Turkey Ministry of Food, Agriculture and Livestock, (online): available: https://www.tarimorman.gov.tr/Konular/Hayvancilik/Kanatli-Yetistiriciligi TÜRKİYE VE DÜNYADA KANATLI SEKTÖRÜNÜN GENEL DURUMU-2018.doc

[2]. Quinn J.M. and McFarlene P.N., "Effects of Slaughterhouse and Dairy Factory Wastewaters on Epilithon: a Comparison in Laboratory Streams", *Water Research*, Vol.23(10), pp. 1267–1273, 1989.

[3]. Sandogoyin A.D and Agbawhe O.M., "Environmental Study on Surface and Ground Water Pollutants from Slaughterhouse Effluents", *Bioresource Technology*, Vol.41, pp.193–200, 1992.

[4]. Bull M.A. , Sterritt R.M. , Lester J.N. ,"The Treatment of Wastewaters from the Meat Industry: a Review", *Environ. Technol. Lett*., 3, pp. 117–126, 1982.

[5]. Tritt W.P. and Schuchardt F., "Materials Flow and Possibilities of Treating Liquid and Solids from Slaughterhouses in Germany", *Bioresour. Technol*., Vol.41, pp. 235–245, 1992.

[6]. Masse D. and Masse L., "The Effect of Temperature on Slaughterhouse Wastewater Treatment in Anaerobic Sequencing Batch Reactors", *Bioresource Technology*, Vol.76 (2), pp. 91–98, 2000.

[7]. Körner S. and Vermaat, J.E., "The Relative Importance of *Lemna Gibba L.*, Bacteria and Algae for the Nitrogen and Phosphorus Removal in Duckweed-Covered Domestic Wastewater", *Water Res.*, Vol.32 (12), pp. 3651–3661, 1998.

[8]. Yılmaz Z., Gür K. ve Tarlan E., "Atıksularının Karakterizasyonu ve Su Mercimeği ile Arıtılabilirliği", *S.Ü.Müh.-Mim.Fak.Dergisi*, Cilt: 20, Sayı:4, Konya, 2005.

[9]. Oron, G. vd., "Performence of the Duckweed Species *Lemna gibba* on Municipal Wastewater for Effluent Renovation and Protein Production", *Biotech. And Bioeng*., Vol.29 (2), pp. 258–268, 1987.

[10]. Mandi L., "Marrakesh Wastewater Purification Experiment Using Vascular Aquatic Plants *Eichhornia crassipes* and *Lemna gibba*", *Water Science and Technology*, Vol.29 (4), pp. 283–287, 1994.

[11]. Gürtekin E., Şekerdağ N., "Son Çökeltme Havuzlarında Su mercimeğinin (*Lemna Minor L.*) Rolü", *SAÜ. Fen Bilimleri Dergisi,* Cilt:12 (1), Syf: 28–31,Elazığ, 2008.

[12]. American Public Health Association (APHA), *Standard Methods for the Examination of Water and Wastewater*, 21st Ed., Washington, DC, 2005.

Journal Homepage : http://dergipark.gov.tr/ejens
EJENS
European Journal of Engineering and Natural Sciences
CODEN: EJENS
DergiPark AKADEMİK

The Abrasion Resistance of Mortars Containing Natural Zeolite Analcime

Yasemin Akgün[1*], Ömer Fatih Yazıcıoğlu[2]
[1] *Ordu University, Department of Renewable Energy, 52200, Ordu, Turkey.*
[2] *Ondokuz Mayıs University, Department of Civil Engineering, Samsun, Turkey.*
**Corresponding Author email: yakgun@odu.edu.tr*

Abstract

It is always an expectation that to minimize of damage caused by abrasion as a result of increase of abrasion resistance of construction materials. Therefore, the influence of analcime on the abrasion resistance of cement mortars was investigated in this study. Analcime is a natural pozzolan and is one of the valuable minerals of zeolite group. The cement mortars were produced by using blended cements containing analcime. The abrasion losses by friction at the end of 28 days of the mortar mixtures were determined by Bohme surface abrasion tests in accordance with TS 2824 EN 1338. The abrasion tests were carried out to cement mortar mixtures produced with different cement replacement ratio (0%, 10%, 30% and 50%). The results obtained from test series were compared with each other. The test results showed that, abrasion losses of mortars containing analcime were lower than portland cement mortars as 25% approximately. It is believed that this positive effect of natural zeolite in the development of abrasion resistance is due to pozzolanic reactions.

Key words

Abrasion, Analcime, Mortar, Natural Zeolite.

1. INTRODUCTION

Natural zeolites have recently become widely used as additive material in blended cement productions. Because, natural zeolites are pozzolanic materials containing abundant amounts of silica and alumina. When zeolite is replaced with clinker at optimum ratio, they form additional binder components by reacts with Ca $(OH)_2$ which is a result of cement hydration. These additional binders improve strength and durability of mortar/concrete. It is obtained advantages such as reducing of CO_2 emissions, energy saving and economy according as reducing of clinker consumption in blended cement applications containing zeolite. Also, natural zeolites are preferred to synthetic zeolites because of their reserve and economic status. The natural zeolites formed by the alteration of the vitric pyroclastic deposits are more reactive materials than the fly ash and furnace slags between mineral additives [1]. Natural zeolites have reserve declared as hundred billions tons in the world [2]. The using of these zeolite reserves will be possible with investigation performed on different zeolite minerals. Analcime is a natural pozzolan and is one of the valuable minerals of zeolite group. Analcime is a feldspathite mineral with a very large amount of hydrated sodium aluminosilicate (Na $(AlSi_2O_6).H_2O$) in its structure.

Abrasion is a physical and mechanical event that is slowly occurred. The reduction in size and mass occurred by friction of abrasive materials on surfaces of objects that make contact with each other and move relative to each other is defined as abrasion loss. Generally, the amount of abrasion depends on type of material, state of abrasion surface, friction conditions and chemical effects of environment.

As a result of optimizations carried out on all of mortar/concrete components, it is known that the abrasion resistance can be increased to desired level. Therefore, it can be possible to minimize damages caused from

abrasion with increasing properly of abrasion resistance of mortar/concrete in some cases such as pavement, concrete roads, factory floor surfaces, water structures, chimneys etc.

In literature, the study made with analcime is very limited [3, 4, 5]. Furthermore, there is no study to examine abrasion resistance on mortar or concrete samples containing analcime. It is always an expectation that to minimize of damage caused by abrasion as a result of increase of abrasion resistance of construction materials. Therefore, the influence of analcime on the abrasion resistance of cement mortars was investigated in this study. The abrasion tests were carried out on mortar mixtures produced with different cement replacement ratio (0%, 10%, 30% and 50%). And, pozzolanic activity of analcime were determined. The results are compared with each other.

2. MATERIALS AND METHODS

The cement used in tests is CEM I 42.5 R type of Portland cement (PC) produced in accordance with TS EN 197-1 [6]. The analcime were used as replaced material by cement. The analcime (A) that is type of natural zeolite were obtained from Ordu/Perşembe regions of Turkey. The analcime samples were finely grinded in a ball mill. The amount of analcime used in mixtures were 0%, 10%, 30% and 50% of cement weight. So, the mixtures were produced with the labels PC, A10, A30 and A50.

The CEN (The European Committee for Standardization) standard sand in accordance with EN 196-1 [7] was used in mortar mixtures. The sand-to-cement ratio is constantly 3 and water-to-cement ratio is constantly 0.5. It was used superplasticizer (at 1%, 1.5% and %2 ratios) complying with TS EN 934-2 [8] by adding to mixture water to recover of adverse effect on mortar consistency of natural zeolites in mixtures. In the production of all samples, water that does not contain organic substances and mineral salts that may be harmful is used. The flow values of mortar mixtures are about 150 ± 20 mm.

All mortar mixtures were prepared by applying the standard mixing, molding and curing procedures stated in TS 196-1. Samples was prepared in laboratory environment where temperatures are 20±2ºC and relative humidity is 60±5%. The samples taken from molds after 24 hours from their productions were kept in the curing tank at a temperature of 21 ± 1ºC until the test days.

X-Rays Fluorescence Spectrometer (XRF) analysis was performed to determine chemical composition of analcime. X-Ray Diffraction (XRD) analysis was performed to determine mineralogical composition of analcime. Some views were also obtained using a Scanning Electron Microscope (SEM).

2.1 Test of Pozzolanic Activity

Pozzolanic activity can be defined as the ability to react with $Ca(OH)_2$ of active silica which is in the pozzolan. At the end of this reaction the amount of portlandite ($Ca(OH)_2$) is reduced, calcium silicate hydrate (CSH) is increased.

The pozzolanic activity tests were performed on 40x40x160mm prismatic samples. In TS 25 [9], the pozzolanic activity test is defined as a characteristic determined in terms compressive strength of the mortar obtained by mixing natural pozzolan which is grinded at a certain fineness with water, standard sand and calcium hydroxide (CaOH2). The amounts of materials required to prepare three test samples for tests on pozzolanic activity are given in Table 1.

Table 1. The amounts of materials for tests on pozzolanic activity

Materials	TS 25	The amounts for tests
Slaked lime ($CaOH_2$)	150gr	150gr
Pozzolan	2x150x(density of pozzolan /density of $CaOH_2$) (gr)	2x150x(2.28/2.15) = 318.14gr
Standard sand	1350gr	1350gr
Water	0.5x (150+pozzolan) (gr)	0.5x(150+318.14) = 234.07gr

The moulds of the prepared samples were covered with a glass plate to prevent evaporation. The samples were allowed to stand at room temperature for 24 hours (23 ± 2)ºC. And then, they were left for 6 days in an drying oven at 55 ± 2°C without removing the moulds. The samples removed from the oven were left to cool until the room temperature reached. Finally, the compressive strengths of samples were performed in accordance with TS EN 196-1.

2.2 Test of Abrasion Resistance

Three cube moulds of 70.7 mm were used for each mixture in abrasion tests. The mortars were produced by using blended cements containing analcime. The abrasion losses by friction at the end of 28 days of the mortar samples were determined by Bohme surface abrasion tests in accordance with TS 2824 EN 1338 [10] (Fig. 1).

Before tests, initial volumes and initial weights of samples were determined. The abrasive force of 294 N was applied to samples placed on rotary disk of Bohme apparatus.

The samples were subjected to abrasive effect of 20 g corundum powder poured on friction path together with operation of device. Total of 16 periods that each of them is 22 cycles were applied to samples. At the end of the test (at the end of the 352 cycles), volumetric abrasion losses (ΔV) in samples were determined.

In calculations, it was used formula at (1) which denote ΔV (cm^3/50 cm^2); volumetric abrasion loss, Δm (gr); weight loss at end of 16 cycles, ρ (g/cm^3); density.

$$\Delta V = \Delta m / \rho \quad (1)$$

Figure 1. Bohme abrasion test device

3. RESULTS AND DISCUSSION

3.1. Some properties of portland cement, analcime and blended cements

Some properties of portland cement (PC), analcime (A), blended cements (A10, A30 and A50) are presented in Tables 2, 3 and 4. Densities of analcime is 26.92% lower than PC. Specific surface area of analcime is 48.91% higher than PC. This situation depends on mineral structure, porosity and fragilement properties of zeolite. Cumulative passing (%) of 45 μm sieve for Portland cement and analcime are 67.11% and 70.80%, respectively. Densities of blended cements have decreased with increasing of zeolite ratios. Fineness of blended cements containing zeolite has increased with increasing of zeolite ratios.

Table 2. Properties of portland cement (PC).

Chemical composition	**(wt.%)**	**Physical and mechanical properties of portland cement**			
SiO_2	19.53	Density, (g/cm^3)	3.12		
Al_2O_3	5.33	Initial set, (h)	2.50		
Fe_2O_3	3.56	Final set, (h)	4.15		
CaO	62.26	Volume expansion, mm	2.00		
MgO	0.99	Specific surface (Blaine) (cm^2/g)	3210		
SO_3	3.02	The compressive strengths	2 days	7 days	28 days
Loss of ignition	3.06	(MPa)	32.30	44.60	53.00
		Over sieve	45μm	90 μm	200 μm
		(%)	32.89	12.15	2.73

Table 3. Properties of analcime

Chemical composition	**Analcime (wt.%)**	**Physical properties**	
SiO_2	46.71		Analcime
Al_2O_3	17.24	Density, (g/cm^3)	2.28
Fe_2O_3	9.21	Blaine fineness (cm^2/g)	4780
CaO	3.03		
MgO	5.29	Over sieve (%)	
Na_2O	4.84	45μm	29.20
K_2O	4.08	90 μm	9.80
Loss of ignition	7.00	200 μm	2.15

Table 4. Properties of blended cements

Physical properties	PC	A10	A30	A50
Specific surface (cm^2/g) (Blaine fineness)	3210	3752	3918	4449
Density, (gr/cm^3)	3.12	2.79	2.75	2.71

3.2 Pozzolanic Activity of Analcime

Pozzolanic activity of analcime are given in Table 5. According to Table 5. In TS 25, one of the conformity criterias for pozzolans is the 7 day compressive strength of samples prepared with lime-natural pozzolan mixture. The limit value of the compressive strength is at least 4 MPa. In test study performed for analcime, the average compressive strength value for the lime-zeolite (pozzolan) mixture samples was determined as 6.30MPa. It has also been emphasized that the sum of SiO_2 + Al_2O_3 + Fe_2O_3 in TS 25 should be at least 70% by mass. The value of this total was found to be 73.16% for analcime. At the same time, the specific surfaces of the pozzolans should be greater than 3000 cm^2/gr. The specific surface of pozzolan which is used in this study were found to be 4780 cm^2/gr for analcime (Table 3). In pozzolanic activity tests. Because of the specific surface of natural zeolite were below of portland cement fineness, the reaction which is between pozzolan and lime was increased. It is thought that, this situation was lead to an increment at value of pozzolanic activity. These value show that the zeolite used in study have an usability potential as a pozzolan.

Table 5. Pozzolanic activity of analcime

TS 25 limit values	Analcime
Lime-pozzolan mixture 7 days compressive strength > 4MPa	6.30MPa
SiO_2+Al_2O_3+Fe_2O_3 wt. content >%70	%73.16
Specific surface area > 3000cm^2/gr	4780 cm^2/gr

3.3 Mineralogical Composition of Analcime

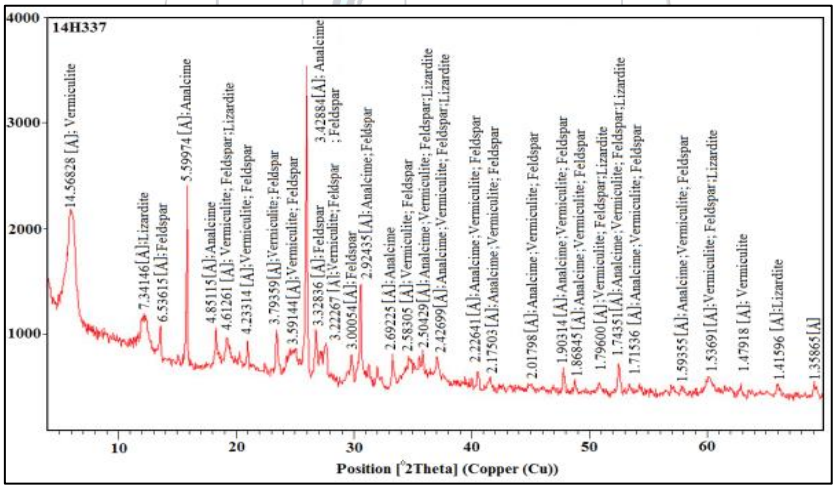

Figure 2. XRD diffraction patterns of analcime

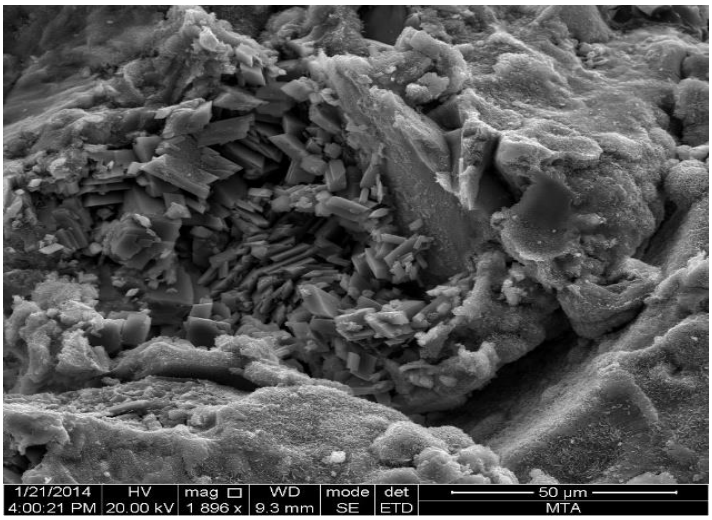

Figure 3. SEM view of analcime

XRD diffraction patterns and SEM views are presented in Figs. 2 and 3. According to the mineral modal ratios at the mineralogical composition results determined by the X-ray diffraction analysis (XRD) of analcime sample, the analcime rock is a vitric tuff and consists of glass splinters and crystal components. Glass splinters are converted to zeolite and chlorite, which are heavily altered. The analcime samples confirm the requirements of national and international standards for zeolite applications.

3.4 Abrasion Resistance of Mortars

Abrasion losses ΔV ($cm^3/50cm^2$) are given in Table 6. Abrasion losses variations for mortars are presented in Fig. 4.

Table 6. Volumetric abrasion losses and densities of mortar

Mortars	**PC**	**A10**	**A30**	**A50**
Density (gr/cm^3)	2.42	2.16	2.13	2.10
ΔV ($cm^3/50cm^2$)	11.84	8.97	9.17	10.23

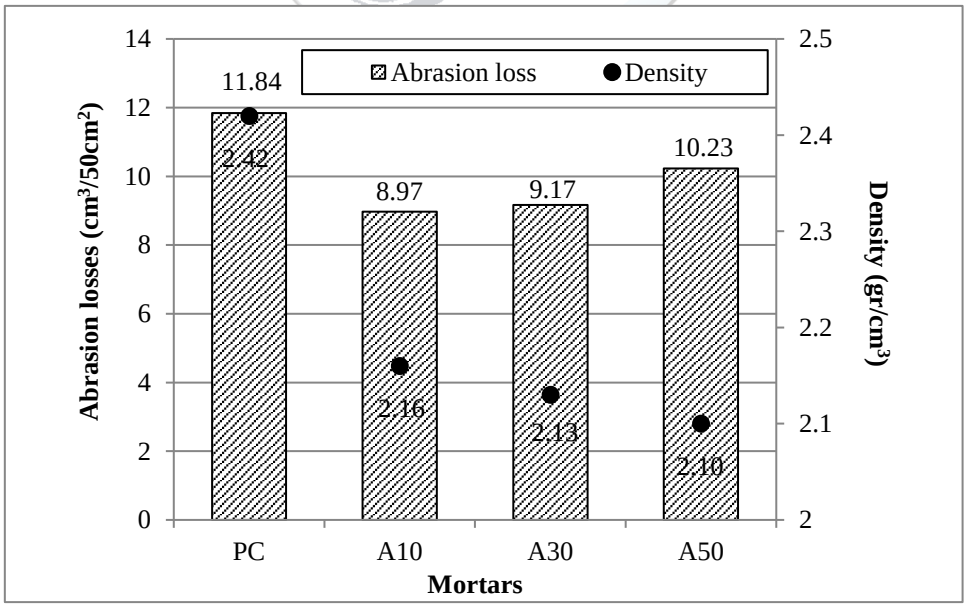

Figure 4. Abrasion loss and density variation for mortar

The volumetric abrasion losses for mortars with blended cements containing analcime (A10, A30 and A50) were 25%, 23% and 14% less than mortars with PC, respectively. In other words, it has been found that the abrasion losses of mortars with blended cement are less than mortars with PC for all replacement ratios. This positive effect

in abrasion resistance is probably performance increasing occurred at aggregate-cement paste interface and cement paste due to pozzolanic reactions of zeolite. Also, as analcime replacement ratio increases, the densities of mortars decrease.

4. CONCLUSIONS

1. Since the density of analcime is lower than that of Portland cement, the densities of mortars produced by blended cement containing analcime are less than that of mortars produced by Portland cement.

2. The properties of natural zeolite analcime investigated in this study such as pozzolanic activity, mineralogical structure, high silica-alumina content, high specific surface, low density are sufficient for sustainable blended cement productions.

3. The abrasion losses of mortars containing analcime were lower than that of mortars containing portland cement for all replacement ratios. In other words, abrasion resistances of mortars containing analcime has increased up to 30% replacement ratio. It is believed that this positive effect of natural zeolite in the development of abrasion resistance is due to pozzolanic reactions.

4. A larger number of studies should be carried out on zeolites named analcime obtained from different regions to reduce amount of cement and to improve of cement performance.

ACKNOWLEDGMENT

This study was funded by the Scientific Research Project Unit of Ordu University under Project No: TF-1521. Also, we would like to thanks to General Directorate Of Mineral Research And Explorations, Votorantim Cimentos, Mineralogy Laboratory of Blacksea Technical University, Gördes Zeolite Company for their support and assistance.

REFERENCES

[1]. Chan, SYN. and Ji, X. Comparative study of the initial surface absorption and chloride diffusion of high performance zeolite, silica fume and PFA concretes. Cem. Concr. Compos. 1999, 21:293–300.

[2]. Özen, S., Göncüoğlu, M. C., Liguori, B., Gennaro, B., Cappelletti, P., Gatt, G. D., Iucolano, F., and Colella, C., A comprehensive evaluation of sedimentary zeolites from Turkey as pozzolanic addition of cement- and lime-based binders", Construction and Building Materials, 2016, Vol: 105, 46-61.

[3]. Bilim, C., Zeolit Katkısının Harçların Aşınma Direncine Etkisi, 6th International Advanced Technologies Symposium (IATS'11), 2011, Elazığ, Turkey.

[4]. Gabriel C., Rajwant S. B., Yushan Y., and Junlan W., Zeolite as a wear-resistant coating, Microporous and Mesoporous Materials, 2012, vol: 151, 346–351.

[5]. Akgün, Y., and Yazıcıoğlu, Ö. F., İki Farklı Doğal Zeolit Katkısının Çimento Harç Aşınma Dayanımına Etkisi, Ordu Üniv. Bil. Tek. Derg., Cilt:6, Sayı:1, 2016,94-104.

[6]. TS EN 197–1, (2002), Çimento - Bölüm 1: Genel Çimentolar- Bileşim, Özellikler ve Uygunluk Kriterleri. Ankara: Türk Standartları Enstitüsü.

[7]. TS EN 196–1, (2009) Çimento Deney Metotları - Bölüm 1: Dayanım Tayini. Ankara: Türk Standartları Enstitüsü.

[8]. TS EN 934-2, (2013), Kimyasal Katkılar - Beton, Harç ve Şerbet için - Bölüm 2: Beton Kimyasal Katkıları - Tarifler, Gerekler, Uygunluk, İşaretleme ve Etiketleme, Ankara: Türk Standartları Enstitüsü.

[9]. TS 25, (2008), Doğal Puzolan (Tras)-Çimento ve Betonda Kullanılan-Tarifler, Gerekler ve Uygunluk Kriterleri. Ankara: Türk Standartları Enstitüsü.

[10]. TS 2824 EN 1338, (2005), Zemin Döşemesi için Beton Kaplama Blokları-Gerekli Şartlar ve Deney Metotları. Ankara: Türk Standartları Enstitüsü.

Journal Homepage : http://dergipark.gov.tr/ejens
EJENS
European Journal of Engineering and Natural Sciences
CODEN: EJENS
DergiPark AKADEMİK

An Image-based Recommender System Based on Image Annotation

Kemal Ozkan[1]*, Zuhal Kurt[2], Erol Seke[3]

[1]*Department of Computer Engineering, Eskişehir Osmangazi University, 26480, Eskişehir, Turkey.*

[2]*Department of Mathematics and Computer Science, Eskişehir Osmangazi University, 26480, Eskişehir, Turkey.*

[3]*Department of Electrical and Electronics Engineering, Eskişehir Osmangazi University, 26480, Eskişehir, Turkey.*

**Corresponding Author email: kozkan@ogu.edu.tr*

Abstract

Recommender system is a software that analyzes available data to make recommendations about various products and services to their users might be interested in. These systems must perform efficient for both users and the e-commerce sites benefiting from such systems. Ensuring proper and reliable recommendations increases user satisfaction that results selling more products and services. Recommendation algorithms can be categorized as collaborative filtering, content-based, and hybrid filtering techniques. Content-based recommendation algorithms are mostly used in text-based systems. However, image-based recommender systems have become increasingly in favour for the content-based recommender systems in recent years.

The process of an image based recommender system is to match a users' images with the most similar images and recommend them. The recommended images are the most likely/similar images that are uploaded and widely acclaimed by the users. The most challenging problem in image-based recommender systems is to match an image with the most similar visual words or classes based on the image's visual content. In this study, we are planning to solve this problem with utilizing bag of words model, which is an effective model in computer vision. Moreover, the visual features are extracted with commonly used descriptors for this model.

Key words

Bag of Words, Descriptor, Similar, Image-based Recommender System.

1. INTRODUCTION

The major aims of recommender systems are helping customers to find products which they seek, and the other one is increasing sales ratios for sellers. Therefore, success of recommender systems is imperative for both users and the e-commerce sites utilizing such systems. Providing accurate and dependable recommendations increases user satisfaction that results selling more products and services. On the other hand, inaccurate recommendations make users to search alternative sites for shopping. Recommender systems can be grouped as collaborative filtering, content-based, and hybrid recommender systems. Collaborative filtering is a common recommender system. In addition to collaborative filtering algorithms, content-based and hybrid recommender systems are increasingly becoming popular due to widespread use of social media. Generally, content-based recommendation algorithms are applied in text-based recommender systems. Recently, image-based recommender systems which utilizes content-based recommendation algorithms, are receiving increasing attention.

Although there are studies focusing on image-based recommender systems, such systems are still challenging research field with some unresolved problems. These systems are based on images uploaded by users. They first determine the most similar users based on the images, which are uploaded to the system by the users before. Then, these systems return the most likely images for the users based on the images liked by their neighbors. The most difficult problem in image-based recommender systems is to match an image with the most similar visual words or classes based on the image's visual content. In this paper, we are planning to solve this problem with using current image annotation techniques, which are effective methods in computer vision. Another challenging problem in image-based recommender systems is the online computation time caused by the large amount of data in real life applications.

An image-based recommender system is proposed that utilizes common image annotation techniques to solve these problems, [1]. This recommendation algorithm works with large collections of touristic images and the structure of this system is based on clustering and classification algorithms. Tourism related images have been annotated geographically, semantically, and visually with utilizing visual features and text data in the system. Then, this system utilizes annotated information to recommend a touristic place where the user can be interested in, [1].

A novel framework called JustClick [3] is a personalized image recommendation system working with large-scale collections of manually annotated Flickr images. The procedure of this system is based on topic networks, that are automatically produced for outlining large-scale collections of manually annotated Flickr images at a semantic level. This system used hyperbolic visualization method to enable interactive navigation and exploration of the topic network. Hence, users can find out the large-scale image collections at the first glance, build up their mental query models interactively and specify their image needs more precisely by selecting the image topics on the topic network directly. Moreover, users can assess the relevance between the recommended images and their real query intentions interactively. An implementation of this system is allowing users to express their time-varying query intentions and to direct the system to more relevant images according to their personal preferences [3].

A personalized recommender system model, that is based on analysis of color features of product images, is proposed in, [2]. This recommendation algorithm is based on colored-feature extraction of images in order to demonstrate impressions related to the human perception of images. This system retrieves and ranks the images corresponding to the desired impressions with utilizing extracted color features. The structure of this model is depend on service-oriented structure in order to promote its flexibility and reuse, that is important when implementing the model into other existing recommender system environments, [2].

A profile based image recommender system is proposed in [4, 5], and this system is able to reach a particular user for retrieval of images from profile based search engines by using smartphone. All users of this system have his/her own profile and semantic signature of each user search is stored individually. This approach improves the performance of search result as it is referring individual profile to know users search intension. The images are re-ranked using keyword expansion to provide better efficiency and effectiveness by using semantic signature for more precise output [4].

The feature extraction techniques are used in order to image annotation, the Color / Scale Invariant Feature Transform (SIFT / C-SIFT) [6,7], Speeded-Up Robust Features [8], Maximally Stable Extremal Regions(MSER) [9] and Local Binary Pattern (LBP) [10] frequently used descriptors, and also new approaches available in the literature. In this paper, we develop an image-based recommender system, and we use novel image annotation approaches to design this system. The proposed system needs to uploaded image from a particular user. These images become query images for our system, then these images are annotated to understand users' preferences. Outputs of the proposed system are recommendation images that are suitable for users' necessity/pleasure. The algorithm of the proposed method and the experimental results will be given in order of the second part and the third part of the study. Finally, the conclusion and future work will be given in section 4.

2. MATERIALS AND METHODS

There are two problems that might affect the overall success of recommender systems. These problems are known as sparsity and accuracy problems. To solve the sparsity problem, we are going to use image annotation techniques to get the image labels, and to construct visual vocabulary. Furthermore, the visual words help the image-based recommender system to collect data about the users, which might improve the accuracy of our recommender system. Contemporary recommender systems utilize GPS data and the labelled data of the collected images to provide recommendations. However, we design our system in such a way so that it will also use unlabeled data to estimate recommendations. At the end, the design of proposed image-based recommender system is based on visual words among images. The current approaches of feature extraction techniques are used to design the proposed image-based recommender system, such as SIFT, SURF, LBP. Overall performance of

the proposed system is evaluated in terms of accuracy and evaluated on a popular dataset. The algorithm of the proposed recommender system is given under below.

- Firstly, a user is prompted to upload the users' images to the proposed system.
- The commonly known feature extraction methods and the bag of Words (BoW) model are used in the proposed system.
- To extract features from the users' images, the popular SIFT, SURF and LBP descriptors are used. Moreover, the proposed system feeds by extracting features from the images in the system.
- In this proposed system, the same feature extraction techniques are applied to users' images, and these images are accepted as test set. Each extracted features from test images are compared to the other images features' in the system. Then top-10 images are recommended to the users.
- The selection opportunity from the recommended top-10 images is given to a user.
- Furthermore, the proposed recommender system is implemented on the Yahoo! shoes dataset, which is generated by Yahoo! Research Lab in 2012.

3. RESULTS AND DISCUSSION

The proposed system is implemented on the challenging Yahoo! Shopping Shoe dataset, [11]. As stated in [11], this dataset provides a new benchmark which contains a diverse collection of types of shoes photos. Object recognition algorithms aim to identify if there is a pair of shoe and the type of shoes (clogs or high heels) appear in a photo automatically. Yahoo! Shopping site is the best place to read user reviews, explore great products and buy online. Dataset is collected from a small subset of product from Yahoo! Shopping to reflect the interesting real-world problem of fine-grained object recognition. This dataset includes a small sample of the Yahoo! Shopping shoe photos. This dataset includes 107 folders, each folder is contained a type and a brand of shoes. Moreover this dataset includes a *.mat file (shoe_annos.mat), which contains a bounding box for each shoe image.

We use shoe annotation file to read images from Yahoo! Shopping Shoe dataset. This file (shoe_annos.mat), contains 4513 image file and a bounding box for each shoe image. For example, the image at classes/lowa_hiking/757550203 640.jpg, has the bounding box: (x1, y1, x2, y2) = (143, 55, 501, 417). We apply boundary box property to all shoe images and to generate a new annotated dataset.

We use SURF, LBP and SIFT descriptor to feature extractions from each image of Yahoo! Shoes Dataset. We select 9 images from each shoe classes to create a training image set, hence the test set includes 21 images from each shoe classes. The descriptors obtained from training images are clustered by k-means clustering method. Clustering centers are considered as visual words that are formed as visual feature vector. To generate image representation, each extracted descriptor is compared to the visual words and associated to the closest word. Finally, image feature histogram vector is obtained. We select randomly 9 images from each class in Yahoo dataset. These 9 images called user's images, we use them as part of test images in our system. The features are extracted from 9 test images with using SIFT, SURF and LBP descriptors. Each extracted features from test images is compared to final image feature histogram vector, then we recommend images which are similar with user's image. The similarity of user images with recommendation images is found with k-nn algorithm. The recommendation accuracy of the proposed recommendation algorithm with utilizing SIFT, Surf, LBP descriptors are respectively %69, %71 and %62. Also, the recommendation accuracy of the proposed system for each class in Yahoo! Shoe dataset is given in Table 1.

For example, we select 10 random images from 7 different heel shoe classes, and then we define these images as user-uploaded images. We recommend 10 shoe images to a particular user, after this recommendation methodology, the user can select a shoe image, which is interested or wanted by this user. An example of the proposed system process is given in Fig. 1, for this example 10 random images from 7 different heel classes are called/named query images, shown Fig. 1. (a). The proposed system recommends images to a particular user with in consideration of query images, hence the recommended images are shown in Fig. 1. (b). It can be concluded in Fig. 1 that only two recommended images are not in the heel shoe classes. Since, Fig. 1 demonstrates that the proposed system can still get good result when the users' images contain various shoes types or brands.

(a) Query Images

(b) Recommendation images

Figure 1. Images are selected from 7 different heel shoe classes as a users'-uploaded images (a) query images, (b) recommended images to a particular user.

Table 1. Recommendation accuracy (%) of the proposed recommender system for each shoe class in Yahoo! Shoe dataset

american eagle sandals	ariat western boots	badgley mischka high heels	betsey johnson platform high heels	birkenstock sandals	clarks sandals	cobian sandals
0,85	0,75	0,9	0,95	0,75	0,8	0,7
1	0,95	0,9	0,8	0,9	0,75	0,8
0,9	0,6	0,95	0,95	0,6	0,8	0,7
corso como flats	creative recreation sneakers	crocs clogs	crocs sandals	crocs slipons	cushe sandals	cushe slipons
0,6	0,6	0,35	0,8	0,2	0,85	0,55
0,75	0,7	0,3	0,9	0,35	0,65	0,65
0,8	0,7	0,4	0,8	0,3	0,7	0,2
ecco laced	ecco slipons	ed hardy sneakers	finn comfort sandals	fitflop sandals	frye laced	grazie sandals
0,3	0,4	0,8	0,9	0,75	0,25	1
0,35	0,4	0,95	0,95	0,9	0,8	0,9
0,05	0,5	0,5	0,75	0,9	0,4	0,9
havaianas sandals	irish setter boots	keen hiking	keen sandals	keen slipons	lacoste slipons	lacoste sneakers
0,75	0,85	0,7	0,7	0,35	0,6	0,35
0,9	0,85	0,45	0,65	0,5	0,65	0,75
0,95	0,6	0,3	0,65	0,25	0,4	0,5
le chameau rain boots	lowa hiking	manolo blahnik high heels	mephisto sandals	mephisto slipons	merrell sandals	merrell slipons
1	0,55	0,9	0,7	0,4	0,85	0,6
1	0,45	0,9	0,9	0,3	0,7	0,5
1	0,25	0,95	0,25	0,2	0,6	0,35
michael kors high heels	nike sandals	oakley sandals	pleaser usa high heels	pleaser usa platform high heels	polo sneakers	puma sneakers
0,8	0,65	0,8	1	0,8	0,5	0,8
0,8	0,8	0,8	1	0,9	0,6	0,7
0,7	0,8	0,95	0,95	0,6	0,4	0,4
quiksilver sandals	ralph lauren sandals	reebok sneakers	reef flip-flops	rider sandals	roxy sandals	sam edelman sandals
0,9	0,8	0,35	0	0,9	0,85	0,8
0,75	0,85	0,55	0,1	0,9	0,9	0,8
0,8	0,75	0,3	0	1	0,8	0,75
sanita clogs	sanuk sandals	sanuk slipons	sebago boat shoes	shiekh sandals	skechers sandals	skechers slipons
0,65	0,95	0,35	0,6	0,95	0,65	0,6
0,5	0,85	0,3	0,5	1	0,75	0,35
0,25	0,7	0,4	0,45	1	0,75	0,15
skechers sneakers	sorel boots	sperry boat shoes	sperry sandals	stuart weitzman high heels	superga sneakers	teva sandals
0,2	0,75	0,6	0,9	0,9	0,7	0,8
0,15	0,65	0,45	0,9	0,858	0,75	0,8
0,45	0,5	0,15	0,7	0,9	0,6	0,65
timberland boots	toms slipons	tory burch sandals	tretorn rain boots	volatile sandals	volcom sandals	yellow box sandals
0,65	0,65	0,8	0,8	0,85	0,75	0,85
0,5	0,8	0,75	0,85	0,8	0,75	0,75
0,4	0,75	0,7	1	0,9	0,85	0,75

4. CONCLUSION

The users are leaving information on the site when on the move, and recommender systems are used this information to recommend products as user's appreciation. Text-based and rating-based recommendation systems attempt to find and recommend items to the users, in contemporary studies. Recently, the number of shopping on the Web is expressed in millions, hence recommender systems are need effective methods to recommend item that user likes or has previously purchased. Hence, an image-based recommender system is examined to provide/propose an effective algorithm for recommender systems. In this paper, a new

recommendation algorithm has been proposed that returns the recommendation images utilizing from the users' uploaded images. After, the users upload images to the proposed system, image annotation techniques are used for extracting features from these images, and then the proposed system recommends images that have same features with the users' images. It is planned to use multi-label image annotation techniques to improve performance of this proposed image-based recommender system.

ACKNOWLEDGMENT

This paper was supported by the Technological and Scientific Research Council of Turkey under its TUBITAK 3001 program with project no: 116E284, entitled 'Developing Image-based Recommender System'. Again, this work was also supported by the Eskisehir Osmangazi University Scientific Research Project Commissions (Grant no.: 2018-1920).

REFERENCES

[1]. K. Pliakos, and C. Kotropoulos, "Building an image annotation and tourism recommender system", *Int. J. Artif. Intell. Tools*, vol. 24 (5), 2015.

[2]. A. Sasa, M. Krisper, Y. Kiyoki, and X. Chen, "A personalized recommender system model using colour-impression-based image retrieval and ranking method", in *Proc. ICIW*, pp.124-130, 2011.

[3]. J. Fan, D.A. Keim, Y. Gao, H. Luo, and Z. Li, "JustClick: Personalized image recommendation via exploratory search from large-scale flickr image collections", *IEEE Trans. Circuits Syst. Video Technol.*, vol. 19 (2), pp. 273-288, 2008.

[4]. P. Bhagat, N. Mahakalkar, R. Chaudhari, and A. Gotmare, "A survey paper on profile- based image recommender system for smartphone", *Int. J. of Eng. Res. Tech.(IJERT)*, vol. 3(10), pp. 69-72, 2014.

[5]. L. Cao, J. Luo, A. Gallagher, X. Jin, J. Han, and T.S. Huan, "A worldwide tourism recommendation system based on geotaggedweb photos", in *IEEE ICASSP*, pp. 2274-2277, 2010.

[6]. D. G. Lowe, "Distinctive image features from scale-invariant keypoints", *Int. J. Comput. Vision*, vol.60, pp. 91-110, 2004.

[7]. S. Van de, E.A. Koen, T. Gevers, and G. M.C. Snoek, "Evaluating color descriptors for object and scene recognition", *IEEE T. Pattern Anal.*, vol. 32 (9), pp. 1582-1596, 2010.

[8]. H. Bay, T. Tuytelaars, and L.V. Gool, "SURF: Speeded up robust features", in ECCV, Lecture Notes in Computer Science, Berlin, Germany: Springer, 2006, vol 3951.

[9]. J. Matas, O. Chum, M. Urban, and T. Pajdla, "Robust wide baseline stereo from maximally stable extremal regions", *Image Vis. Comput.*, vol. 22(10), pp. 761-767, 2004.

[10]. M. Heikkila, M. Pietikainen, and C. Schmid, "Description of interest regions with local binary patterns", *Pattern Recogn.* , vol. 42, pp. 425-436, 2009.

[11]. (2012) Yahoo! Shoes Dataset [Online]. Available: https://webscope.sandbox.yahoo.com/catalog.php?datatype=i.

Journal Homepage : http://dergipark.gov.tr/ejens
EJENS
European Journal of Engineering and Natural Sciences
CODEN: EJENS
DergiPark AKADEMİK

Development of Ecological Biodesign Products by Bacterial Biocalcification

Tugba Keskin[1*], Irem Deniz[2] , Alpcan Aric[1], Burak Talha Yilmazsoy[1], Ozge Andic-Cakir[3-4],Ayşegül Erdoğan[4], Didem Altun[5], Ayça Tokuç[5] , Burcu Filiz Demirci[5], Aylin Sendemir-Urkmez[1], Gülden Köktürk[6], Feyzal Özkaban[5]

[1]1Bioengineering Department, Engineering Faculty, Ege University, Izmir, Turkey
2Bioengineering Department, Engineering Faculty, Manisa Celal Bayar University, Turkey
3Civil Engineering Department, Engineering Faculty, Ege University, Izmir, Turkey
4Ege University Application and Research Center for Testing and Analysis, Izmir, Turkey
5Department of Architecture, Faculty of Architecture, Dokuz Eylul University, Izmir, Turkey
6Department of Electrical and Electronics Engineering, Faculty of Engineering, Dokuz Eylul University, Izmir, Turkey,.
**Corresponding Author email:keskin.tugba@gmail.com*

Abstract

Biodesign is an interdisciplinary field in which biological processes are combined with many different fields to produce environmentally friendly and economically feasible products. Within the scope of this study, first $CaCO_3$ production potential of *Sporosarcina pasteurii* has been observed and optimized, and then the capability of hardening of the sand is examined. The optimum $CaCl_2$ concentration for maximized $CaCO_3$ formation was found as 50 mM. The ecological urban element was designed and its mold was produced by 3D printer at lab scale. The *Sporosarcina pasteurii* was mixed with sand and filled into the mold. The sand was mixed with 50 mM $CaCl_2$ solution every day until hardening is observed. At the end of one week, a sitting element from hardened sand was produced. The $CaCO_3$ formation was observed with XPS analysis. Thus, an interdisciplinary approach was used to produce ecological biodesign products.

Key words

Biocalcification, Biodesign, Urban living elements, Sand hardening, *Sporosarcina pasteurii*

1. INTRODUCTION

With the progress of technology, great changes and developments especially in the social sense are emerging. The adverse effects of increasing technology and production capacities on nature and human health are also increasing at the same rate. The elimination of the negative environmental conditions or the reduction of the minimum environmental burden has been the focus of many researchers, along with developing bioengineering approaches. Increasing production capacities, which are the biggest reason of globalization, result in increasing harm to the human health of the emerging products [1].

On the other hand, the products related to the building sector causes the most damage to the environment in human activities. In this point of view, environmentally friendly, sustainable design products that are compatible with nature are now a developing field of study. A number of structures under the heading of sustainable architectural design are criticized by different approaches such as high material or resource consumption during the production process or afterwards, negative associations with the natural environment, and inability to integrate with the socio-cultural structure. Today, all kinds of urban furniture, architectural / structural / industrial materials / products (children playgrounds, seating elements, kiosks, exhibition stands, etc.) can be produced and used by processing natural materials (wood, stone, etc.) [2]–[4].

Biodesign is a study field, in which organisms are used as a design input, to create sustainable, functional, durable and non-health threatening products related to taking inspiration from natural processes [5]. It also

investigates natural building designs and structures for human welfare. Cooperative studies between engineers and designers are needed with respect to build progressive, bio-based, natural forms using microorganisms as a factory to produce a structure that is both functional and has aesthetics. One way to produce products can be by utilization of mineralization and biocalcification processes inherent in nature.

Formation of minerals in nature is known as a very slow process that can take as long as a geological time. Many of the mineral types are evoluted by microbial activity which is very dependent on microorganism strain. Ureases are the main enzymes used in mineralization processes. Ureases are homologous and Ni-dependent enzymes which can be found in many living organisms such as plants, bacteria etc. Ureases hydrolyze urea into ammonia and CO_2. *Sporosarcina pasteurii* is a wide spread soil bacterium. It has very large capacity of urease production [6].

One of the main activities of the role of microorganisms in nature is the microbial cementation, in other words biocalcification. Biocalcification can be performed by different strains of bacteria, *Sporosarcina pasteurii, Sporosarcina urea, Sporolactabacillus* etc[7].

Traditionally, gram-positive, aerobic or facultative anaerobic, sporulating, rod-shaped bacteria belong to the *Bacillus* family. This causes many heterogeneities in terms of the characteristics that must be defined within the *Bacillus* family. In 1889, the microorganism identified by Miquel Chester as *Bacillus pasteurii* was defined in 2001 by Yoon et al.[8], and its name was changed to *Sporosarcina pasteurii*. The cell size of *Sporosarcina pasteurii* varies between 1.3-4 ηm and the spores size is between 0.8-1.3 ηm. They live at a maximum temperature of 30-45 ° C and a minimum temperature of 5-15 ° C. They can be isolated from soil, water and mud layers and they are non-pathogenic microorganisms with a biosafety level of 1. *Sporosarcina pasteurii* is not conventional because its living conditions can withstand high pH conditions as well as environments containing ammonium salts at high concentrations. In most studies, urea has been used instead of the ammonium salt because these organisms have the ability to break down the urine [9].

The metabolic pathway of *Sporosarcina pasteurii* is as follows.

1 mol urea is converted to 2 mol ammonia and 1 mol CO_2.

$CO(NH_2)_2+H_2O \rightarrow NH_2COOH+NH_3$

$NH_2COOH+H_2O \rightarrow NH_3+CO_2+H_2O$

The pH of the soil medium is increased and the enzymatic reaction occurs by the addition of $CaCl_2$ and $CaCO_3$ precipitates. By the $CaCO_3$ metabolism, the negative effect of atmospheric release and global warming would be prevented [10].

$CO_2+H_2O \leftrightarrow H_2CO_3 \leftrightarrow HCO_3^-+H^+ \leftrightarrow CO_3^{+2}+2H^+$

$CO_3^{-2}+Ca^{+2} \rightarrow CaCO_3$

The microbial cementing ability demonstrated by this microorganism is widely used as an innovative and promising biotechnological application such as rehabilitation and reinforcement of cement materials [11]. In recent years, the selective cementation activity with the precipitation of $CaCO_3$ by microbiologically induced calcium carbonate biocalcification, was used for filling of cracks with calcite layers[12], blending of self healing mechanism with bacterial immobilization techniques [13], [14]. Another new application area is the use of *Sporosarcina pasteurii* to reduce the hydraulic conductivity in environmental processes. Magnus Larsson proposed this solution as a solution to desertification, including soil remediation, solid phase sequestration of contaminants, and carbon sequestration technologies[15].

In summary biocalcification is a process that is used in healing cracks in reinforced concrete buildings, soil stabilization and environmental processes. Recent studies were also showed that it can be used for hardening sand[16].

This study aimed to develop an architectural design product that is in harmony with the nature and suitable to human health with partnership of bioengineering and architecture disciplines via bacterial calcification to form an architectural structure with the support of 3D printing technology of poly-lactic acid (PLA). For this purpose, *Sporosarcina pasteurii* (*Bacillus pasteurii*) was chosen to use the urea mechanism to precipitate $CaCO_3$ thus hardening sand by utilizing urea. Even though there are limited studies that make use of bacterial calcification to harden sand, this is the first study to show a successful design element built with the help of a 3D printed mold.

2. MATERIALS AND METHODS

Sporosarcina pasteurii was obtained from the DSMZ culture collection and grown in Caso Agar DSM 33 medium. Growth medium content of bacterium; For 1L; 15 g peptone from meat, 5 g peptone form soymeal, 5 g NaCl, 20 g urea. For $CaCO_3$ production in broth medium 10, 30 and 50 mM $CaCl_2$ was added to the medium. For biocalcification DSM 33 medium with urea and 50 mM $CaCl_2$ was used.

2.1. Inoculum Preperation

Sporosarcina pasteurii was obtained from the DSMZ culture collection and grown in Caso Agar DSM 33 medium. Growth medium content of bacterium; For 1L; 15 g peptone from meat, 5 g peptone form soymeal, 5 g NaCl, 20 g urea. For $CaCO_3$ production in broth medium 10, 30 and 50 mM $CaCl_2$ was added to the medium. For biocalcification DSM 33 medium with urea and 50 mM $CaCl_2$ was used.

2.2. Bacterial Staining and Growth Curve

The Schaeffer-Fulton method was used for bacterial staining. The growth broth and the broth with $CaCl_2$ was prepared on microscope and air dried and heat fixed. The malachite green was added for endospore staining. Then the slide was rinsed with water to remove malachite green. Then the broth on slide was stained by safranin this secondary stain was again washed with water and air dried. The bacteria were observed under 1000X (oil immersion) with total magnification. The vegetative cells were observed by pink/red color.

Using the broth medium the growth performance of *Sporosarcina pasteurii* was measured at 600 and 660 nm of optical density during 24 h.

2.3. $CaCl_2$ Concentration Optimization in Broth Media

$CaCO_3$ concentration was reacted with an optimum concentration of $CaCl_2$. 10, 30 and 50 mM $CaCl_2$ was added to broth medium to start $CaCO_3$ formation. $CaCO_3$ was separated from broth medium by filter paper (Advantec 5, USA).

2.4. Bacterial Solidification

In bacterial solidification experiments, preliminary experiments were performed on petri dishes. First bacteria were grown on petri dishes agar medium. One petri without inoculums was used as control. The two petri dishes (with and without inoculums) were added with equal amounts of sea sand so that the height would be 2-3 cm. 10 mL of 50 mM $CaCl_2$-containing growth medium was added to the sand. Inoculum was added to one of the petri dishes. The petri dishes were left open in the incubator at 30°C. The feed medium was depleted for one week as the petri dishes appeared to solidify.

2.5. Design of urban, architectural and industrial elements

If the bacterial calcification process is directed, it is thought that it is possible to produce architectural, urban and industrial design products. Today, many industrial products contain harmful and toxic substances for health. Particularly the construction sector is one of the most harmful activities for environment within human activities. The designs, produced by this method, will be organic and ecological because they are shaped like processes in nature. It will not contain harmful and toxic substances found in the urban environment, architectural structures or in many other things we use in everyday life.

Basically, here is to direct the bacteria through engineering methods, without leaving it to natural growth process, for generating creative design products. By using this method, a vase or a plate, or a seating element or a playground for the city can be produced. These biodesign products will be a healthy and ecological alternative with a completely natural, non-toxic character. The goal is to make this even more advanced, so that it can be used on larger scale, in architectural structures or production of buildings. Very different from the construction methods of today, buildings can be produced from soil or from sand, by bacteria - in the direction of architects and engineers' designs. Although there are a variety of researchers study on this method, there is no detailed research on the directing of bacteria, nor is there an architectural structure produced by this method.

2.6. $CaCO_3$ Analysis

The presence of $CaCO_3$ was revealed by XPS analysis. The measurements were performed with a Thermo Scientific Model K-Alpha XPS instrument using monochromatic Al Kα radiation (1486.7 eV). Survey spectra and high-resolution spectra were acquired using analyzer pass energies of 50 eV. The X-ray spot size was 300 µm for single point analysis. Data were analyzed using Avantage XPS software package. Peak fitting was performed using Gaussian/Lorentzian peak shapes and a Shirley/Smart type background.

3. RESULTS AND DISCUSSION

3.1. Bacterial Staining Results and Growth Curve of Bacteria

Determination of life cycle of microorganisms is very important for optimal process performance. The growth curve of *Sporosarcina pasteurii* was sketched by measuring the optical density of 600 and 660 nm by taking samples every 2 h during 24 h and the graph was sketched time vs OD (Optical Density). The results showed that the most active times of *Sporosarcina pasteurii* is between 6-8 h (Figure 1). According to this result the inoculation of all processes was done at 6 h.

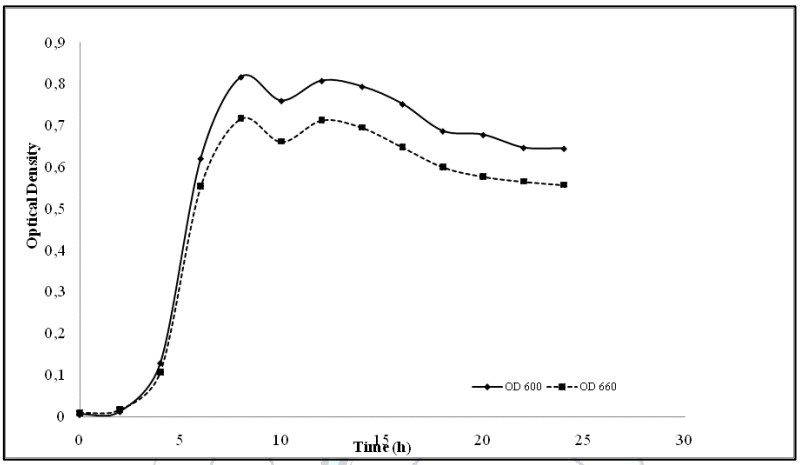

Figure 1. Growth curve of Sporosarcina pasteurii

The bacterial staining was performed according to Schaffer Fulton method. In this method red-purple colors showed the vegetative *Sporosarcina pasteurii*, which means these are active microorganisms (Figure 2 a). In this method the stains were not washed with alcohol or any other chemicals so we can observe the cluggings of $CaCO_3$ formation in the broth medium containing 50 mM $CaCl_2$ (Figure 2 b). The $CaCO_3$ formation was not enough with the broth medium containing 10 mM $CaCl_2$(Figure 2c) and 30 mM $CaCl_2$ (Figure 2 d) .

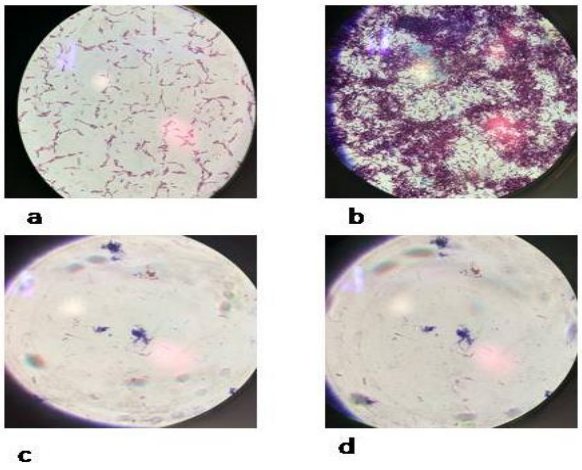

Figure 2. Staining microphotographs of the bacteria(X100; 1024dpi, olympus E 400)

3.2.$CaCl_2$ Concentration Optimization in Broth Media

$CaCO_3$ precipitates were produced by hydrolysis of urea which results in production of ammonia and carbonate. Carbonate binds calcium ions in medium and after this reaction $CaCO_3$ crystals can be formed. $CaCO_3$ (calcium carbonate) concentration is related with an optimum concentration of $CaCl_2$;10 mM, 30 mM and 50 mM $CaCl_2$ was added to broth medium to start $CaCO_3$ formation. Starting from the second hour (Figure 3a) of the process a white powder started to appear which is a mixture of $CaCl_2$ and $CaCO_3$ crystals. The concentration of the $CaCO_3$ increased by incubation at 30 ^oC during 7 days and the photos taken on day 1, day 2 and day 7, respectively. (Figure 3b, c and d)). $CaCO_3$ was separated from broth medium by filter paper and weighted. The weight of the $CaCO_3$ produced from 10 mM, 30 mM and 50 mM are 1.02 g, 1.34 g and 1.62 g respectively. In another study conducted by Dhami et al.[17]. The amount of precipitated $CaCO_3$ from different strains of B. megabacterium MTCC 1684 was between 0.84-0.076. This difference caused from the difference of bacteria and also the medium used.

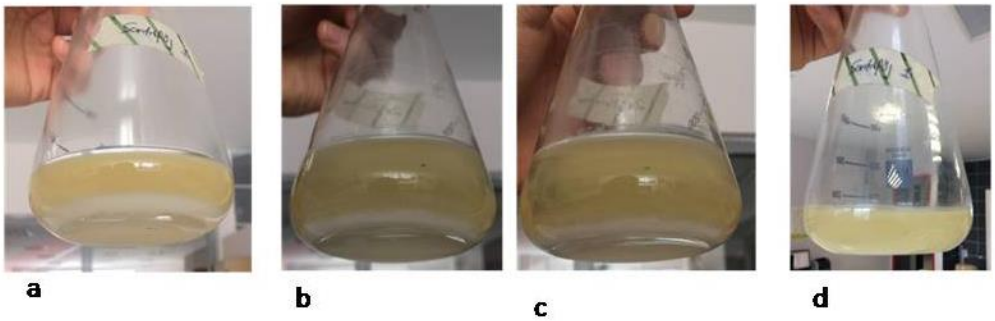

Figure 3. $CaCO_3$ formation during incubation (after; a)1 hour; b) 2 hours; c) 1 day; d) 1 week)

3.3. Bacterial Solidification

Microbially induced $CaCO_3$ is a very important product which can be used to fix cement cracks and fissures in structural formation. The most important application area for microbiologically induced $CaCO_3$ is remediation of damaged concrete. Microbiologically induced $CaCO_3$ formation reaction generally ends with high pH because of series biochemical reactions. *Sporosarcina pasteurii* is plays an important role in this process by producing urease to hydrolyze urea to ammonia and O_2. The produced ammonia will increase the pH of surroundings and calcite precipitation will start[18].

In this study, first of all, attempts were made to be sure about the solidification process is carried out by *Sporosarcina pasteurii* in petri dishes. *Sporosarcina pasteurii* is grown on agar plates and the 2-3 cm height sand as put on it. Then the medium with $CaCl_2$ was spread over sand daily until solidification completed. Another petri without inoculums was used as control. The same procedure was applied on it. It was seen that the inoculum-free sand has elasticity (Figure 4a) just because of the agar and can be easily and rapidly disintegrated while the inoculum-containing sand is hardened (Fig. 4b).

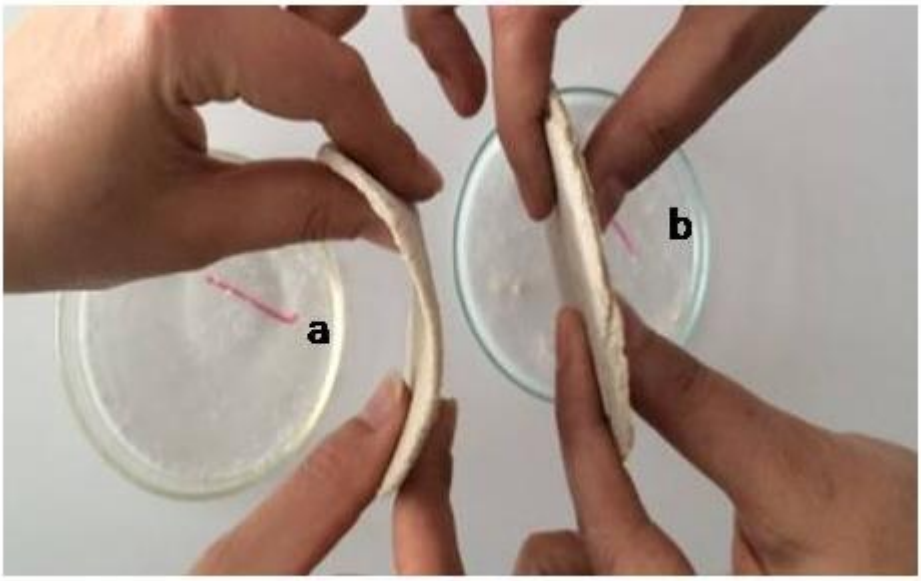

Figure 4. Solidification trials on petri dishes (a. without inoculum; b. with inoculum)

3.4. Production of Environmentally Friendly Design Elements by Bacterial Solidification

After the successful solidification process in petri dishes, a unique design element was designed and taken out from the 3-D printer (Figure 5). The design element that was selected for production with biodesign in this paper is a multipurpose urban furniture. It is part of a product range for parks and can be used to sit or lie on under various weather conditions including next to the sea. The product in this paper was scaled down for laboratory conditions.

Figure 5. 3D printed design

First of all this structure was filled with sand. Inoculum was then added to the sand and evenly distributed throughout. The DSM 33 growth medium containing 50 mM $CaCl_2$ was evenly distributed on the sand too and incubated for 1 week in a 30°C incubator. The design unit obtained at the end of one week is shown in Fig 6.

The ability of CO2 capture by Sporosarcina pasteurii is was analyzed by Okwadha and Li [19] and they found that CO2 usage by ureolytic activity can be used for microbial $CaCO_3$ formation. Another application area where

Figure 6. Environmentally friendly solidified design element

Sporosarcina pasteurii is used is civil engineering. A study conducted by Achal et al.[20] resulted in the increase of durability of concrete and Jonkers et al.[16]showed the self healing capability of concrete by *Sporosarcina pasteurii*.

Stocks and Fisher [7] used narrow plastic columns to detect the solidification ratio and ability of sand hardening by *Sporosarcina pasteurii* was analyzed by SEM and XRD. The analysis showed the formation of calcite crystals which decreased the permeability of solid by 98%.

The sand hardening properties of the bacteria in the work done by Sarmast et al.[21] have been tested in plastic columns. It has been observed to harden for 7 days in a similar quadrant in our study. At the end of this process, the stiffened sections were taken and $CaCO_3$ crystals formation was compared and equal distribution throughout the column was observed. In our study, the possibility of taking the advantage of the sand hardening properties of bacteria to create a sophisticated architectural design elements which can be readily used in daily life.

3.5. Solidification and $CaCO_3$ Analysis Results

Ca 2p peaks have clearly spaced spin-orbit components ($\Delta_{carbonate}$ =3.5 eV). In the present study, Ca 2p region for this material (Figure 7) exhibits a well-resolved doublet with a Ca $2p_{3/2}$ component at 347.1 eV and a Ca $2p_{1/2}$ component at 350.7 eV. The Ca $2p_{1/2}$ and Ca $2p_{3/2}$ bands are separated by 3.6 eV indicating that the structure is $CaCO_3$.

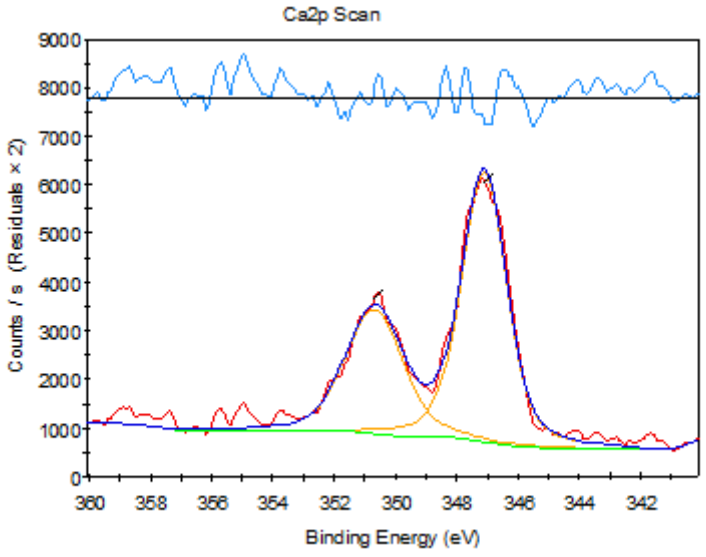

Figure 7. XPS spectrum of Ca in solidified sand

Sarmast et al. [21] used 2 bacterial species (*Sporosarcina pasteurii* is and *Sporosarcina urea*) to test the reaction times of solidifying at sandy soil columns. The results showed that $CaCO_3$ precipitation so does solidification is more favorable with *Sporosarcina pasteurii* and 12% $CaCO_3$ precipitation was observed. In our study according to XPS results 10% $CaCO_3$ precipitation was observed with 50 mM $CaCl_2$ addition.

CONCLUSION

Sporosarcina pasteurii is an environmentally friendly bacterium that can be used in hardening sand. Bacterial solidification was achieved after addition of $CaCl_2$ to the medium. In future studies, real scale designs will be manufactured via harmless environmental processes and elements made by living organisms can be produced at larger scales. The originality of this study is that the resulting products are healthier and ecological alternatives to urban constructions with detrimental health and environmental effects. Besides the novel composition and production of the design products, they aim to be totally natural, non-toxic and durable. From a social point of view, this totally natural alternative production method in the environmentally notorious construction industry gives hope to the future generations for a new way of living.

ACKNOWLEDGMENT

The authors wish to thank Prof. Dr. Nuri Azbar for the technical support by Environmental Biotechnology and Bioenergy Laboratory and Can Aysan for 3D printing support.

REFERENCES

[1] L. S. Wong, "Microbial cementation of ureolytic bacteria from the genus Bacillus: a review of the bacterial application on cement-based materials for cleaner production," *J. Clean. Prod.*, vol. 93, pp. 5–17, 2015.

[2] I. Fjørtoft and J. Sageie, "The natural environment as a playground for children," *Landsc. Urban Plan.*, vol. 48, pp. 83–97, 2000.

[3] I. Fjørtoft and J. Sageie, "The natural environment as a playground for children. Landscape description and analyses of a natural playscape," *Landsc. Urban Plan.*, vol. 48, no. 1–2, pp. 83–97, 2000.

[4] E. M. Campa, "Pensamientos compartidos. Aldo van eyck, el grupo cobra y el arte," *Rev. Proy. Progreso, Arquit.*, no. 11, pp. 64–75, 2014.

[5] M. Taya, "Bio-inspired design of intelligent materials," *Smart Struct. Mater.*, vol. 5051, pp. 54–65, 2003.

[6] D. Olivera-Severo, G. E. Wassermann, and C. R. Carlini, "*Bacillus pasteurii* urease shares with plant ureases the ability to induce aggregation of blood platelets," *Arch. Biochem. Biophys.*, vol. 452, no. 2, pp. 149–155, 2006.

[7] S. Stocks-Fischer, J. K. Galinat, and S. S. Bang, "Microbiological precipitation of $CaCO_3$," *Soil Biol. Biochem.*, vol. 31, no. 11, pp. 1563–1571, 1999.

[8] J. H. Yoon, K. C. Lee, N. Weiss, Y. H. Kho, K. H. Kang, and Y. H. Park, "*Sporosarcina aquimarina* sp. nov., a bacterium isolated from seawater in Korea, and transfer of *Bacillus globisporus* (larkin and stokes 1967), *Bacillus psychrophilus* (Nakamura 1984) and *Bacillus pasteurii* (Chester 1898) to the genus *Sporosarcina* as *Sporosa*," *Int. J. Syst. Evol. Microbiol.*, vol. 51, no. 3, pp. 1079–1086, 2001.

[9] W. R. Wıley and J. L. Stokes, "Requirement of an alkaline pH and ammonia for substrate oxidation by *Bacillus pasteurii*.," *J. Bacteriol.*, vol. 84, pp. 730–734, 1962.

[10] R. Siddique and N. K. Chahal, "Effect of ureolytic bacteria on concrete properties," *Construction and Building Materials*, vol. 25, no. 10. pp. 3791–3801, 2011.

[11] S. J. Park, Y. M. Park, W. Y. Chun, W. J. Kim, and S. Y. Ghim, "Calcite-forming bacteria for compressive strength improvement in mortar," *J. Microbiol. Biotechnol.*, vol. 20, no. 4, pp. 782–788, 2010.

[12] Q. Chunxiang, W. Jianyun, W. Ruixing, and C. Liang, "Corrosion protection of cement-based building materials by surface deposition of $CaCO_3$ by *Bacillus pasteurii*," *Mater. Sci. Eng. C*, vol. 29, no. 4, pp. 1273–1280, 2009.

[13] J. Wang, K. Van Tittelboom, N. De Belie, and W. Verstraete, "Use of silica gel or polyurethane immobilized bacteria for self-healing concrete," *Constr. Build. Mater.*, vol. 26, no. 1, pp. 532–540, 2012.

[14] H. M. Jonkers and E. Schlangen, "Crack Repair By Concrete-Immobilized Bacteria," *Civ. Eng.*, no. April, pp. 1–7, 2007.

[15] B. Mahanty, S. Kim, and C. G. Kim, "Biokinetic modeling of ureolysis in Sporosarcina pasteurii and its integration into a numerical chemodynamic biocalcification model," *Chem. Geol.*, vol. 383, pp. 13–25,

2014.
[16] H. M. Jonkers and M. C. M. van Loosdrecht, "BioGeoCivil Engineering," *Ecological Engineering*, vol. 36, no. 2, pp. 97–98, 2010.
[17] N. K. Dhami, M. S. Reddy, and A. Mukherjee, "*Bacillus megaterium* mediated mineralization of calcium carbonate as biogenic surface treatment of green building materials," *World J. Microbiol. Biotechnol.*, vol. 29, no. 12, pp. 2397–2406, 2013.
[18] S. S. Bang, J. K. Galinat, and V. Ramakrishnan, "Calcite precipitation induced by polyurethane-immobilized *Bacillus pasteurii*," *Enzyme Microb. Technol.*, vol. 28, no. 4–5, pp. 404–409, 2001.
[19] G. D. O. Okwadha and J. Li, "Optimum conditions for microbial carbonate precipitation," *Chemosphere*, vol. 81, no. 9, pp. 1143–1148, 2010.
[20] V. Achal, A. Mukherjee, and M. S. Reddy, "Microbial concrete: Way to enhance the durability of building structures," *J. Mater. Civ. Eng.*, vol. 23, no. 6, pp. 730–734, 2011.
[21] M. Sarmast, M. H. Farpoor, M. Sarcheshmehpoor, and M. K. Eghbal, "Micromorphological and biocalcification effects of *Sporosarcina pasteurii* and *Sporosarcina urea*e in sandy soil columns," *J. Agric. Sci. Technol.*, vol. 16, no. 3, pp. 681–693, 2014.

Journal Homepage : http://dergipark.gov.tr/ejens
EJENS
European Journal of Engineering and Natural Sciences
CODEN: EJENS
DergiPark AKADEMİK

Developments and Applications in Enzyme Activated Membrane Reactors: A Review

Nadir Dizge [1*], Ruken Esra Demirdogen [2], Kasim Ocakoglu [3]
[1]*Mersin University, Department of Environmental Engineering, 33343, Mersin, Turkey.*
[2] *Cankiri Karatekin University, Department of Chemistry, 18100, Cankiri, Turkey.*
[3] *Tarsus University, Department of Energy Systems Engineering, 33400 Tarsus, Turkey*
**Corresponding Author email: ndizge@mersin.edu.tr*

Abstract

Enzyme immobilization has been significant in applying polymer membranes to prevent biofouling or to create catalytic reactions. So far, several modification methods have been employed for modifying surface of membranes. Among these methods, enzyme immobilization on polymeric membranes have gained much attention. Enzymes can be immobilized either via physical or chemical methods. This review summarizes the recent literature on modification of polymer membranes using various immobilization techniques.

Key words

Polymeric membranes, enzyme activated membranes, enzyme immobilization, membrane reactor, catalytic membrane separation process

1. INTRODUCTION

Membrane technologies have been widely used for reducing water consumption, reusing and recycling treated water, and producing freshwater via desalination. Membrane treatment offers better water quality when compared with other treatment methods. However, membranes can be used as reactors for achieving simultaneously catalytic reactions and separation process. Membrane reactors, which benefit from collaboration of different disciplines such as chemical reaction engineering, separation technology, materials science, also mathematical modelling aspects. They couple chemical reactions with membrane separation and provide a cost effective and more system design besides improved performance with regard to selectivity and/or yield [1]. Extensive research is still going on to modify membrane surfaces and enzyme immobilization on polymeric membranes to obtain biocatalytic membrane reactors.

In this review, recent developments, applications and future perspectives in enzyme activated membrane reactors are discussed.

2. CATALYTIC MEMBRANE REACTORS

Membranes are semi-permeable thin layer of materials capable of separating contaminants as a function of their physical or chemical properties and therefore they have been preference of choice in clean and valuable separation processes as well as for removal of suspended particles and microorganisms [2]. There are different types of membranes which can be classified according to their pore sizes and charge affinity. Therefore, they are utilized in a wide range of applications such as microfiltration (MF), ultrafiltration (NF), nanofiltration (NF) and reverse osmosis (RO) [3].

When rejected macromolecules or other substance solutes are adsorbed in the pores of the membranes plugging occurs which causes membrane fouling [4]. The factors, which are responsible for membrane fouling can be grouped under three main categories [5,6]: (i) feed suspension properties such as particle size, particle concentration, pH and ionic strength), (ii) membrane properties such as hydrophobicity, charge and pore size), and (iii) hydrodynamics such as cross-flow velocity, transmembrane pressure.

There is an increasing interest in producing biocatalytical membrane surfaces by immobilizing enzymes on membranes for to obtain catalytical membranes as well as for to minimize membrane fouling so that these membrane systems can be employed as reactor. There are many reactor types currently in use today. Among many reactors immobilized enzyme membrane reactor (ImEMR) is usually preferred as a suitable platform for continuous reactor operation that does not require an additional step to recover the enzyme [7,8].

3. ENZYME DEFINITION

Catalysts are used for increasing reaction rates without being a part of the reaction products [9]. Enzymes, which are the biological catalysts, have high specificity and catalyze or in other words increase the rate of one or few closely related chemical reactions without altering the equilibrium state. Enzymes acting as catalyst lower the activation energy and thus increase the rate of the reactions in the cells, which would not have occurred even over time periods of years, and enable these reactions occur in fractions of seconds and finally attain the equilibrium state (Figure 1). If enzymes had been absent most cellular reactions would not have even occurred and if cellular reactions had not been fast it would be impossible to see life in its present form. As any other catalyst enzymes themselves also undergo transient changes during the reactions. However, in the overall process, enzymes do not undergo any net change [10]. Enzymes as catalysts take place in some vital processes such as:

1) regulating the structure and function of cells and organisms,
2) synthesizing and breaking down biochemical building blocks and macromolecules,
3) transmitting genetic information,
4) transporting compounds across membranes,
5) providing motility of organisms,
6) converting chemical energy,
7) enable biochemical reactions proceed at the necessary rate in physiological conditions.

One of the most basic and characteristic feature of enzymes is their specificity. To state it in other words, each reaction in the cell is catalyzed by its own, specific enzyme. Specificity of enzymes depends both on the structure of the enzyme and the active sites where the substrate molecule -the substances upon which enzymes act- binds on the enzyme. Substrate do not necessarily have to be small molecules they can also be macromolecules like the enzyme itself like trypsin which is the enzyme that uses polypeptides as substrates and acts on them by hydrolysing the peptide bonds [10]. Enzymes function over the mechanism that proceeds through binding to the substrate at the beginning via non-covalent interactions such as hydrogen bonds, ionic bonds and hydrophobic interactions.

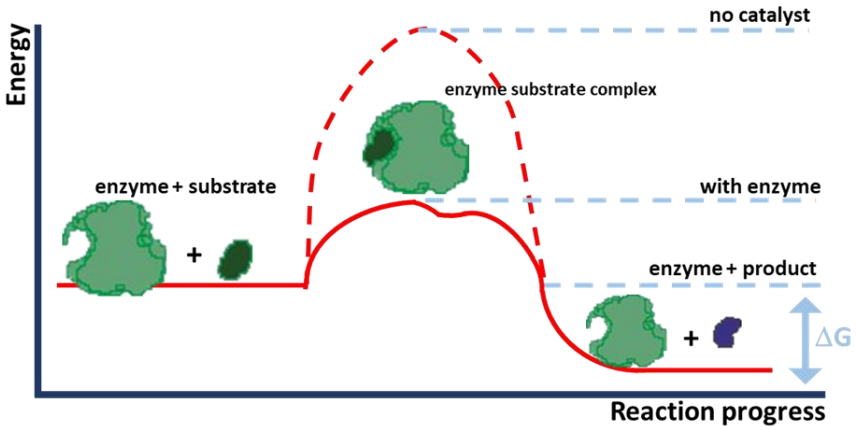

Figure 1. *Activation energy versus reaction progress for a catalyst*

Enzyme Immobilization Techniques

Enzyme engineering, which heavily relies on enzyme applications and thus mostly benefits from enzyme immobilization as a powerful tool, plays a vital role in the biotechnological processes [11,12]. Incorporation of enzymes in artificial membranes perform bio-chemical transformation of substrates during filtration of feed solution and doing this in a continuous mode with improved stability and activity has gained much importance [13,14]. These bio hybrid systems, which can be considered micro or nano chemical reactors, have become a breakthrough in membrane technology [15].

The success of enzyme applications is related to the success of enzyme immobilization which depends on the following criteria: (i) resistance of enzyme to leaking, (ii) high enzyme activity which can be retained over a long-term use and storage; (iii) no unfavorable alterations in kinetic properties; (iv) immobilization matrix should be negligible diffusional limitation and fouling; (v) sustained operational stability under adverse environmental conditions; (vi) fast catalytic activity exhibited by enzymes; (vii) proper enzyme immobilization density with adequate orientation; (viii) reasonable operational costs and additional costs (i.e. career and fixing agents and immobilization process), (ix) easy access to immobilized matrixes (or support materials) [11]. The last criteria indicate that proper selection of the support materials (i.e. solid beads, porous particles or membranes) plays a key role in enzyme immobilization. This selection can be made either according to the chemical (i.e. hydrophilicity, hydrophobicity, ionic charges) or geometric properties (i.e. shape, size, porosity, pore size distribution) of the support material [11,16,17].

The structural or the geometric properties of the support material such as the particle shape and size have profound effect on the intrinsic activity of the enzyme-loaded particles [11,18]. For instance, the carriers with spherical shape have large surface area and high enzyme loading capability. Particles with pore sizes in the 10 to 100 µm range – micro particles – have been preferred in food, pharmaceutical, biofuel cell production, and bioremediation [9,11]. However, particles with pore sizes <0.1 µm – nanoparticles – have mostly been preferred in medical applications such as biological/chemical sensing, drug delivery and disease diagnostics [19].

Depending on their chemical properties carriers can be categorized as inorganic and polymeric materials. Due to the favorable mechanical properties and facile tailorability of the latter category polymeric materials have become preference of choice in most of the applications [20]. Moreover, chemical properties of the support material determine the route of immobilization. That is to say whether immobilization will go through the route of binding to the support (physical adsorption, ionic bonding and covalent bonding) or will be via entrapment as well as encapsulation within the support, or cross-linked on the support. A schematic illustration of enzyme immobilization methods is presented in Figure 2.

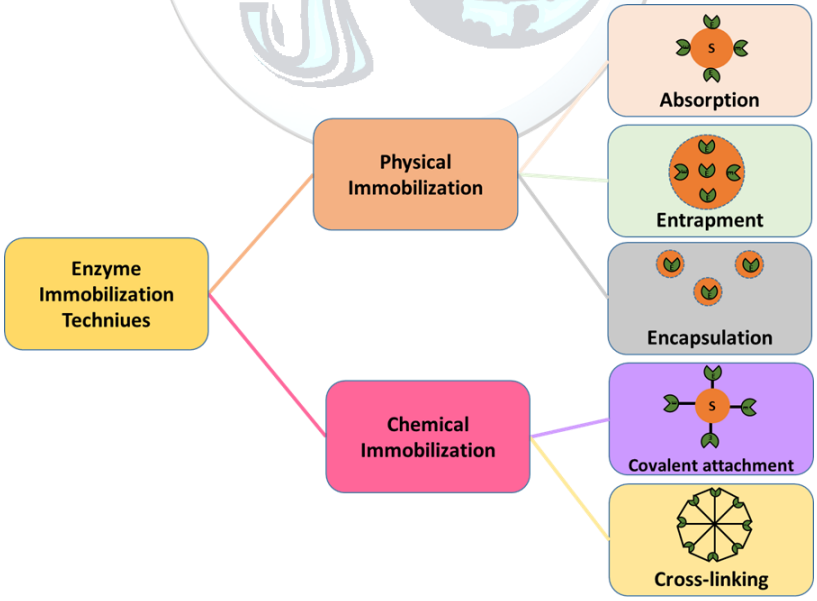

Figure 2. *Schematic explanation for enzyme immobilization techniques*

A key factor in enzyme immobilization is choosing the appropriate support since to a great extent the nature of the support and its bonding with the enzyme is the determining step regarding the efficiency of the enzyme. Therefore, it is necessary that the support has high affinity or capacity for enzymes. Moreover, the chemical structure of the support should enable the interaction between the enzyme and the substrate be maximum. Besides favorable

chemical properties, an appropriate support should have thermal resistance, chemical durability and be resistant against contamination and fouling and at the same time be cost effective [21]. Additionally, a preferred immobilization technology should have the following features: (i) enzyme reuse; (ii) favorable working pH and temperature; (iii) product separation should be easy; (iv) possibility of co-immobilizing different enzymes reactor design should be simple; (v) wider choice of reactors [22-24].

When working with enzyme immobilized membranes it is a key factor to avoid deactivation of the enzyme. Since the substrate is retained in the reactor for a much shorter time than the immobilized enzyme, immobilized enzyme membrane reactors is much more efficient than batch operations on the condition that the immobilized enzymes are replaced with fresh enzymes for the purpose of cleaning the membrane when the membrane gets oversaturated with the substrate [25,26]. Therefore, reactors play a key role in the success of the operation of the immobilization technology.

4. DIFFERENT TECHNIQUES FOR ENZYME IMMOBILIZATION ON POLYMERIC MEMBRANES FOR BIOCATALYTIC REACTORS

4.1. Physical Immobilization on Polymeric Membranes

4.1.1. Adsorption

Adsorption is the method of preference for enzyme immobilization due to its simplicity. One of its main disadvantages is its limited turn over number since the enzyme leaks from the matrix. In a research conducted by Giorno et al. [27] a multiphase enzyme-loaded membrane system was used for investigating mass transfer performance of naproxen acid and ester [27]. This system was preferred for preparing two-separate phase enzyme membrane reactor (TSP-EMR). The experimental set-up is presented in Figure 3. The TSP-EMR was used for converting racemic ester of naproxen into the corresponding S-naproxen acid in an enantioselective manner. Since the transport kinetics of the system were investigated when there was no biochemical reaction, the overall mass transfer coefficients of naproxen ester, which is the reactant, and S-naproxen acid, which is the product, through the TSP-EMR was measured via loading a deactivated enzyme on the membrane. This loading was carried out under two different conditions, which are either the enzyme was immobilized alone on the membrane or the enzyme was immobilized in the presence of oil/water (o/w) emulsion, which constitutes the multiphase system, where the organic and the aqueous phase are separated by a polymeric membrane. The transport rate of naproxen acid, which is polar in nature, and naproxen ester, which is apolar in nature, through the polymer membrane (50 kDa molecular cut-off), hydrophilic in nature, and through the enzyme immobilized membrane systems in the presence and absence of o/w emulsion were evaluated. The membrane was placed in upright position and no pressure was applied from neither side of the membrane (TMP = 0) (Figure 3).

The transport rate of naproxen acid from shell-to-lumen was measured at 30 °C with initial acid concentration of 2.53 mM in the reservoir of shell side. The shell and lumen sides were found to have Reynolds (Re) numbers of 17.0 and 122.1, respectively. The results revealed that the change in concentration of naproxen acid in the shell and lumen sides would be asymptotic. The relationship between the change in the concentration of Naproxen acid in the lumen side and the contact time between the solutions on the shell and the lumen sides was in direct and linear proportion. It was found that after 22 h continuous operation the concentration of naproxen acid in the lumen side was around 0.34 mM and under these experimental conditions the transfer rate of naproxen acid was about 4.21×10−6 mMs−1.

The transport of naproxen ester through the membrane from the shell to the lumen side at 30 °C was investigated with (R,S)-naproxen ester with an initial concentration 2.50 mM in the reservoir of shell side was investigated. The Reynolds numbers in the shell and lumen sides were found to be 30.6 and 157.0, respectively. The change in the concentrations of naproxen acid and naproxen ester in the membrane were similar to each other. Under the said experimental conditions, the transfer rate of naproxen ester was about 7.8×10−8 mMs^{-1}. The transfer rate of naproxen acid was two orders of magnitude more than the transfer rate of naproxen ester.

The transport kinetics (i.e. transport rate and the overall mass transfer coefficient of naproxen acid and naproxen ester) as a function of fluid dynamic parameters (i.e. axial velocity) were investigated. It was observed that K_{ov} and the axial velocity was directly proportional with each other, but K_{ov} for naproxen acid ($\sim 10^{-7}$) was higher than that for naproxen ester ($\sim 10^{-9}$). It was also observed that presence of emulsion during immobilization of the enzyme improved the mass transfer of naproxen ester through the membrane. It was reported that knowing the mass transfer properties of both naproxen acid and the ester that is of the reactant and the product enabled the reactor to be used at the highest performance for the enantioselective hydrolysis of racemic mixtures of naproxen methyl ester into S-naproxen acid.

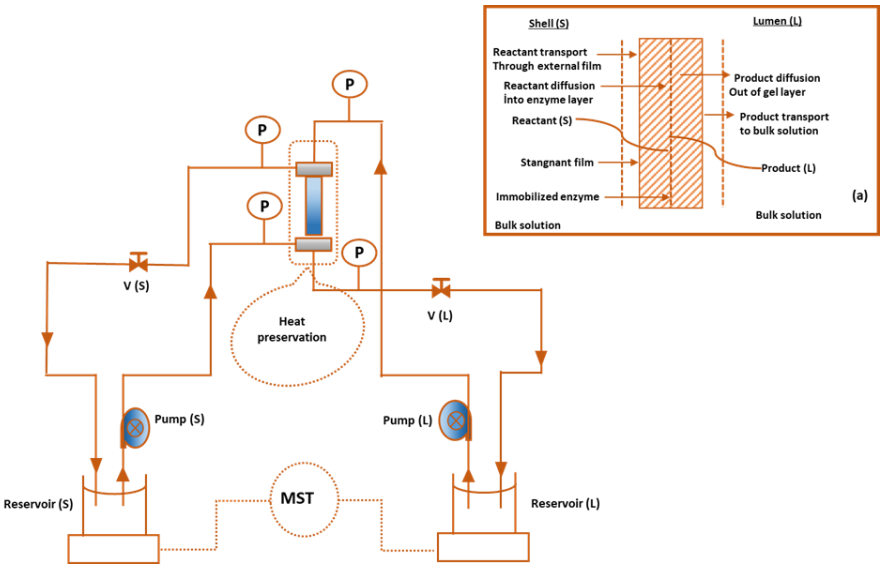

Figure 3. *Schematic diagram of the TSP-EMR (V: stands for valve; S: for shell side; L: for lumen side; MST: for magnetic stirrer with temperature controller and P: manometer. The arrows show the direction of the flow in the system) [27].*

Xu et al. have reported a method for fast protein digestion via stable microporous reactor prepared by a simple and cost-effective method based on sequential adsorption of poly(styrene sulfonate) and trypsin in nylon membranes [28]. Proteolysis was facilitated by the high local trypsin concentration and short radial diffusion distances in membrane pores that occurred in a few seconds. Since the pressure drop across these thin membranes was small these membranes were appropriate for use in syringe filters. After bovine serum albumin was digested via the membranes and 84% sequence coverage was attained. This was higher than the coverage obtained with a 16 h in-solution digestion, which was 71%, and that was obtained by other methods utilizing immobilized trypsin, which was less than 50%. Protein digestion in membranes modified with trypsin occurs when 0.05 wt% sodium dodecyl sulfate (SDS) is present. However, at the end of in-solution digestion under similar conditions no peptide signal is observed in the MS spectra. It was observed that presence of SDS had no effect in this. This study reports that the shelf life of these membrane reactors is not less than several months and these membranes can digest protein continuously for more than 33 h while maintaining their activity considerably.

As presented in Figure 4, the solution, which pass through the commercially available polymer membranes, separates into many streams. The micrometer-size pores of these membranes cause the radial diffusion distances between the solution and the wall of these membranes to be short (~1 μm). Therefore, these membranes are considered to be similar to monoliths.

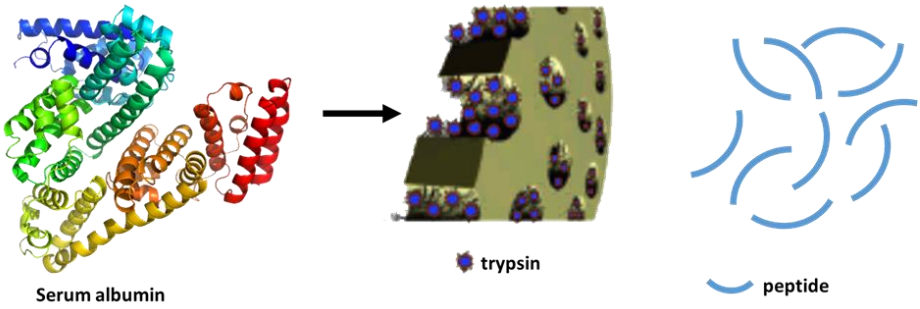

Figure 4. *Schematic presentation of a membrane reactor for tryptic digestion [28].*

As can be seen in Figure 5, a 4 mm disk was cut from a 25 mm-diameter membrane modified with trypsin and inserted in an Upchurch low-pressure in-line filter system where a frit was placed between the membrane and the downstream tubing for samples of a few microliters.

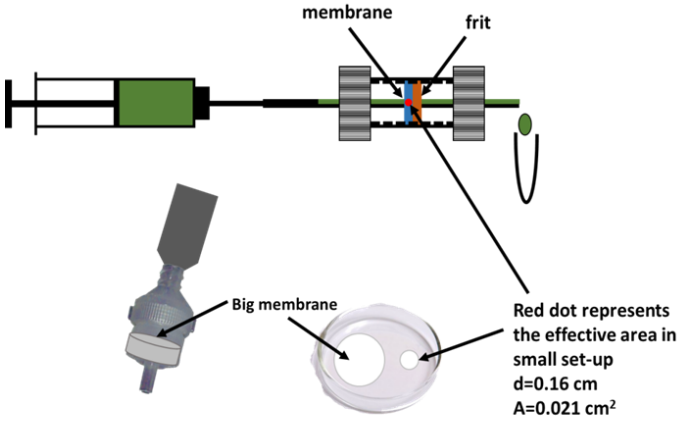

Figure 5. *Schematic presentation of the miniaturized membrane holder (top), the Swinnex Holder (bottom left), and a photograph (bottom right) of the 25 mm membrane disk and a miniaturized membrane [28]*

Trypsin concentration in the membrane pores was found to be high when PSS and trypsin were sequentially adsorbed in nylon supports. This provided proteolysis to ocur in short residence times of a few second. MALDI-MS results revealed that the protein sequence coverage achieved in digestion of R-casein by membranes was similar or higher than that obtained in in-solution digestion. It was observed that the MS detectable peptides obtained in BSA digestion, in-solution digestion and other digestion techniques such as those using trypsin immobilized monoliths was at least 1.4 times less than that obtained via digestion in membranes. Miniaturized membranes provide several advantages such as low sample consumption (i.e. a few microliters) and short processing times (1,7 μL solution/min). Moreover, if the conditions are optimized this time may decrease significantly. On the other side, when immobilized trypsin is used digestion may even take place in solutions containing 0.05% SDS. However, no MALDI-MS signal was observed for solution digestion under similar conditions even when SDS was removed from the solution by cation-exchange before the analysis. It is expected that trypsin-modified membranes would facilitate protein analysis due to the advantages they offer such as long-term stability and simple fabrication and those mentioned above [28].

4.1.2. Entrapment

Amounas et al. [15] used entrapment method to immobilize glucose oxidase (GOD) and peroxidase (POD) enzymes in a polypyrrole matrix by an avidin–biotin molecular recognition process. The mechanism is given as follow:

$$\text{Glucose} + O_2 \longrightarrow \text{GOD} + H_2O_2 + \text{gluconolactone}$$

$$H2O2 + POD_{ox} \longrightarrow POD_{red} + H_2O$$

$$POD_{red} + \text{pyrogallol} \longrightarrow \text{purpurogallin} + POD_{ox}$$

The enzymes were immobilized in electro-polymerized polymer using a biotin labeled pyrrole precursor. The amount of enzyme entrapped in the polymeric matrix was 60% and 83% for GOD and POD, respectively. The fabricated enzyme activated membranes showed a good performance during the permeation of the substrates which were glucose and hydrogen peroxide for GOD and POD enzymes, respectively. The reactive membranes catalyzed the oxidation of glucose in the presence of oxygen by GOD activated membrane whereas the reduction of hydrogen peroxide in the presence of the oxidant pyrrogallo by POD activated membrane. The enzyme activated POD membrane exhibited excellent stability with less than 6% decrease of activity when stored for 80-day. They concluded that enzymatic membranes can be used for the treatment of aqueous media due to high enzyme immobilization and stability [15].

Giorno et al. [27] immobilized in a polyamide capillary polymeric membrane by entrapment method using the lipase from *Candida rugosa* to develop a multiphase enzyme membrane reactor. The reactor was designed to have a configuration of a two separate phase emulsion enzyme membrane reactor (TSP-E-EMR) and two separate phase enzyme membrane reactor (TSP-EMR) (Figure 6).

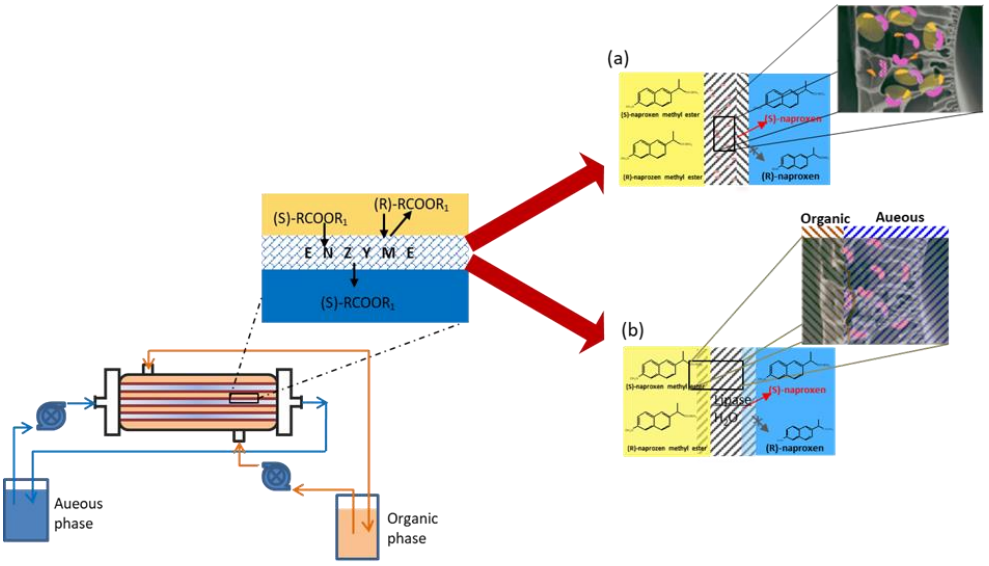

Figure 6. *Schematic representation of the membrane reactors used: (a) the two separate phase emulsion enzyme membrane reactor (TSP-E-EMR) and (b) the two separate phase enzyme membrane reactor (TSP-EMR) [27].*

A stable and uniform oil-in-water emulsion was prepared by membrane emulsification. The enzyme was used in free form and it was performed using triglycerides as substrate in a stirred tank reactor. The results indicated that the specific activity of the enzyme in the presence and absence of emulsion was the same and organic phase did not hinder enzyme performance. TSP-E-EMR and TSP-EMR reactors were also tested with triglycerides present in olive oil as substrate. It was observed that productivity increased from 5.2×10^{-4} mmol/min to 4.94×10^{-3} mmol/min. The results showed that the presence of the emulsion had significantly improved the catalytic activity in the reactor. The presence of emulsion increased the mass transport of the hydrophobic substrate through the membrane and immobilization improved enzyme stability [27].

In a study by Bohdziewicz [29], the possibility of phenol biodegradation in coke wastewater by enzymes isolated from a bacterial strain of *Pseudomonas sp.* was investigated. The enzyme was immobilized in the porous structure of an asymmetric polyacrylonitrile ultrafiltration membrane. The influence of process parameters such as transmembrane pressure (ΔP), stirring rate, and feed concentration of phenol on the effectiveness of ultrafiltration enzymatic membranes was systematically investigated.

When the transmembrane pressure was increased from 0.5×10^5 to 1.0×10^5 Pa the permeate flux increased at a 49% ratio. Further increasing in ΔP from 1.0×10^5 to 2.0×10^5 Pa and from 2×10^5 to 3.0×10^5 Pa increased the permeate flux by 57% and 23%, respectively. Nevertheless, it cannot be said that there is a linear relationship between the flux and the pressure for the enzymatic membranes examined. An increase in pressure does not always mean an increase in the flux. However, as the pressure increased in the range from 0.5×10^5 to 1.0×10^5 Pa the degree of phenol biodegradation also increased (from 23 to 33%). The stirring rate also affected both the permeate flux and the phenol biodegradation. An increase-in the stirring rate up to 500 rpm caused an 8% increase in the permeate flux. However, the degree of phenol biodegradation reached the maximum value (27%) at 400 rpm and did not change for stirring rate between 400 and 500 rpm. Feed concentration of phenol was tested for the range from 1 to 7 g/L. The permeate flux decreased by 6% when the phenol concentration was increased up to 7 g/L. Moreover, high degree of phenol biodegradation (from 10% to 38%) was achieved when phenol concentration was increased in the range from 1 to 7 g/L. The enzymatic membrane was also tested using coke wastewater. It was reported that the rate of filtration did not change over 18 h in the filtration process. The degree of phenol biodegradation increased from 36 to 57% during the first 3 h and then decreased and attained stability at 40% after 7 h. Deterioration in the enzymatic properties of the membrane was explained by the destructive influence of coke wastewater on the immobilized enzyme complex [29].

4.2. Chemically Immobilization on Polymeric Membranes

4.2.1. Covalent Attachment

Gupta et al. [30] have immobilized Lipase on polyvinyl alcohol photo modified polysulfone (PS–PVA) membranes. The maximum loading capacity for PS–PVA membranes was 1.48 mg/cm^2. It was observed that there

was a direct correlation between the amount of lipase, which can be immobilized on the membrane, and the PVA content in the PS–PVA membrane. The hydrolytic performance of both the lipase immobilized PS (lipase-PS) and lipase immobilized PS–PVA–glu (lipase- PS–PVA–glu) membranes were determined against olive oil and the free fatty acid (FFA %) and acid value (AV) for PS–PVA–glu, which were determined by titrimetric analysis, were found to be 1.53 and 3.04, respectively. The K_m and V_{max} values were found to be 105 mM and 0.9 mM/min for lipase-PS–PVA–glu and 153.8 mM and 0.51 mM/min for lipase-PS. Lipase-PS–PVA–glu membranes were found to be more stable than lipase-PS membranes. It was observed that after five cycles of use there was only 10.7% decrease in reusability of Lipase-PS–PVA–glu membranes whereas there was 33.3% decrease in reusability of Lipase-PS membranes. The reaction mechanism with PVA and glutaraldehyde is presented in Figure 7.

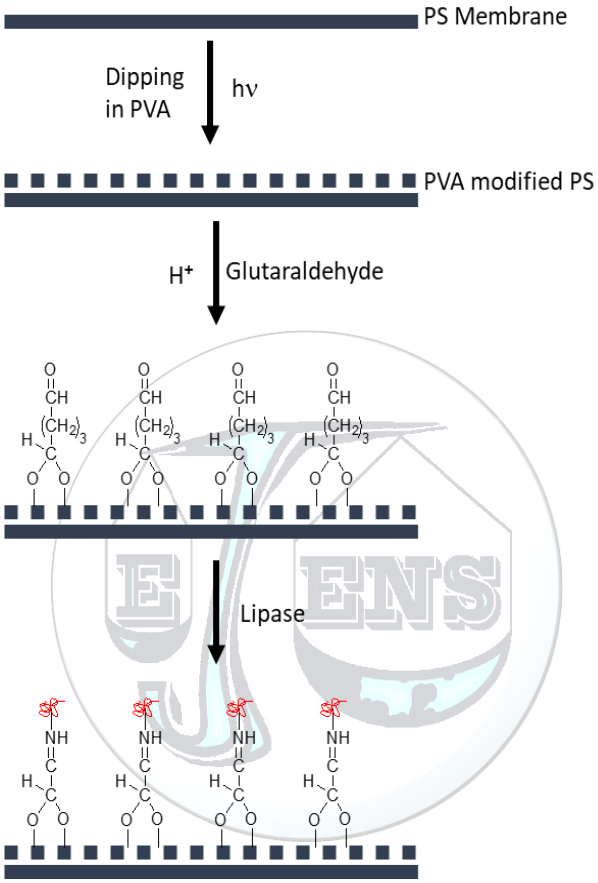

Figure 7. *Reaction mechanism for immobilization of lipase on PS–PVA using glutaraldehyde [30].*

It was reported that the amount of PVA on PS increases when dipping time increases and the efficiency of immobilization depends on the PVA content. Maximum amount of saturation, which was 2%, was observed to occur in 30 min. It was also observed that both for unmodified PS and PS–PVA membranes, glutaraldehyde concentration affects immobilization concentration which was found to be 2% for 30 min dipping time. It is expected that for other PS–PVA membranes it would be very similar. In this study, membrane surfaces were modified via photo-irradiation technique which was verified via FTIR, contact angle and pure water permeability measurements. It was observed that the longer the period the membranes were dipped in PVA solution the more PVA content was on the membranes [30].

The XRD and SEM results showed that lipase was successfully immobilized on the membranes. The change in the amount of immobilization was as follows: PS–PVA–glu[PS–glu[PS–PVA]. Covalent binding of glutaraldehyde in PS–PVA–glu membrane provided better immobilization efficiency than adsorption. As the amount of lipase on PS–PVA–glu membrane was more than that on the PS the total hydrolytic activity of lipase was found to be higher for PS–PVA–glu membranes. Among the factors of the hydrolytic reaction that influenced the hydrolytic activity pH, temperature and substrate concentration were investigated. Maximum hydrolytic activity was achieved at pH 8 and at 37 °C and at a concentration of 150 mM. As the acid values obtained via the titrimetric and GC methods indicate, the amount of free fatty acid (FFA) liberated by PS–PVA immobilized

membrane was more than that liberated by PS. The data obtained fit the two linear equations: Lineweaver–Burk and Hanes plot. When compared with PS membranes, higher hydrolytic reaction rate (V_{max}) was achieved with PS–PVA–glu membrane and the lower Km values obtained with Lipase-PS–PVA–glu membrane compared to that obtained with lipase-PS membrane indicates the greater affinity to olive oil. Upon investigating the reusability feature, it was found that Lipase-PS–PVA–glu was –lipase membrane had better stability [30].

Gulec et al. [31] investigated how surface characteristics, chemical and physical structure of the CA membrane surfaces affected the immobilization yield and the enzyme activity of unmodified and plasma modified cellulose acetate (CA) membranes affected efficiency of immobilization of –galactosidases obtained from Kluyveromyces lactic (KLG), which is an essential enzyme in food industry, and its galacto-oligosaccharide (GOS). Surfaces of CA membranes were modified via low pressure plasma treatments involving oxygen plasma activation, plasma polymerization (PlsP) of ethylenediamine (EDA) and PlsP of 2-mercaptoethanol. Through plasma polymerization the NH_2 and SH groups from EDA and 2-mercaptoethanol precursors could be incorporated onto the surface of CA membranes. Moreover, PEI could succefully be used to coat enzyme layers on EDA modified CA membrane surface upon plasma polymerization of the surface.

KLG enzyme was immobilized on unmodified and oxygen plasma treated membranes via physical binding. It was observed that CA membranes modified via oxygen plasma activation had higher hydrophylicity and immobilization efficiency increased by a factor of 42%. The enzyme, KGL, was covalently immobilized on CA membranes via amino groups created by PlsP of EDA. Activating the membrane via plasma at 60 W plasma power for 15 min. increased the amount of enzyme immobilized by 3.5-fold. When the amount of amino groups were enriched via polyethyleneimine (PEI) addition this 3.5-fold increase was observed to be 4.5-fold. Probably due to the adverse effect of the active amino groups although enzyme loading efficiency (65–83%) was high the enzyme activity and GOS yield dramatically decreased (11–12%). It was observed that CA membrane surfaces modified with thiol groups created by PlsP of 2-mercaptoethanol provided more effective immobilization of KLG enzyme with immobilization yield of 70% as well as high enzyme activity of 46%. Enzyme immobilized CA membranes treated by PlsP could be successively used for 5–8 cycles at 25 ◦C and the enzymatic derivatives could retain 75–80% of their initial activites after the cycles. Low temperature plasma is an important technique for modifying several polymeric membranes effectively [31].

It was observed that the techniques employed for immobilizing enzyme KLG had great impact on the apparent parameters of the enzyme-catalyzed reactions. The presence of KLG on membranes significantly changed the kinetics of GOS production. The GOS yield for separating monosaccharides from reaction mixture, selectively, was improved via PlsP of EDA modified CA membranes. High reactor productivity could be achieved via the combined system based on simultaneous production and separation with high enzyme loading. However, this system is still under development.

In a study by Hilal et al. [32] physical and chemical immobilization methods were used for immobilizing lipase enzyme on ultrafiltration membranes which were namely the regenerated cellulose (C030F) and polyethersulphone (PM30) membranes. In these methods, the lipase enzyme was either immobilized on the membrane via non-covalent method that is adsorption (Figure 8a), or it was incorporated in the membrane structure by filtration which was another noncovalent method or the enzyme was incorporated in the structure of the membrane via chemical method which was covalent attachment of lipase to the membrane (Figure 8b). These membranes were investigated for their catalytic properties in the reaction of butyloleate synthesis where the oleic acid was esterified with *n*-butanol in isooctane. The results showed that highly effective bio-catalytic membranes were prepared by inclusion of lipase in the wide pores of the supporting layer of the membrane. These lipase-immobilized bio-catalytic membranes provided oleic acid conversion at a degree of about 70–72% in a reaction time of 8 h. However, under the same experimental conditions, the bio-catalytic membranes obtained via adsorption or covalent immobilization of lipase could give substrate conversion of only 22–28 and 18–21%, respectively. The substrate conversion values were higher for membranes with filtration-immobilized lipase than those for membranes with adsorbed lipases since more lipase could be loaded on the membranes.

The study revealed that the distribution profile of the lipase in the membrane is an important factor in achieving effective enzyme utilization. Atomic Force Microscopy (AFM) was used for the profile imaging and the direct measurement of the interaction force between the lipase-coated tip and membrane surfaces. It was found that the direct measurement method is a useful and practical approach for choosing the right membranes as porous polymeric support for immobilizing lipase via adsorption [32].

The data on mass and area reaction rates indicate that at high enzyme loadings achieved in the filtration technique essential mass transfer is limited. The catalytic activity achieved in enzyme immobilization by filtration in the sponge layer of the asymmetric membranes provided higher catalytic activity compared to that obtained with the enzyme immobilized on the active membrane layer. In other words, the distribution profile of the lipase in the membrane has significant role on the effectiveness of immobilized enzyme. In a wide range of concentration, such

as 0.034–0.68 g protein/m^2, for enzyme loading a very small change of 63–72 and 43–48%, was achieved in the substrate conversion degree via the membranes with lipase immobilized in sponge or in active PM30 membrane layers, respectively. This indicates that not all the enzyme in the membrane is involved in the reaction. Hence, excessive loading of the enzyme in the membrane would not necessarily be beneficial.

C030F membrane on which the enzyme was adsorbed were more active in esterification reaction than the membrane on which the enzyme was covalently immobilized (Figure 8b). This may be due to conformational changes in the tertiary structure of the enzyme during its covalent immobilization on the membrane leading to some loss in the activity of the enzyme. In situations when a HMD spacer exists between the surface of the membrane and the chemically bound enzyme, negative effect of covalent immobilization decreases while the reaction rate of esterification increases.

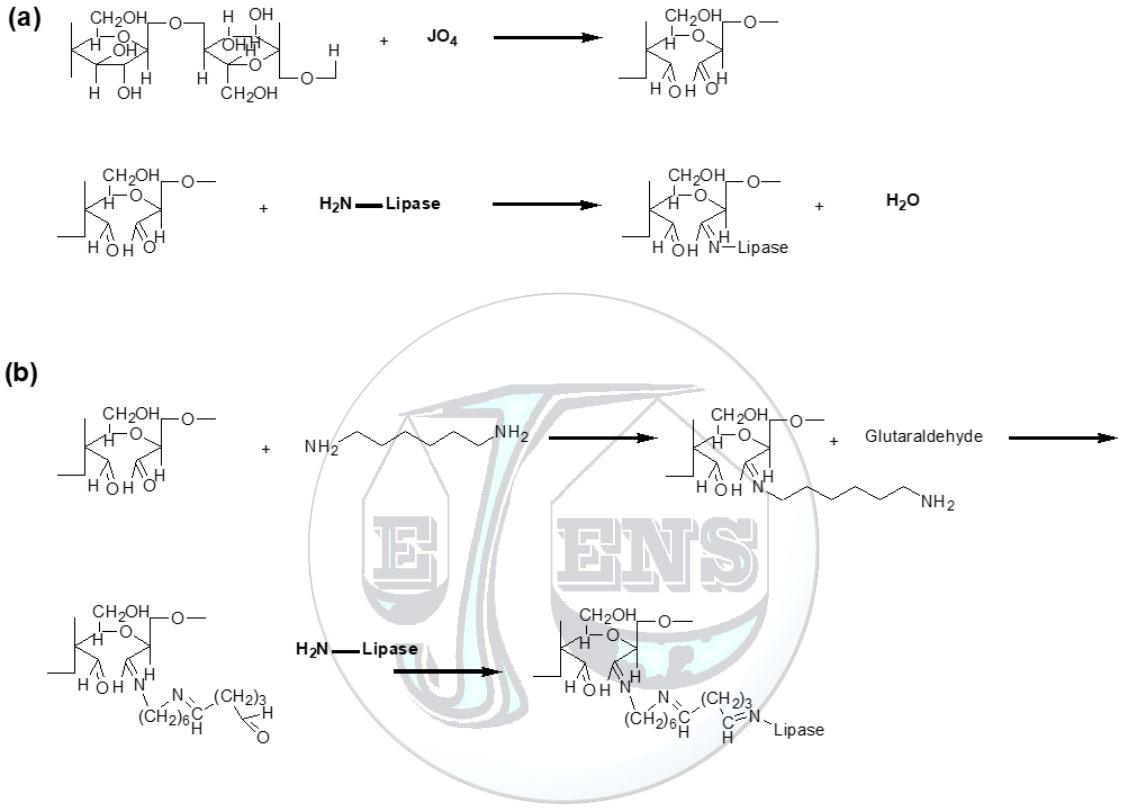

Figure 8. *Schematic presentation of chemical binding of the enzyme lipase on the cellulose C030F membrane without (a) and with (b) a HMD spacer [32].*

Vitola et al. [33] investigated the catalytic performance of a mutant, namely, SsoPoxW263F of the thermophilic Phosphotriesterase-like lactonase (PLL) isolated from Sulfolobus solfataricus (SsoPox). Lactonase was both introduced on free and immobilized membrane systems by using pesticide paraoxon as substrate. Bio-catalytic membrane systems which were obtained by immobilizing the single mutant on/into hydrophilic (Nonstandard grade Polyethersulphone, NGS-PES) and hydrophobic (Polyvinylidenefluoride, PVDF) membranes, could be used in the liquid and in the vapor phase for decontamination of water and air, respectively. stability of the developed systems was determined by investigating the vapor and water permeability, catalytic activity of the free and immobilized enzyme as well as enzyme stability of the membranes for a period of more than 5 months. The results showed that the free mutant showed a higher performance up to 30 days, but after two months' period it lost its activity completely. However, although the bio-catalytic membranes lost their activity in the first days almost no instability in a period more than 5 months. For instance, when the mutant was immobilized on/into NSG-PES, the residual specific activity was about 54% and when it was immobilized on/into PVDF the residual specific activity was about 5%. The residual specific activity could be enhanced by changing the amount of mutant immobilized on the PVDF membrane. A trade off was found between the amount of immobilized enzyme and the catalytic performance. While the residual specific activity could be improved for both bio-catalytic membranes sat least 5 months, the free system almost lost all its activity after two months. On the other hand, both bio-catalytic

membranes provided the same results in terms of vapor flux when water vapor was fed to them. This result may render this application the choice of preference in vapor phase decontamination applications [33].

Water and vapor permeance and flux through the native NSG-PES and functionalized NSG-PES-GA-SsoPox membranes and the relationship between these parameters and the pore size measurements before and after enzyme immobilization were measured. There was no considerable change in pore size, membrane wettability, water permeance and vapor flux after membrane biofunctionalization. Hence, it can be said that biofuctionalization process do not change the membrane properties [33].

4.2.2. Cross-linking

Atia et al. [21] investigated application of immobilized lipase enzyme on different radiation grafted polymeric films such as polypropylene (PP) and poly(tetrafluoroethylene-perfluroro-propyl vinyl ether) (PFA) using glutaraldehyde as cross linker. The polymeric membranes were modified by direct radiation grafting method and were grafted via Co60 γ-rays at a dose rate of 1.85 Gy/s. The modified membrane was activated by glutaraldehyde and lipase enzyme immobilized on the glutaraldehyde-activated membrane. The factors, which have pronounced effect on lipase activity such as graft yield, enzyme concentration, γ-irradiation, temperature, and pH, were systematically investigated. Activity of the immobilized lipase increased up to 178.5% upon grafting for PP, but it decreased when grafting was increased. This decrease in activity is attributed to the formation of multi bonds between lipase molecule and the PP-g-P(MAAc) membrane leading to increased AAc concentration. The immobilized lipase activity on PFA membrane increased with the percentage of grafting. Besides this increasing the amount of added protein resulted in a decrease in the activity of the retained enzyme. A study on the effect of γ-irradiation revealed that the free lipase lost about 50% of its relative activity when exposed to a dose of 2 Mrad and lost the rest of its activity upon exposure to a dose of about 5 Mrad. The results showed that irradiation at a dose of 5 Mrad caused no significant loss in the relative activity of the immobilized lipase. Immobilization of lipase on polymeric membranes had a shielding and stabilizing effect for the enzyme against radiation and the produced free radicals. The experimental results showed that the optimum temperature and pH were 40°C and 8.0, respectively, for free and immobilized lipase. The kinetic studies showed that the K_m value, which is a measure of the rate of reaction, decreased for immobilized lipase [21].

Gebreyohannes et al. [34] investigated the performance of an innovative magnetic responsive bio-catalytic membrane reactor (BMRSP) under various operational parameters. The effect of feed flow rate, temperature, feed concentration, and enzyme concentration were investigated via cross-linking of the pectinase enzyme (Figure 9).

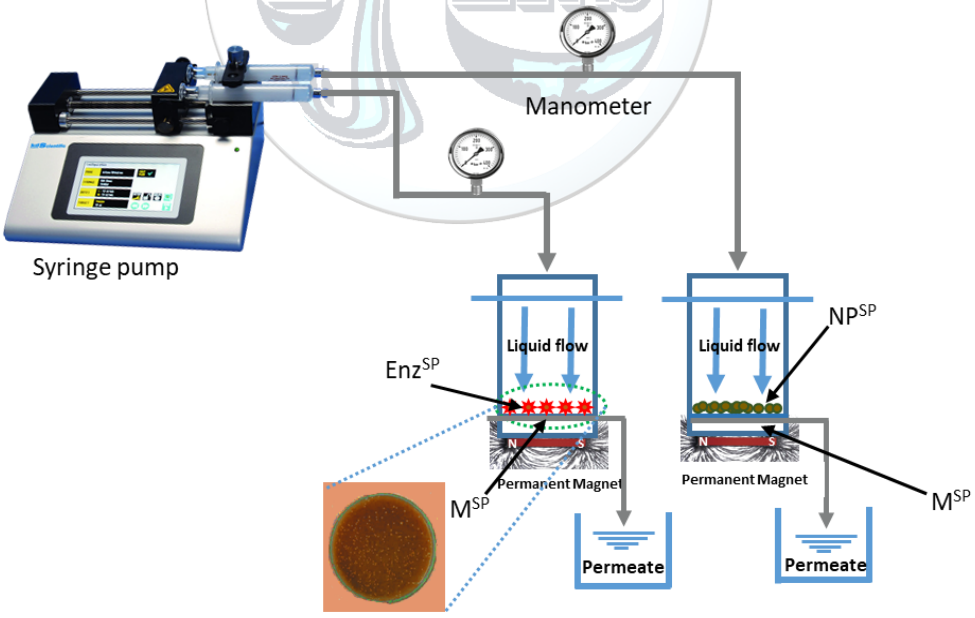

Figure 9. *Schematic illustration of the filtration set-up consisting of a syringe pump with two heads, two syringes each having 100 mL capacities, dead end filtration cell containing dynamic layer of pectinase activated magnetic nanoparticles (EnzSP), parallel control filtration cell containing dynamic layer of neutral magnetic nanoparticles (NPSP) and two parallel permeate tanks and digital manometers [34].*

It was observed that the feed flow rate affected the average degrees of conversion at 5, 15, 30 and 45 L/m^2 h as 28, 31, 28 and 34%, respectively. When the thermal stability of the BMRSP were tested in the temperature range between 25-40 °C, it was found 40 °C was the optimum temperature at which the enzyme pectinase provided the best efficiency. At 40 °C, the reaction rate was fast and accumulation of unreacted pectin was lower than that at 25 °C. At the lower temperature additional hydraulic resistance occurred and this induced a constant raise in the TMP.

Penicillin G acylase was immobilized on highly porous cellulose-based polymeric membrane in the presence of different ionic molecules/compounds which were used as ligand. The buffer flux at a pressure of 0.5 bars was 1,746 LMH (L m^{-2} h^{-1}). Activity of the immobilized enzyme was found to be around 250 UApp in the presence of a ligand such as proline, tryptophan, casein acid hydrolysate, and brilliant green. Different ligands provided different percentage immobilization yield (IMY%) and percentage of activity retention (RTA%). For instance, while the IMY % for proline was found to be less IMY% (—58) and the RTA% (— 71) higher, the specific activity was observed to be 145 UApp g^{-1}. However, when the brilliant green was prepared via crosslinking it via glutaraldehyde, activity of the immobilized enzyme was found to be 82±2.7% after a using it for successive five cycles. On the other side, when free enzyme was compared with the enzyme immobilized on the brilliant green coupled membrane it was observed that at there was 2.4-fold increase in K_m value (47.4 mM) and they had similar optimum pH, which was 7.2, and temperature, which was 40°C. The results showed that the immobilized enzyme retained almost 50% of its activity even being used for 50 cycles and after 107 days. However, after the enzyme immobilization the buffer flux decreased by almost 50%.

However, although after 30 cycles buffer flux decreased by 38%, this decrease reached a steady state after 16 cycles. The flux pattern is of great importance as this would be an important parameter in assessing the operation life of the membrane that hosts the enzyme. Almost a 50% decrease was observed in the buffer flux after the enzyme was immobilized. This shows that immobilization procedure affects pore size of the membrane. The results for 30 cycles of operation were studied. Although the average buffer flux observed after the first 1-15 cycles of operation was 655±83 LMH, it was 545±15 LMH for 16-30 cycles of operation. The studies showed that the average sample flux for the first 1- 15 cycles was 436±94 LMH, but for 16 to 30 cycles it was 310±11 LMH. These results indicate that the change in the flux value becomes less at higher numbers of cycles of operation and at even higher values it approaches a steady state. After 30 cycles of operation, the buffer flux pattern decreases by almost 38%. This indicates that around 60% active flux of the membrane remains intact and this value can be interpreted as the membrane has good operation life. In this study, it was observed that Proline selectively adsorbs penicillin G acylase, but the stability is less. The results indicate that stability may be enhanced if the binding chemistry is improved. The significant activity retention of Penicillin G acylase immobilized on the brilliant green coupled membrane and its storage and operational stability besides the flux pattern rendered it successful. This technology would be of preference of choice in industrial applications if an enzyme obtained from the modified microbial strain is used in immobilization [34].

Present work primarily deals with an exhaustive investigation on the effect of -galactosidase (EC 3.2.1.23) immobilization on polymeric polyether sulfone, cellulose triacetate and thin film composite polyamide membrane to produce galacto-oligosaccharides from lactose. Fouling is one of the key issues that control any membrane separation process to obtain the desired product. Especially, this issue with membrane becomes multiplied after making any attachment of immobilization chemicals on its surface, i.e. in case of enzymatic membrane reactor. Present work thus aims to identify the insights of carbohydrate interactions with the membrane surface after immobilization and how far it controls the production of galacto-oligosaccharides in this membrane reactor. Figure 10 shows the schematic representation of the membrane module used in this study.

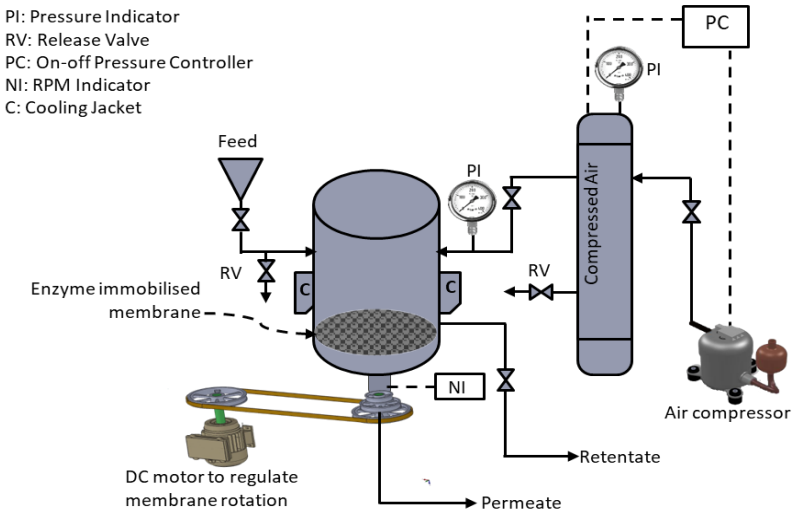

Figure 10. *Schematic representation of the experimental setup.*

Figure 11 shows the crosslinking of enzyme on polyamide NF membrane after immobilization.

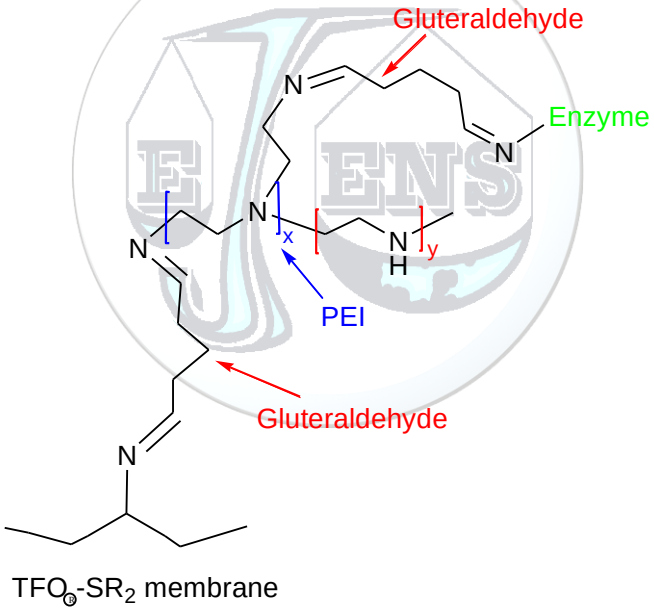

Figure 11. *Immobilized TFC®-SR2 membrane with β-galactosidase*

Glu259 amino acid residue acts as a nucleophile for β-galactosidase (EC 3.2.1.23; Uniprot A/C Number: O31341) from *B. circulans*. This catalytically active amino acid residue forms a hydrogen bond with the galactosyl moiety leading to a formation of enzyme-galactosyl complex (Figure 12).

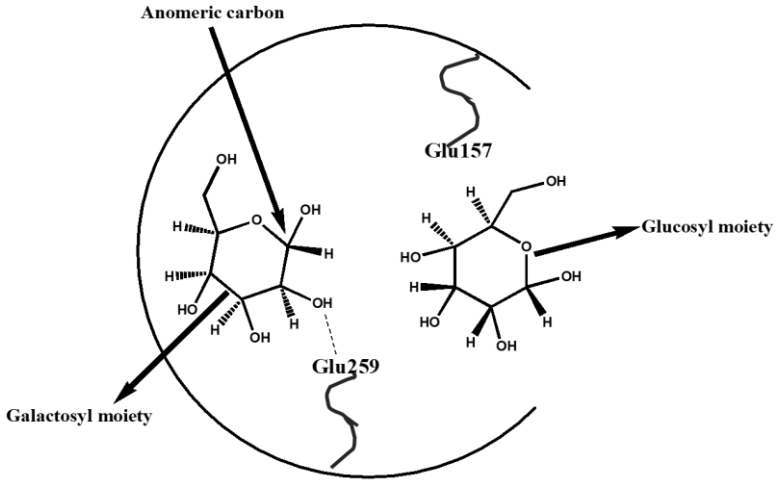

Figure 12. *Glu259 amino acid residue acts as a nucleophile for β-galactosidase*

Present study was an in-depth investigation on the reaction and separation of sugars with an enzyme immobilized membrane. Now from the observations it was seen that immobilization of enzyme on the polymeric membrane modifies the functional group presents on the surface and thus making some notable changes in the permeation characteristics of the membrane for carbohydrates. Especially immobilized CTA membrane shows more conversion compared to

the PES membrane, probably because of higher retention of lactose on the immobilized side. However, in any case the retention of monosaccharides was more with either PES or CTA, which is imparting an inhibitory effect on the enzymatic production of GOS. In comparison with the others, these immobilized NF membranes showed more convenient observations during GOS production. Although the requirement of high pressure with immobilized NF was one of the concerns, but in any way it shows good results with high separation for GOS and other sugars produced during the hydrolysis of lactose.

5. FUTURE PERSPECTIVE OF ENZYMATIC MEMBRANE REACTOR

Enzyme immobilization confers distinct advantages in bio-catalysis which provide more consistent performance and eco-friendliness. Among these advantages can be named

1) possibility of increasing control over reaction by separating the catalyst from the reagents and products,
2) reuse of the catalyst,
3) minimization or elimination of contamination of the products by the enzyme as well as of undesirable side reactions,

4) miniaturization, which brings along the advantage of improving the kinetic performance of enzymes, render these devices particularly preferable in analytical and biotechnological applications.

Although there are many different methods, materials, and enzymes which can provide this end, bio-micro reactors can be categorized under four main types:

1) Surface-immobilized enzymes: In this type, enzymes are bound to the surface of a pre-constituted micro reactor for instance by activating the inner channels of a capillary and then they are exposed to the reagent flow;

2) Enzyme activated beads: This type of bioreactors is prepared by functionalizing porous beads with enzymes and then filing them into the chamber of a micro reactor;

3) Enzyme-containing monoliths: meso- or macro porous monoliths are either previously coated with a resistant layer or are directly prepared in a microchannel. Then they are functionalized with enzymes; and

4) Membranes: In this type, the bioreactor is the selective ultrafiltration membrane onto which enzymes are immobilized [35].

6. CONCLUSIONS

As is presented in this review, enzymatic membrane reactors represent a very interesting and diverse area of research. They offer many different solutions for chemical and biochemical problems, with the underlying goal to enhance the selectivity and yield of complex reactions and separation. In particular, the development of selective

and reversible enzyme immobilization may allow for more versatile systems permitting potential reuse of the unit after the loss of enzymatic activity in enzymatic membrane reactors.

REFERENCES

[1] J.G.S. Marcano, T.T. Tsotsis, Catalytic membranes and membrane reactors, Online ISBN:9783527601981, Wiley-VCH Verlag GmbH, 2004.

[2] A. Asatekin, S. Kang, M. Elimelech, A.M. Mayes, Anti-fouling ultrafiltration membranes containing polyacrylonitrile-graft-poly(ethylene oxide) comb copolymer additives, J Membr. Sci. 298 (2007) 136–146.

[3] T. Uragami, S. Chakraborty, V. Piemonte, L.D. Paola, Biocatalytic membrane reactors: principles, preparation and biotechnological, pharmaceutical and medical applications, Handbook of membrane reactors, 2013.

[4] A. Al-Amoudi, R.W. Lovitt, Fouling strategies and the cleaning system of NF membranes and factors affecting cleaning efficiency, J. Membr. Sci. 303 (2007) 4–28.

[5] S. Shirazi, C. Lin, D. Chen, Inorganic fouling of pressure-driven membrane processes – a critical review, Desalination. 250 (2010) 236–248.

[6] N. Pena, S. Gallego, F. del Vigo, S.P. Chesters, Evaluating impact of fouling on reverse osmosis membranes performance, Desalin. Water Treat. iFirst (2012) 1–11.

[7] F.Afani au[Gabriele Iorio, G. Greco Jr., M. Cantarella, M.H. Remy, V. Scardi, Kinetic behaviour of immobilized enzyme membrane reactors, Chem. Eng. Sci. 34(10) (1979) 1213-1219.

[8] J. Agustian, A.H. Kamaruddin, S. Bhatia, Enzymatic membrane reactors: the determining factors in two separate phase operations, J. Chem. Technol. Biotechnol. 86 (2011) 1032–1048.

[9] F. Gao, X. Tang, H. Yi, S. Zhao, C. Li, J. Li, Y. Shi, X. Meng, A Review on selective catalytic reduction of NOx by NH3 over Mn–based catalysts at low temperatures: Catalysts, mechanisms, kinetics and DFT calculations, Catalysts 7 (2017) 199-231.

[10] P. Mäntsälä, J. Niemi, Enzymes: The biological catalysts of life. Physıology and Maintenance – Vol. II – Enzymes: The Biological Catalysts of Life.

[11] E. Piacentini, M. Yan, L. Giorno. Development of enzyme-loaded PVA microspheres by membrane emulsification, J. Membr. Sci. 524 (2017) 79-86.

[12] R.A. Sheldon, S. van Pelt. Enzyme immobilisation in biocatalysis: why, what and how. Chem. Soc. Rev. 42 (2013) 6223-6235.

[13] S.L. Matson, J.A. Quinn, Membrane reactors. In: Ho W.S.W., Sirkar K.K. (eds) Membrane Handbook. Springer, Boston, MA, 1992.

[14] K.K. Sirkar, V. Purushottam, A. Shanbhag, S. Kovvali, Membrane in a reactor: A functional perspective, Ind. Eng. Chem. Res. 38(10) (1999) 3715–3737.

[15] M. Amounas, C. Innocent, S. Cosnier, P. Seta, A membrane based reactor with an enzyme immobilized by an avidin–biotin molecular recognition in a polymer matrix. J. Membr. Sci. 176 (2000) 169-176.

[16] J.N. Talbert, J.M. Goddard, Enzymes on material surfaces, Colloids Surf. B: Biointerfaces 93 (2012) 8–19.

[17] C. Mateo, J.M. Palomo, G. Fernandez-Lorente, J.M. Guisan, R. Fernandez Lafuente, Improvement of enzyme activity, stability and selectivity via immobilization techniques, Enzym. Microb. Technol. 40 (2007) 1451–1463.

[18] P. Wang, H.F. Jia, G.Y. Zhu, Catalytic behaviours of enzymes attached to nanoparticles: the effect of particle mobility, Biotechnol. Bioeng. 84 (2003) 406–414.

[19] S.A. Ansari, Q. Husain, Potential applications of enzymes immobilized on/in nano materials: a review, Biotechnol. Adv. 30 (2012) 512–523.

[20] J. Lu, P.H. Toy, Organic polymer supports for synthesis and for reagent and catalyst immobilization, Chem. Rev. 109 (2009) 815–838.

[21] K. S. Atia, Characterization and application of immobilized lipase enzyme on different radiation grafted polymeric films: Assessment of the immobilization process using spectroscopic analysis, J Appl. Pol. Sci. 90(1) (2003) 155-167.

[22] N.R. Mohamad, N. H.C. Marzuki, N.A. Buang, F. Huyop, R.A. Wahab, An overview of technologies for immobilization of enzymes and surface analysis techniques for immobilized enzymes. Biotechnol Biotechnol Equip. 29(2) (2015) 205–220.

[23] S. Datta, L.R. Christena, Y.R.S. Rajaram. Enzyme immobilization: an overview on techniques and support materials. 3 Biotech. 3(1) (2013) 1–9.

[24] B.M. Brena, F. Batista-Viera, Enzyme immobilization literature survey from methods in biotechnology: Immobilization of enzymes and cells, Second Edition Edited by: J. M. Guisan © Humana Press Inc. Totowa, NJ.

[25] J. Fan, J. Luo, Y. Wan. Aquatic micro-pollutants removal with a biocatalytic membrane prepared by metal chelating affinity membrane chromatography. Chem. Eng. J. 327 (2017) 1011–1020.

[26] M.F. Chaplin, C. Bucke. Enzyme technology. Edition, illustrated. Publisher, CUP Archive, 1990. ISBN, 0521348846, 9780521348843. Length, 264 pages.

[27] L. Giorno, J. Zhang, E. Drioli, Study of mass transfer performance of naproxen acid and ester through a multiphase enzyme-loaded membrane system, J. Membr. Sci. 276(1-2) (2006) 59-67.

[28] F. Xu, W.H. Wang, Y.J. Tan, M.L. Bruening, Facile trypsin immobilization in polymeric membranes for rapid, efficient protein digestion, Anal. Chem. 82 (2010) 10045–10051.

[29] J. Bohdziewicz, Biodegradation of phenol by enzymes from Pseudomonas sp. immobilized onto ultrafiltration membranes, Process Biochem. 33(8) (1998) 811-818.

[30] S. Gupta, Y. Kumar, K. Singh. A. Bhattacharya, Lipase immobilized on poly (vinyl alcohol) modified polysulfone membrane: application in hydrolytic activities for olive oil, Polym. Bull. 64 (2010)141–158.

[31] H.A. Gülec, Immobilization of β-galactosidase from Kluyveromyces lactis onto polymeric membrane surfaces: Effect of surface characteristics, Colloids and Surfaces B: Biointerfaces 104 (2013) 83– 90.

[32] N. Hilal, V. Kochkodan, R. Nigmatullin, V. Goncharuk, L. Al-Khatib, Lipase-immobilized biocatalytic membranes for enzymatic esterification: Comparison of various approaches to membrane preparation. J. Membr. Sci. 268 (2006) 198–207.

[33] G. Vitola, R. Mazzei, E. Fontananova, E. Porzio, G. Manco, S.N. Gaeta, L.Giorno, Polymeric biocatalytic membranes with immobilized thermostable Phosphotriesterase, J. Membr. Sci. 516 (2016)144–151.

[34] A.Y. Gebreyohannes, L. Giorno, I.F.J. Vankelecom, T. Verbiest, P. Aimar, Effect of operational parameters on the performance of a magnetic responsive biocatalytic membrane reactor, Chem. Eng. J. 308 (2017) 853-862.

[35] E. Laurenti, A. dos Santos Vianna Jr. Enzymatic microreactors in biocatalysis: history, features, and future perspectives, Biocatalysis. 1 (2015) 148–165.

Journal Homepage: http://dergipark.gov.tr/ejens
EJENS
European Journal of Engineering and Natural Sciences
DergiPark AKADEMİK
CODEN: EJENS

Investigation of Notch Root Strain Behaviors Under Combined Loadings

Toros Arda Aksen[1]*, Emre Esener[2], Mehmet Firat[1]
[1]*Sakarya University, Department of Mechanical Engineering, 54187, Esentepe/Sakarya, Turkey.*
[2]*Bilecik Seyh Edebali University, Department of Mechanical Engineering 11210, Gulumbe/Bilecik, Turkey. *Corresponding*
Author email: ardaaksen@sakarya.edu.tr

Abstract

Notches are the stress raiser regions. Along the notch section, not only the stress distribution becomes non-uniform, but also the stress level reaches the maximum value. These geometrical disorders can be undesirable such as casting cavity but sometimes these disorders are created deliberately for assembly process such as keyway holes or shaft steps. Because of the necessity of these notches. This is important to understand material behavior along this region.

In this study, three different strain paths were generated by the cyclic tensile and torsional loadings and strains of the notch root of a shaft which contains circumferential notch, were investigated through the finite element method (FEM). MSC. Marc commercial program have been used in this study as finite element software. The results have been obtained for kinematic hardening rules and compared with the experimental results obtained from literature studies. Also in this study, a subroutine file was used to calculate the Chaboche kinematic hardening rule parameters according to Swift equation.

Key words

Cyclic Plasticity, Kinematic Hardening, Finite Element Method

1. INTRODUCTION

The main purpose of this study is to investigate the notch root strains for circumferentially notched bar under the combined stress situation using FEM and also examine the effect of the back stress value for kinematic hardening. MSC.Marc software was used for finite element simulations. Strain paths were created through the tensile loadings and torsial loadings together.

There is a lot of similar studies in literature. Neuber [1] examined the shear stress distribution on sharp notched prismatic material subjected to shear loading and developed a mathematical model establishing relationship between elastic stress concentration factor, elastic – plastic stress factor and strain factor. Crews Jr. [2] investigated notch root stress and strains under the cyclic loadings by using Neuber and modified Stowell equations for different materials SAE 4130 and 2024-T3 aluminum alloy which had the same notch geometry. Barkey [3] developed a method for calculating the elasto-plastic strains at notch root under multiaxial loadings and compared the results with the finite element analyzes results. He recorded that the finite element results were compatible with experimental results. Hoffman [4] realized FE analysis of a shaft which has circumferential notch under incremental axial loading, bending moments. Koettgen [5] et al. used notch stress calculation method suggested by Hoffman and Seeger on a fatigue assessment of preloaded fuel injection pump and compared notch stress –strain results with elasto plastic FE analyzes.

Moftakhar [6] calculated notch stress – strain of filled and empty both two shafts using FE method under incremental axial loading and bending loads and he obtained suitable correlations. Firat [7] modeled circumferentially notched round bar and fulfilled FE analysis under combined axial and torsion loading and he compared notch root deformations with the notch root strain history. For both elastic and elastoplastic notch deformations, he obtained suitable results. Firat [8] also proposed simplified method related to stress – strain calculations at notch root under bending – torsion loads for fatigue life predictions. This method is based on the total strain energy density and he performed in phase, out phase cyclic loading simulations of SAE 1045 steel under combined bending – torsion loads according to constant amplitude. Critical plane based multiaxial damage assessments was fulfilled through Smith – Watson – Topper and Fatemi – Socie criteria. For both criteria, suitable cycle predictions were obtained in comparison with crack initiation cycles.

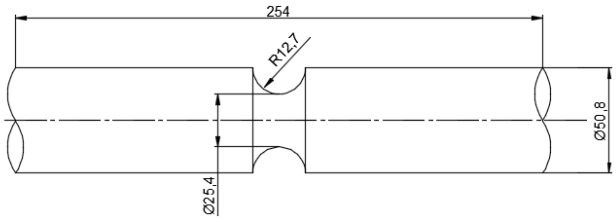

Figure 1. Circumferentially notched bar in 2D [3]

In this study, a circumferentially notched bar was modeled using Ansys software and the model was transferred to Marc finite element software. The dimensions of the circumferentially notched bar can be seen in Fig 1. Materials plastic properties were calculated according to Swift equation and the plastic parameters of the Swift equation were obtained from Hollomon parameters. In order to calculate materials plasticity parameters, a user subroutine file was used. This subroutine file requires Swift parameters for isotropic hardening solutions and besides the Swift parameters, saturation stress and saturation strain values for kinematic hardening solutions. So as to decrease solution time, because of the symmetry, half of the model was generated. Boundary condition of the half symmetric model can be shown in Fig 2.

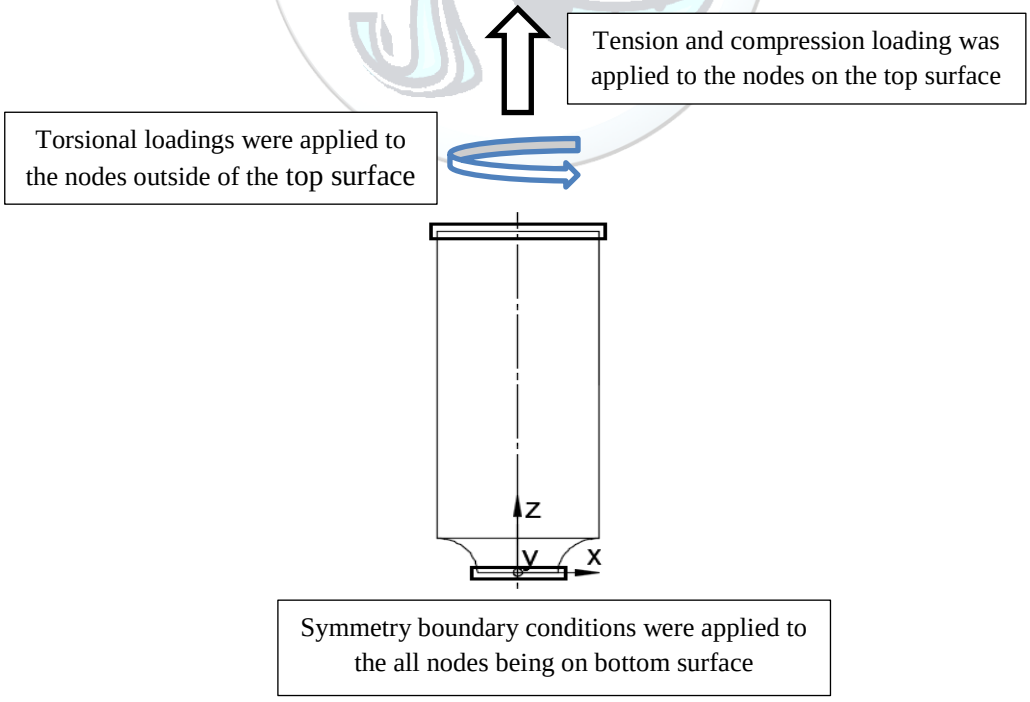

Figure 2. Boundary conditions applied on circumferentially notched bar in 2D

2. MATERIALS AND METHODS

2.1. Determination of Flow Curve

Material of the notched bar was determined as SAE1070 steel. The mechanical properties of SAE1070 steel were procured from the literature studies. The mechanical properties of the material are shown in Table 1.

Table 1. Mechanical properties of SAE1070 [3]

Parameter	Value
Young Modulus [MPa]	210000
Poisson Ratio	0,3
Yield Stress [MPa]	250
Cyclic Strength Coefficient [MPa]	1736
Cyclic Hardening Exponent	0,199

The stress values beyond the yield stress can be calculated according to power law equation shown in Eq. (1) [9].

$$\sigma_{True} = K . \varepsilon_p^n \quad (1)$$

In the equation above, K is the strength coefficient, n is the strain hardening exponent. Plastic strain which is expressed as ''ε_p'' can be calculated by the following equation.

$$\varepsilon_p = \varepsilon_T - \frac{\sigma_{True}}{E} \quad (2)$$

In this study, materials plastic parameters were calculated according to Swift equation and in order to obtain Swifts parameters, curve fitting method was implemented in Excel program. The flow curve obtained from the Hollomon power equation was matched with the Swift's equation. According to Swift's equation, true stress beyond the yield strength can be expressed by the following equation [9].

$$\sigma_{True} = C . (\varepsilon_0 + \varepsilon_p)^p \quad (3)$$

In Swift equation, C is the strength coefficient, p is the hardening exponent. To determine these parameters, curve fitting was applied and strength coefficient was obtained as 1800 MPa, hardening exponent was obtained as 0,215.

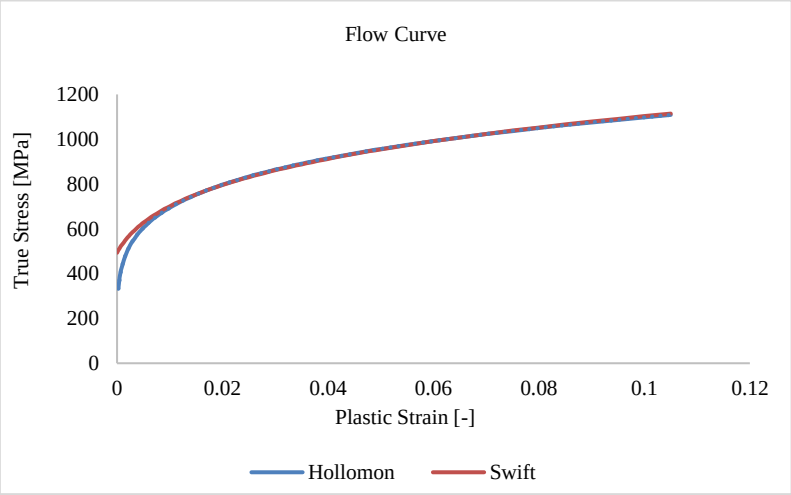

Figure 3. Curve fitting for Swift parameters

Along with the yield criteria and flow rule, hardening rule is required to define plasticity. Hardening rules describe the change of the yield surface and can be disintegrated into isotropic hardening and kinematic hardening rules. Backstress concept is associated with the kinematic hardening rule. Armstrong and Frederick expressed the backstress tensor increment as following equation [7], [8].

$$d\underline{\underline{\alpha}} = \frac{2}{3}\, C\, d\underline{\varepsilon}^{p} - \gamma\, \underline{\underline{\alpha}}\, dp \tag{4}$$

In Eq. (4), C and γ are the material constants; $d\underline{\varepsilon}^{p}$ and dp are the plastic strain tensor and equivalent plastic strain increment respectively. Chaboche and Rousselier disintegrated the back stress tensor into few parts which has different hardening properties. It is assumed that 5 parts will be adequate to calculate the plastic part of the material [7], [8], [10], [11], [14], [15].

$$\underline{\underline{a}} = \sum_{i=1}^{n} \underline{\underline{a}}^{(i)} \;; \quad i = 1,2,\dots,m \tag{5}$$

$$d\underline{\underline{\alpha}}^{(i)} = \frac{2}{3}\, C^{(i)}\, d\underline{\varepsilon}^{p} - \gamma^{(i)}\, \underline{\underline{\alpha}}\, dp \tag{6}$$

''i'' represents the arbitrary partition number which the back stress was divided. Equivalent plastic strain increment can be expressed as following inequality [7], [16].

$$0 \le dp^{(i)} \le \sqrt{\frac{2}{3}\, \underline{\underline{\varepsilon}}^{p}\, \underline{\underline{\varepsilon}}^{p}} \tag{7}$$

Jiang and Sehitoglu proposed another kinematic hardening model and define the backstress tensor increment as following equation [7], [14].

$$d\underline{\underline{\alpha}}^{(i)} = c^{(i)}\, .\, r^{(i)} .\left[\underline{\underline{n}} - \left(\frac{\left\|\underline{\underline{\alpha}}^{(i)}\right\|}{r^{(i)}}\right)^{(\chi)+1} .\, \underline{\underline{L}}^{(i)}\right] .\, dp \;; \quad i = 1,2,\dots,m \tag{8}$$

Here $c^{(i)}$, $r^{(i)}$ and $\chi^{(i)}$ are the scalar parameters; L is the unit tensor of the back stress tensor which can be expressed as following equation [7].

$$\underline{\underline{L}}^{(i)} = \frac{\underline{\underline{\alpha}}^{(i)}}{\left\|\underline{\underline{\alpha}}^{(i)}\right\|}; \quad (i = 1, 2, \dots, m) \tag{9}$$

n is the unit tensor of the yield surface normal which belongs to the related stress point and expressed by Eq. (10) [7], [12], [17].

$$\underline{\underline{n}} = \frac{\underline{\underline{S}} - \underline{\underline{\alpha}}}{\left\|\underline{\underline{S}} - \underline{\underline{\alpha}}\right\|} \tag{10}$$

Yield surface is the limit which the material can endure without exposed to any plastic deformation and can be define by following equation [7], [12].

$$F = \left\|\underline{\underline{S}} - \underline{\underline{\alpha}}\right\| - \sqrt{\frac{2}{3}} \cdot \sigma_0 \tag{11}$$

In Eq. (11), $\underline{\underline{S}}$ is the deviatoric stress component. According to the consistency condition, yield surface remains steady during plastic deformation as expressed in Eq. (12) [7] [12].

$$dF = 0 \tag{12}$$

Additionally, consistency condition can be expressed as Eq. (13).

$$d\underline{\underline{S}} : \underline{\underline{n}} - d\underline{\underline{\alpha}} : \underline{\underline{n}} = 0 \tag{13}$$

Plastic hardening modulus can be defined by Eq. (14).

$$h = \frac{d\underline{\underline{\alpha}} : \underline{\underline{n}}}{dp} \tag{14}$$

Through substituting Eq. (8) and Eq. (14), hardening modulus may be expressed as following equation [7], [12].

$$h = c^{(i)}\, r^{(i)} \left(1 - \left(\frac{\left\| \underline{\underline{\alpha}}^{(i)} \right\|}{r^{(i)}} \right)^{\chi^{(i)+1}} \underline{\underline{L}}^{(i)} : \underline{\underline{n}} \right); \quad (i = 1, 2, \dots, m) \tag{15}$$

$c^{(i)}$, $r^{(i)}$ which are also known as Jiang parameters can be calculated according to the following equations [7], [10], [11], [12], [14], [15].

$$c^{(i)} = \sqrt{\frac{2}{3}} \cdot \frac{1}{\underline{\varepsilon}^{p}_{a(i)}}; \quad i = 1,2,\dots,m \tag{11}$$

$$r^{(i)} = \frac{2}{3} \cdot \frac{H_{(i)} - H_{(i+1)}}{c^{(i)}}; \quad i = 1,2,\dots,m \tag{12}$$

In the Eq. (12), H represents the slope between two points in sequence which belong to the stabilized cyclic stress –strain curve [7]. These points have to be selected between yield stress and ultimate tensile stress. Slope of the curve can be calculated according to Eq. 13 [7], [12].

$$H_{(i)} = \frac{\sigma_{a(i)} - \sigma_{a(i-1)}}{\varepsilon^{p}_{a(i)} - \varepsilon^{p}_{a(i-1)}}; \quad i = 1,2,\dots,m \tag{13}$$

Hardening slope which belongs to the last point is zero. Other initial conditions are described in Eq. (14) [7], [10], [11], [12].

$$\sigma_{a(0)} = 0;\ \varepsilon_{a(0)} = 0;\ H_{(m+1)} = 0 \tag{14}$$

2.2. Finite Element Method

The model was generated in Ansys software. The coordinate systems of the nodes were transferred from the cartesian to cylindirical coordinate system and the boundary conditions were regulated for cylindirical coordinate system in Ansys. Then the model was transferred from Ansys to Marc software. Element density at the notch root was increased toward to the specimen surface because it is assumed that the stress level will reach the maximum level on surface.

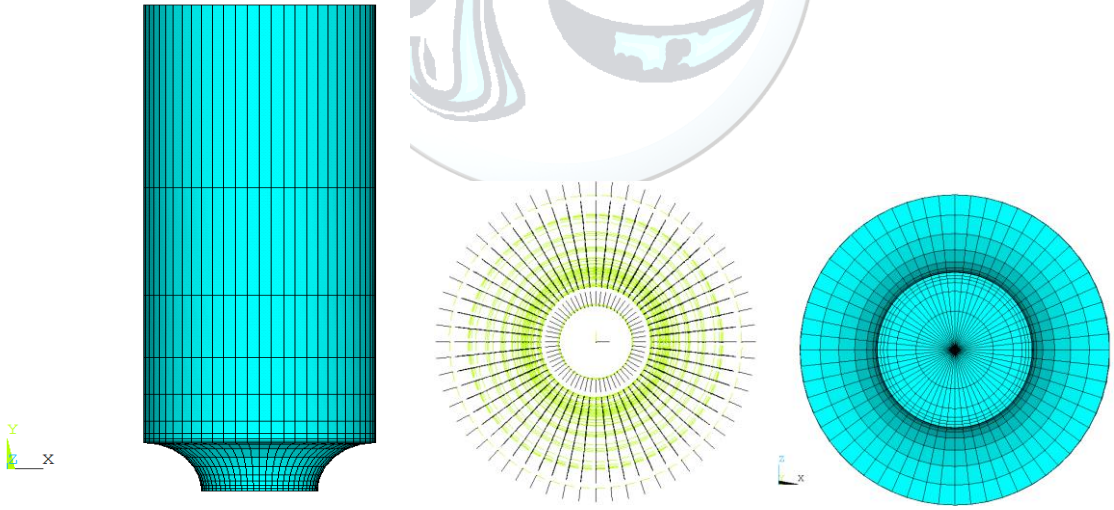

Figure 4. a) Model created through Ansys software. b) Cyl. coord. sys. of the nodes. c) Bottom view of the model.

In Fig. 5, green line represents Θ axis which is transformed from the y axis and black line represents the r axis which is transformed from the x axis. Also there is z axis in cylindirical coordinate system which is perpendicular to the r - Θ plane. The notched bar model transferred to Marc software can be seen in Fig 5.

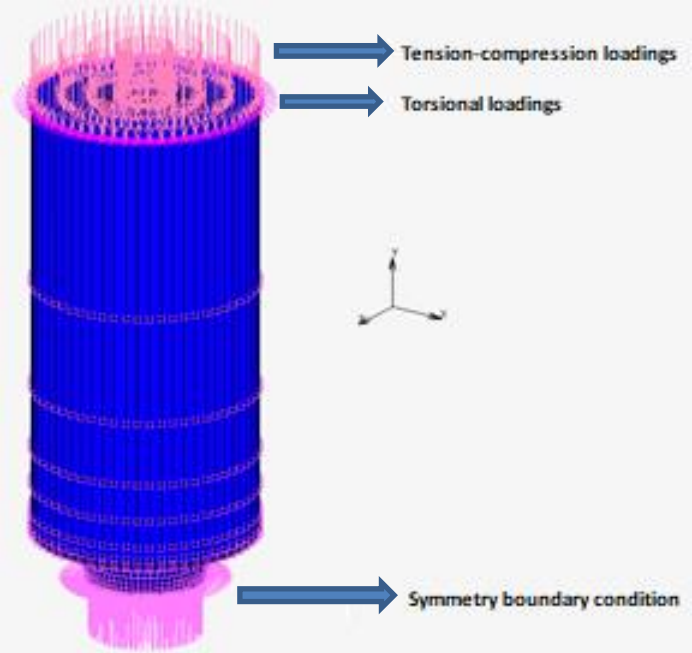

Figure 5. Model transferred to Marc software

2.2.1. Boundary Conditions

There strain paths which contain torsional and cyclic tension-compression loadings, were applied to the notched shaft. These strain paths are proportional loading, box type non-proportional loading and zig-zag type non-proportional loading, Strain paths can be shown in Fig 6.

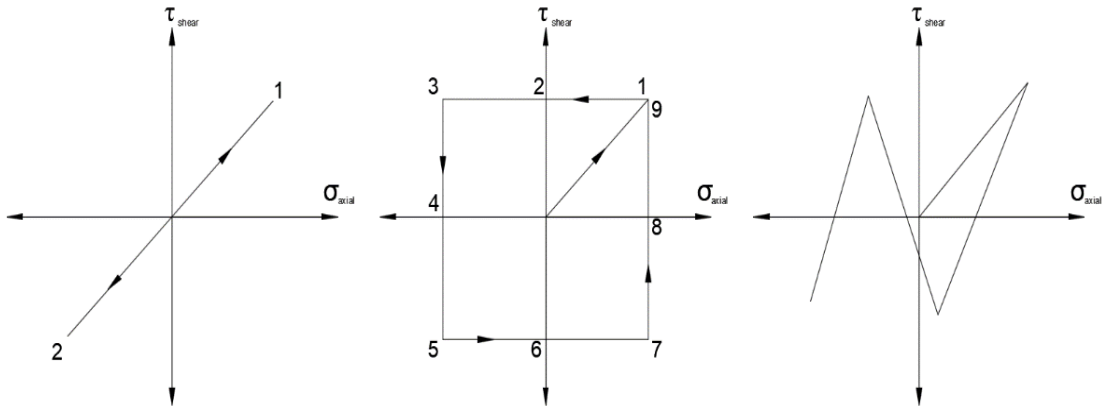

a) b) c)

Figure 6. a) Proportional loading, b) Box type non-proportional loading. c)Zig-zag type non-proportional loading [3], [7]

The stress occurred at the notch root is determined according to the nominal stress defined by Barkey. The nominal stresses created at the notch root can be seen in following table.

Table 2. Nominal stresses created at the notch root [3], [7]

Test Number	Nominal Axial Stress [MPa]	Nominal Shear Stress [MPa]	Loading Condition
1	296	193	Proportional Loading
2	296	193	Non-proportional Loading (Box)
3	296	193	Zig – Zag Type Loading

Because of the stress concentration at the notch root, the stress level reach the maximum level which is much more than the nominal stress. So, stress values in table 2 represent the stresses calculated at the notch root according to geometrical dimensions regardless of plastic deformation and stress concentration.

2.2.2. Subroutine File Regulations

A subroutine file called as Hypela 2 was used in this study for calculating the kinematic hardening rule parameters. In order to regulate the isotropic hardening parameters, in addition to the Young Modulus, Poisson ratio and yield stress, Swift parameters should be entered to the subroutine file. Besides the isotropic parameters, back stress components which are saturation stress and saturation strain data were entered to this subroutine file. Analyzes according to kinematic hardening rule assumptions were realized. To predict the accurate back stress parameters certain analyzes were performed in rows. First back stress parameters are determined by offsetting the flow curve to below as yield stress and the saturation stress value determined as 855 MPa for saturation strain equal to 0,1. According to the deviations and the convergence to the experimental results, the back stress parameters were updated at every turn until the appropriate results were obtained. The first saturation stress and saturation strain values obtained from the flow curve can be shown in Fig 7.

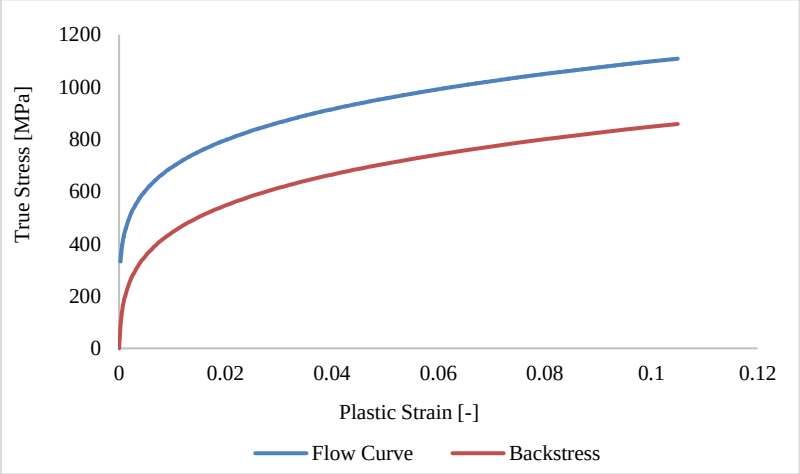

Figure 7. Saturation stress and saturation strain values obtained from the flow curve

3. RESULTS AND DISCUSSION

In order to examine strain behavior, a node which is located at the notch root, on the surface of the bar was examined. The results were compared with the experimental outcomes obtained by Barkey [3]. The results under proportional loadings can be shown in following Fig 8 for different saturation stresses.

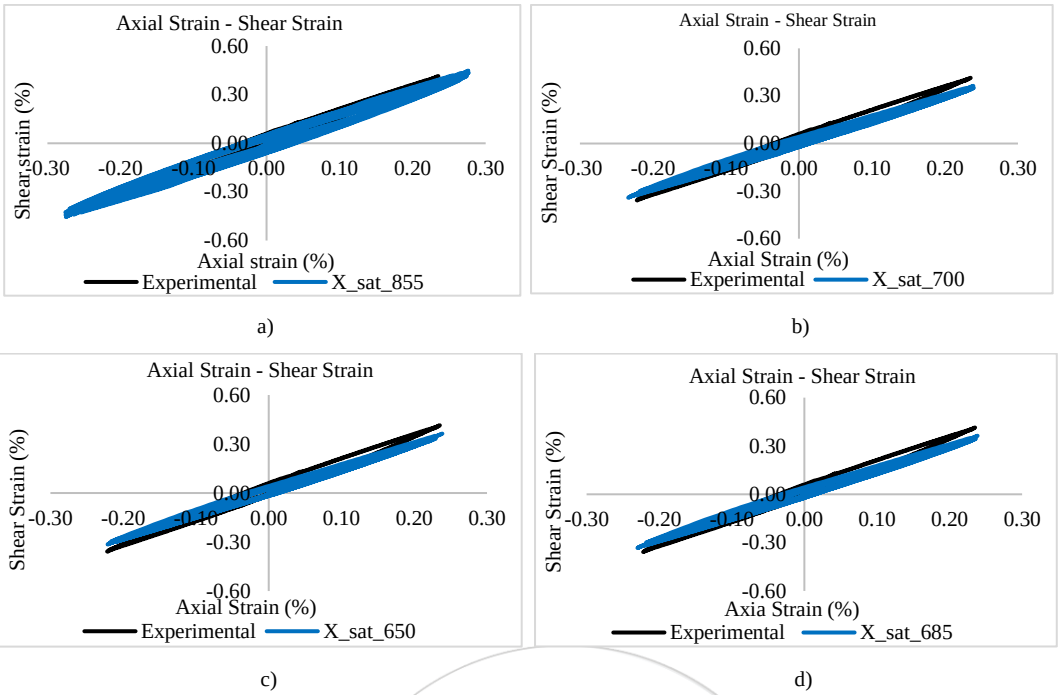

Figure 8. Axial strain – shear strain results under proportional loadings. a) Saturation stress 855 MPa, b) Saturation stress 700 MPa, c) Saturation stress 650 MPa, d) Saturation stress 685 MPa

The results under the box type non-proportional loadings can be shown in Fig 9 for different saturation stresses.

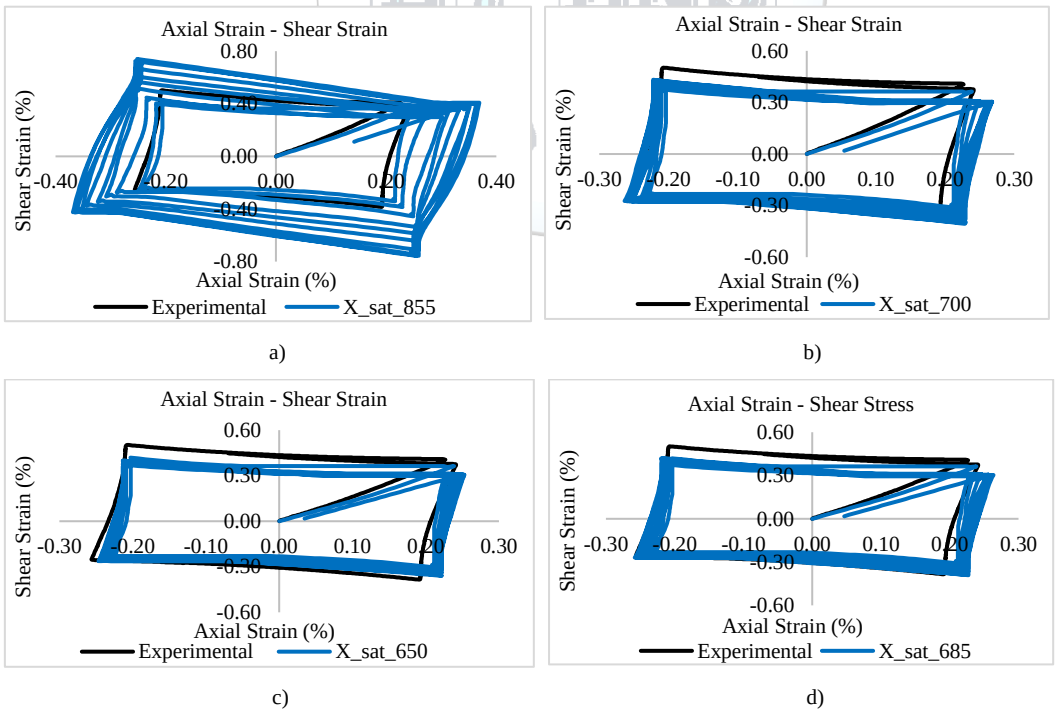

Figure 9. Axial strain – shear strain results under box type non-proportional loadings. a) Saturation stress 855 MPa, b) Saturation stress 700 MPa, c) Saturation stress 650 MPa, d) Saturation stress 685 MPa

The results under the zig-zag type non-proportional loadings can be shown in Fig 10 for different saturation stresses.

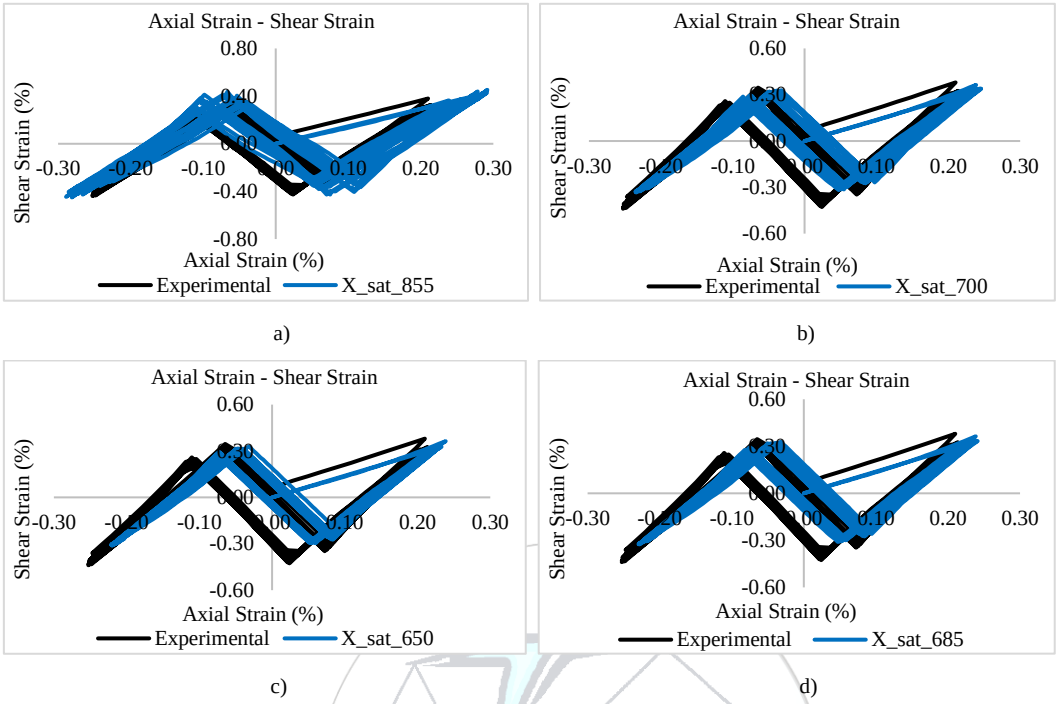

Figure 10. Axial strain – shear strain results under zig-zag type non-proportional loadings. a) Saturation stress 855 MPa, b) Saturation stress 700 MPa, c) Saturation stress 650 MPa, d) Saturation stress 685 MPa

4. CONCLUSION

In this study, under the combined loadings, notch root strain behaviors of a circumferentially notched bar were investigated. These combined loadings were proportional loadings, box type non-proportional loadings and zig-zag type non-proportional loadings. Analysis were performed according to the kinematic hardening rule assumptions. To define the kinematic hardening rule parameters, a user subroutine file was used and the plasticity calculations were realized according to Swift equation. Swift parameters were obtained from the Hollomon parameters which were procured from the literature studies. In order to calculate the back stress, saturation stress values were updated repeatedly. Then the solutions were compared with the experimental results.

It can be seen that the results were in accord with the experimental data. For all loading types, this is similar that, the results obtained according to 855 MPa saturation value, showed deviations in comparison with the experiments. Then the saturation stress values were updated to 700 MPa, 650 MPa and 685 MPa respectively. The results were close to each other and the deviations were fell off. For the results obtained according to the 650 MPa saturation stress, deviations were the lowest but the results diverged from the experimental results. The optimal results were obtained according to the saturation stress equal to the 685 MPa because the outcomes were in accord with the experimental results and the deviations were lower. In addition, calculating the strain behaviors at notch root according to the different back stress values is difficult and time consuming process. In this study this process accomplished readily through a user subroutine file.

REFERENCES

[1]. H. Neuber, ‘’Theory of stress concentration for shear strained prismatic bodies with arbitrary stress – strain law,’’ Journal of Applied Mechanics, vol 28, pp. 544-550, Dec. 1961.

[2]. H. J. Crews, ‘’Elastoplastic stress – strain behaviour at notch roots in sheet speciments under constant – amplitude loading,’’ Langley Research center, NASA Technical Report, D-5253, 1969.

[3]. Barkey, M., E., ‘’Calculation of notch strains under multiaxial nominal loading,’’Ph.D. thesis, University of Illinois, College of Engineering at Urbana-Champaign, Oct. 1993.
[4]. M. Hoffmann,*’’*Ein naeherungsverfahren zur ermittlung mehrachsig elastisch-plastischer kerbbeanspruchungen’’, M.Eng thesis, Darmstadt Technical University, Germany, 1985.
[5]. V.B. Koettgen, M. Schoen, and T. Seeger, *’’*Application of multiaxial load notch strain approximitation procedure to autofrettage of pressurized components, *’’American Society for Testing and Materials*, pp. 375-396, 1993.
[6]. A.A. Moftakhar,’’Calculation of time – independent and time – dependent strains and stresses in notches,’’ M.Eng. thesis, Univercity of Waterloo,1994.
[7]. M.Firat,’’Cyclic plasticity modeling and finite element analysis of a circumferentially notched round bar under combined axial and torsion loadings*’’*, Material and Design, vol. 34, pp 842-852, Feb. 2012.
[8]. M. Firat, “A numerical analysis of combined bending – torsion fatigue of SAE notched shaft,” *Finite Elemenst in Analysis and Design*, vol. 54, pp. 16-27, 2012.
[9]. G. E. Dieter, *Mechanical Metalurgy*, SI metric ed., United Kingdom, 1988.
[10]. M. Firat, U. Kocabicak,’’Analytical durability modeling and evaluation – complementary techniques for physical testing of automotive components,’’ Engineering Failure Analysis, vol. 11, pp. 655–674, 2004.
[11]. M. Firat, U. Kocabicak,’’A simple approach for multiaxial fatigue damage prediction based on FEM post-processing,’’ Materials and Design, vol. 25, pp. 73–82, 2003.
[12]. M.Firat,’’U-channel forming analysis with an emphasis on springback deformation,’’ Material and Design, vol. 28, pp 147-154, Feb. 2007.
[13]. Y. K. Lin, K. M. Hsu and P.K. Lee, ‘’The application of flow stress flow stress model to sheet metal forming simulation,’’ Iron & Steel Research & Development Department, China Steel Technical Report, No 23, pp.31-35, 2010.
[14]. Y. Jiang and H. Sehitoglu,’’ Modeling of cyclic ratchetting plasticity, part I: development of constitutive relations,’’ Journal of Applied Mechanics, vol. 63, pp. 720-725, Sept 1996.
[15]. Y. Jiang and H. Sehitoglu,’’ Modeling of cyclic ratchetting plasticity, part II: comparison of model simulations with experiments,’’ Journal of Applied Mechanics, vol. 63, pp. 726-733, Sept 1996.
[16]. N. Ohno and J. D.Wang,“Kinematic hardening rules with critical state of dynamic recovery, part I: formulation and basic features for ratcheting behavior”, International Journal of Plasticity, vol. 9, pp. 375-390-650, 1993.
[17]. J. Lemaitre and J. L. Chaboche, “Mechanics of Solid Materials”, Cambridge University Press, New York, 1990.

Journal Homepage : http://dergipark.gov.tr/ejens
EJENS
European Journal of Engineering and Natural Sciences
CODEN: EJENS
DergiPark AKADEMİK

The Investigation and Comparison of Friction Stir Spot Welding and Electrical Resistance Spot Welding of AA2024 Aluminium Alloy Joints

Yahya Bozkurt[1]*, Adnan Türker[2], Gamze Soytemiz[1], Serdar Salman[3]
[1]*Marmara University, Faculty of Technology, Department of Metallurgy and Materials Engineering, 34722, Kadıköy/İstanbul, Turkey.*
[2]*National Defence University, The NCO Vocational High School, Department of Mechanical Science, Balıkesir, Turkey.*
[3]*National Defence University, Rectorate of National Defence University, Turkey.*
**Corresponding Author email: ybozkurt@marmara.edu.tr*

Abstract

Both Friction Stir Spot Welding (FSSW) and Electrical Resistance Spot Welding (ERSW) are contemporary techniques for joint of the thin sheet materials. But FSSW is more modern technique than RSW. FSSW is used a lot of area which are from marine to aerospace industries. Aluminium alloy has a lot of advantages of the other materials. One of them is weight. In this study, AA2024 sheets are chosen for FSSW and RSW joint. FSSW is effected with tool rotational speed, tool transverse speed, dwell time and tool plunge depth. Two sheets were joined under the tool rotational speed for 1040 rpm and dwell time for 10 second. The same samples joints with under RSW for 39 kA and dwell time for 0.5 second. These parameters are optimized for both welding techniques. Afterwards FSSW and RSW are compared about lap shear tensile test for aluminum alloy joints with plane thickness of 1.6 mm. So that FSSW is more suitable joining process than ERSW. As a results of test and analyses are showed that FSSW is better mechanical properties than RSW. Eventually, These results are verified by many experiments.

Key words

Friction Stir Spot Welding, Electrical Resistance Spot Welding, Aluminium alloys, Mechanical properties,Welding parameters.

1. INTRODUCTION

The ERSW method group (group of pressure welding method) has a wide range of applications in the automotive industry. This welding operation takes place in the solid phase. Especially, the ERSW used in automobile body sheet production is made by robots because this method is suitable for serial production [1]. ERSW is welding method which heat from the resistance of the materials against the electric current passing through the work pieces and at the same time applying the pressure. Apart from the heat generated by the electric current passing through the material, no heat treatment is applied to the work pieces. The heat is generated around the welded zone and pressure on this welded zone by applied through the electrodes [2]. However, the difficulties welding aluminum alloy which is a soft material with the RSW, have delayed widespread use of aluminum alloys in the automobile body sheet production [3]. A schematic presentation of the ERSW process is shown in Fig. 1 [4].

FSSW method recently advanced as an alternative to ERSW and developed from the traditional friction stir welding (FSW) method, it is one of the latest developments in joining technology [4].

In Figure 2, the steps of the FSSW technique is shown. The process is used for joined two metal plates. A non-consumable rotating tool with a specially designed pin plunges into upper plate. A support tool underneath the lower plate provides the force against the shoulder and pin (Fig. 2a). The tool accomplish two important function: heat generation hereabouts weld zone, and movement of material to produce the weld (Fig 2b). The heating is served by friction between the tool and the plastic deformation of the plates (Fig 2c) [5].

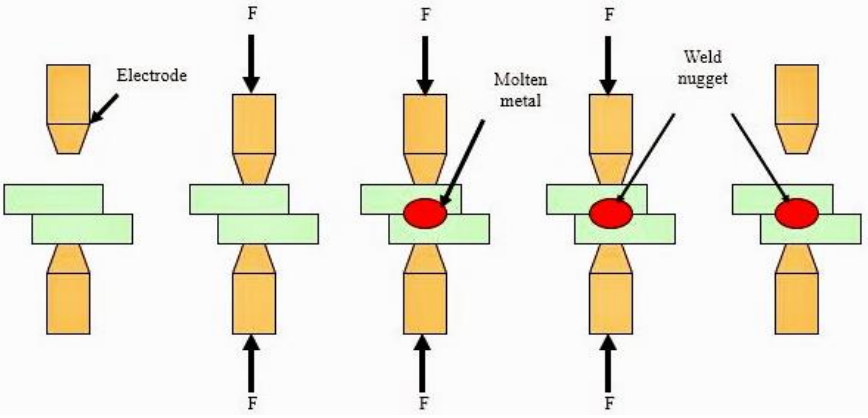

Figure 1. A schematic presentation of the ERSW process [5].

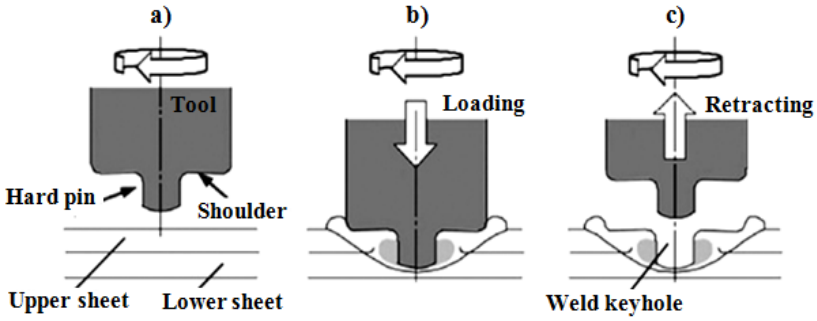

Figure. 2. A schematic presentation of the FSSW process: (a) plunging; (b) bonding; (c) drawing out [6].

After the FSSW process, the weld zone is observed as shown Figure 3. Two special segment can be identified from weld zone. The first segment is the thickness of weld nugget (X) which is a determiner of the weld (bond) section (Figure 3a and 3b). The bond section size is changed of depending of nugget thickness. The second segment is thickness of subject to shoulder operation on the upper plate (Y). The size of these segment establish the strength of a FSSW joint [7].

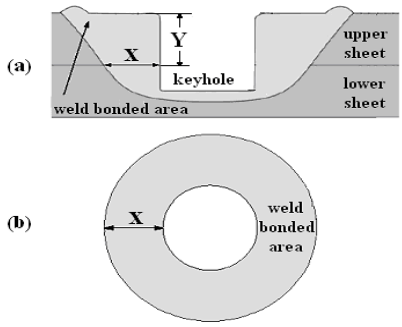

Figure. 3. (a) Schematic presentation of the cross section of a FSSW and (b) geometry of the weld bonded area; x: nugget thickness and y: the thickness of the upper sheet [7].

A new solid state welding technique, FSSW has been developed by Mazda Motor Corporation and Kawasaki Heavy Industry, as an extension of FSW for joining aluminum alloys [8-9]. Mazda reported a great reduction in energy consumption and equipment investment compare to ERSW for aluminum [10]. The only energy consumed in FSSW is the electricity needed to rotating and drive the tool. Compared to ERSW, the energy consumption has reduced by 99% for FSSW of aluminum and 80% for steel [11].

Since FSSW is a solid state welding process, no compressed air and coolant are need, and less electricity is required than ERSW. FSSWs have higher strength, better fatigue life, lower distortion, less residual stress and better corrosion resistance. Unlike ERSW, there is no traverse movement after plunging a rotating non-consumable tool into the work pieces. Tools used for FSSW have two parts, a pin and a shoulder. The pin is projected to throw the faying surface of the work pieces, shear and transport the material around it and produce deformational and frictional heat in the thick work pieces. The tool shoulder produces a majority of frictional heat to the upper surface and lower plate zones of the work pieces. Also the shoulder constrains the flow of plasticized material and produces the downward forging action [12].

In this study, sheet materials AA2024-T3 were selected for the ERSW and FSSW methods used in the industry. These selected sheets were separately welded with RSW and FSSW. The tensile test of welded joins was carried out. In addition, these test results were examined comparatively.

2. EXPERIMENTAL STUDY

2.1. Materials

In this study, 2 mm thickness AA2024-T3 plates were used for dissimilar FSSW and ERSW. The chemical composition of these alloy sheets is shown in Table 1.

Table 1. The mechanical properties and chemical composition of the aluminum plates.

Alloy	Mechanical properties		Chemical composition (wt. %)								
	Tensile strength (MPa	Elongation (%)	Al	Si	Fe	Cu	Mn	Mg	Zn	Ti	Cr
AA2024-T3	435	17	93.11	0.07	0.14	4.5	0.65	1.5	0.01	0.02	-

Aluminium plate dimension is 25x100 mm. The welding zone is fixed as 25x25 mm for all test specimens.

All the FSSW experiments were carried on FSW adjusted milling machine as shown in Fig 4.

Figure 4. FSSW process: a) rotating tool prior to penetration into the lap joint; b) tool shoulder makes contact with the part, making heat and the joint zone; c) retraction of the tool from the lap joint zone.

2.2 Preparation and Joint of Experimental Specimens

The FSSW tool was made of Aluminum Titanium Nitrate (AlTiN) coated, 1.2344 hot work tool steel and had a hardness of 58 HRC. FSSW tool had a shoulder diameters of 18 mm, a pin diameter of 6 mm and a pin length of 3.80 mm. Joint configuration was used to produce the FSSW joints where the rolling direction of the plates. All the welding processes were done at the room temperature. FSSW process rotating tool have a constant speed that 1040 rpm. Dwell time of the tool was determined as 10s.

During the ERSW process, the specimens were joined at the current values of 39 kA with constant welding time of 0.5s and a constant electrode force of 1710 N which is the same in each joining.

2.3 Lap Shear Tensile Test

Welded plate pairs are tested with 250 kN capacity tester at 30 mm/min. tensile speed. The test equipment's trademark is ZWICK Z010. The lap-shear tensile tests (LSTT) were carried out at room temperature by Zwick Z010 universal type tensile test machine at a constant crosshead speed of 5 mm/s. The load and displacement were simultaneously recorded during the test.

Figure 5. Zwick Z010 lap-shear tensile tests machine.

Three specimens were tested for each parameter from the specimens joined by ERSW and FSSW and the averages were taken. ERSW and FSSW welded specimens plates (AA2024) are shown in Figure 6a and 6b.

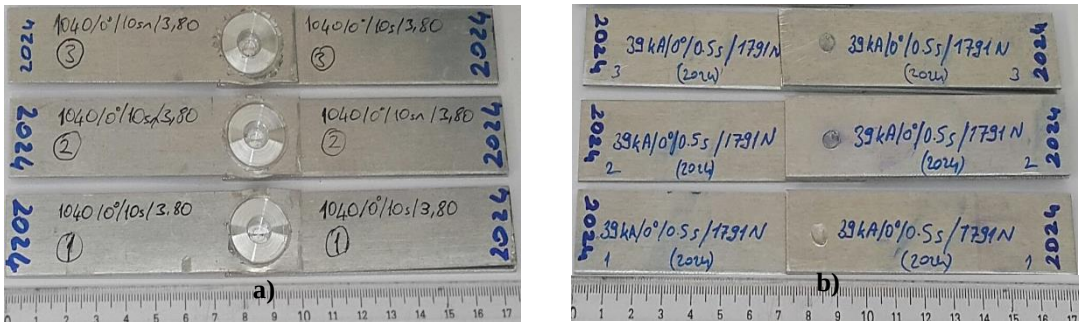

Figure 6. Lap-shear tensile tests specimens: a) Before test of FSSW specimens; b) Before test of ERSW specimens.

3. RESULTS AND DISCUSSION

3.1 Results of LSTT

The LSTT results of specimens joined with ERSW and FSSW are shown in Table 2. The results are given graphically in Figure 7. Increasing the weld current value causes inner heat rising and result of this operation nucleus grows.

Weld nucleus diameter is smaller in lower weld time and weld current values. It is also reported in other studies that heat input increases when weld current and time increased as formulated below; [13].

$Q = I^2 \cdot R \cdot t$

where Q is the generated heat (J), I the current (Ampere), R the resistance of the work (Ω) and t the time of current (s).

The expansion of weld nucleus and heat affected zone with increase in heat input is an expected result [14-19]. Bonding occurred at 9kA - 40kA but bonding was not happened at 3kA - 10 kA cycles. Bonding occurred at higher heat input. Rising the weld metal size increases the tensile-shear force. As the current continues to rise, the size of the weld metal decreases due to excessive melting and splashing and therefore the tensile-shear force is also reduced [13].

Aslanlar et al. 2006 showed that In low welding currents achieved by increasing the welding time, the amount of fused metal to form a nucleus increase, so the nucleus diameter increases and the height of the nucleus nearly reaches the sheet thickness [13].

LSTT was performed to obtain information on the joint strength of AA2024 plates joined with FSSW technique and ERSW technique. Thus, the yield strength, tensile shear strength and % elongation value of the material were determined. During the tensile tests a time must be given to distribute the uniformity of the applied stress uniformly throughout the sample.

Table 2. The LSTT results.

Materials	LSTT (kN)	
	FSSW	ERSW
AA2024	4.74	2.07
	8.31	3.38
	7.3	2.72

In FSSW process, the tool plunge depth up to 3.80 mm increases of tensile-shear force and decreases after this depth. The reason for this, the tool excessively depth process on the Al-alloy plate during the FSSW that causes thinning in the weld zone on the top surface of the plate [20].

The variation in pin length and pin profiles has direct impact on material mixing, flow etc. The commonly used pin profiles are cylindrical, conical, threaded, square, octagonal etc [21]. During FSSW process, the plunge depth and dwelling time of the tool determine the flow of metal around the stirrer tip, heat generation, weld strength and geometry [22].

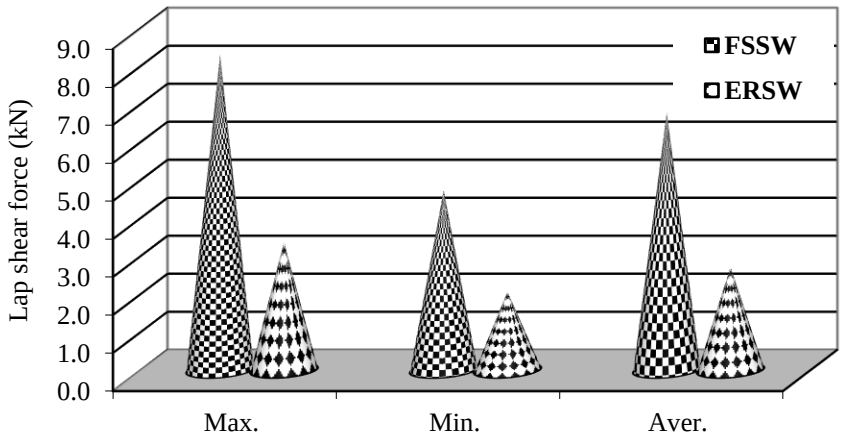

Figure 7. The lap-shear test results of specimens Joined with RSW and FSSW.

The weld metal is similar to the tool pin used in FSSW process. The shoulder of tool causes burr formation during the plunge. This situation is compatible with literature because it is formed in this way in all studies and is allowed to collapse on surface of upper material [4].

4. CONCLUSIONS

In this study, AA2024 Aluminium alloy sheets were joined with FSSW and ERSW methods. Maximum and minimum LSTT were determined. During the ERSW process, maximum LSTT force was determined to be 3.38 kN, a current value of 39 kA, a welding time (constant) of 10 s, an electrode force (constant) of 1710 N. During the FSSW process, maximum lap-shear force was determined to be 8.31 kN, a tool rotation speed of 1040 rpm, a dwelling time of tool of 10 s and a plunge depth of 3.80 mm. When these results were evaluated, FSSW method is given better results than ERSW method. As a result of increasing the welding current, the heat input and size of weld nucleus increased.

ACKNOWLEDGMENT

This study is granted by Marmara University, BAPKO project numbers: FEN-C-YLP-150218-0059.

REFERENCES

[1]. M. H. Coşkun, ‘’Otomotiv endüstrisinde kullanılan AN 7114 ve Dp600 Çelik Sacların Direnç Nokta Kaynağı (RSW) ve Sürtünme Karıştırma Nokta Kaynağı (FSSW) Yöntemleri ile Birleştirilmesi,’’ Kocaeli Unv. Fen Bil. Enst., 2009.
[2]. A.Bilal, ‘’AA 2024-T3 Alüminyum Alaşımının Sürtünme Karıştırma Kaynağında İşlem Parametrelerinin Mikroyapı ve Mekanik Özelliklere Etkileri,’’ Osmangazi Unv. Fen Bil. Enst., 2006.
[3]. G. Çam, ‘’Sürtünme Karıştırma Kaynağı Uygulamalarında Son Gelişmeler,’’ Kaynak Tekn. VI. Kongre ve Sergisi Bildiriler Kitabı, TMMOB Makine Mühendisleri Odası, 2007, p. 449, 42.
[4]. http://mechanicalinventions.blogspot.com.tr/2014/09/resistance-spot-welding-rsw-working-principle.html
[5]. R.S. Mishra, M.W. Mahoney, ‘’Friction Stir Spot Welding, American Society for Metals,’’ 2007, pp. 235-250.
[6]. D. A. Wang and S. C. Lee, ‘’Microstructures and failure mechanisms of friction stir spot welds of aluminum 6061-T6 sheets,’’ J. Mater. Process. Technol., 2007, 186291-297.
[7]. M. K. Bilici and A. I. Yukler, ‘’Effects of welding parameters on friction stir spot welding of high density polyethylene sheets,’’ Mater. Des., 2012, 33, 545–550.
[8]. R. Sakano, K. Murakami, K.Yamashita, T. Hyoe, M. Fujimoto, M. Inuzuka, U. Nagao, H. Kashiki, “Development of spot FSW robot system for automobile body members,’’ Proceedings of the Third Int. Symposium of Friction Stir Welding,’’ Kobe, Japan, 2001.
[9]. T. Iwashita, Method and apparatus for joining, US Patent Issued on August 5, 2003.
[10]. R. Hancock, ‘’Friction stir spot welding on similar aluminum alloys al6082 by using different shape of en19 and en 31 profile tool,’’ Welding journal, 2004, 40-43.
[11]. "Mazda Develops World's First Aluminum Joining Technology Using Friction Heat", Mazda media release, February 27, 2003.
[12]. C. B. Fuller, in: R.S. Mishra, M.W. Mahoney (Eds.), Friction Stir Welding and Processing, ASM International, Ohio, 2007, pp. 7-35.
[13]. S. Aslanlar, ‘’The Effect of Nucleus Size on Mechanical Properties in Electrical Resistance Spot Welding of Sheets Used in Automotive Industry,’’ Materials and Design, 2006, 27, pp.125-131.
[14]. P. Gupta, P.K. Ghosh, S.K. Nath and S. Ray, “Resistance spot weldability of plain carbon and low alloy dual phase steels”, Z. Metallkde., 1990, 81,7, pp. 502-508.
[15]. P. Sharma, P.K. Ghosh and S.K. Nath, “Studies on fatigue behaviour of resistance spot welded Mn-Cr-Mo dual phase steel”, Z. Metallkunde, 1993, 84, 7, pp. 513-517.
[16]. M. Vural and A.Akkus, ‘’On the resistance spot weldability of galvanized interstitial free steel sheets with austenitic stainless steel sheets,’’ J. Mater. Process. Technol., 2004, 153-1.
[17]. M.Vural, A.Akkus and B. Eryurek, ‘’Analysis of Process Parameters for Resistance Spot Welding on Cold Reduced Low Carbon Steel,’’ J. Mater. Process. Technol., 2006, 176-127.
[18]. F. Hayat, B. Demir and M. Acarer, ‘’Tensile shear stress and microstructure of low-carbon dual-phase Mn-Ni steels after spot resistance welding,’’ Sci. Heat Treat., 2007, 49 484.
[19]. P. Zhang, J. Xie, Y.X.Wang and J.Q. Chen, ‘’Effects of welding parameters on mechanical properties and microstructure of resistance spot welded DP600 joints,’’ Sci. Technol. Weld. Join., 2011, 16-567.

[20]. Y. Tozaki, Y. Uematsu, K. Tokaji, ‘’Effect of Processing Parameters on Static Strength of Dissimilar Friction Stir Spot Welds Between Different Aluminium Alloys Fatigue,’’ Fract. Engng. Mater. Struct., 2007, 30 , pp.143-148.
[21]. B.R. Singh, A handbook on Friction stir welding Research Gate, DOI/10.13140/RG.2.1.5088.6244 (2012).
[22]. Z. Zhang, X. Yang, J. Zhang, G. Zhou, X. Xu, B. Zou, ‘’Effect of Welding Parameters on Microstructure and Mechanical Properties of Friction Stir Spot Welded 5052 Aluminum Alloy,‘’ Materials and Design, 2011, 32, pp.4461-4470.

Journal Homepage : http://dergipark.gov.tr/ejens
EJENS
European Journal of Engineering and Natural Sciences
CODEN: EJENS
DergiPark AKADEMİK

An Alternative Method for Long-Term Land Cover Change Detection: A Case Study of Hasanlar Dam

Firat Caglar Yilmaz[1]*, Sukran Sahin[2]

[1] *Pamukkale University, Department of Landscape Architecture, 20070, Pamukkale/Denizli, Turkey.*

[2] *Ankara University, Department of Landscape Architecture, 06120, Keçiören/Ankara, Turkey.*

**Corresponding Author email: fcyilmaz@pau.edu.tr*

Abstract

Dams which needed to drinking and irrigation water supply, flood control etc. at first have undertaken an another task with hydroelectric power which emerged from the increasing energy demand due to population growth, technological developments and changes in consumption habits in recent years. This process has accelerated from the 1980s which was the beginning of the increasing trends in renewable energy sources due to the environmental impacts of fossil fuels. However, even though dam type hydroelectric power plant project is a renewable energy, it has some adverse effects on ecosystems. The changing flow regime with the intervention to the river generally results in destruction and fragmentation in the riparian ecosystem. This change in the land cover can lead to modification on the microclimate, thus it can change the hydrological cycle of the basin. For this reason, the monitoring of the change in the land cover at the dam and its surroundings is important for revealing the effects of the project. In this context the Hasanlar Dam in Düzce province was examined in the scope of this study. The land cover change has been determined in two temporal periods through 1:25000 scale topographic maps date on 1960, 1982 and 2013. The land cover which is consist of 4 classes was obtained by visual classification method. The amount of change was determined as the unit by grid method. It was observed that forest areas showed a decreasing tendency after the dam construction during the first temporal period but an increase was shown later. On the other hand it has been determined that non-vegetated areas are transformed into orchard predominantly. As a result, it has been seen that the proposed method can provide an effective analysis for the land cover change detection when old dated aerial photos or satellite images can not be reached.

Key words

Land cover change, Dam, Hydroelectric power plant, Hasanlar Dam

1. INTRODUCTION

In our day, the development and conservation of water resources have become one of the most important parameters of their modernity beside influencing the development of countries [1]. In this context, the concept of sustainability comes to the forefront in the projects that countries implement for the utilization of water resources. Among these projects, dam projects have an important share.

It is seen that the first samples of dams were constructed for agricultural irrigation, drinking water supply and flood control. However, when it came out that the controlled water can be an energy source when released, the dams gained another function [2]. Although there are different methods that do not require a dam crest to obtain

energy from the river, this discovery of humans has played a role in the increase of dam projects. This method, called hydroelectric, which works by the principle of converting the potential energy of water flowing from the highs through the turbines and generators to electric energy, is preferable as it is a cleaner and renewable resource compared to fossil fuels [3], [4]. Such that; the report by The World Commission on Dams, published in 2000, shows the extent of intervention in streams in a rational sense. In the report, it is stated that in European Union countries and United States, 60-65% of rivers were controlled, although it differs by the basin, whereas in Asia, the number of rivers taken under control by more than one large-scale dam was well below half the total number of rivers [5].

Although the dam projects have an important place in development, they have some adverse effects on ecosystems. The results of studies in developed countries in the northern hemisphere show that river regulation is the most powerful and common anthropogenic impact on the riverine ecosystem [6]. These adverse effects can be seen in the short or long term and can be grouped as effects on aquatic ecosystems, fauna, and flora. Depending on the changing regime of flow; the changing habitat areas in the river due to the blocking of sediment transport [4], blocking of the transport of nutrients required for aquatic life [4], defects in some vital activities (determination of migration time etc.) of living beings due to the regime of flow [7], declining water quality resulting from eutrophication starting with transition to stagnant water [7] and changing bottom structure [8] are examples of the effects on aquatic ecosystems. In other words, the changing flow regime generally results in the destruction and fragmentation of the riverine ecosystem [9]. In terms of fauna, prevention of the passage of fish species moving between the lower and upper parts of the river seems to be an important impact value [8]. The adverse effects on the flora becomes visible in a much shorter period in the construction phase. For example; the dust created by the construction work sticks on leaves and decreases the light transmittance, thus, affects the photosynthesis and slows the growth rate of the plant [10]. In the long term, the evaporation increases together with the dam reservoir formed and therefore some climatic effects occur. The humidity in the air increases, the air movement change, and the temperature, wind, and precipitation become different. This creates a sudden change in the natural vegetation in the region, and only species that can adapt to this change can survive [7]. In the light of this information, it understood that the change in land cover is inevitable as a result of the intervention to nature through the dam projects. In fact, in the change of microclimate and land cover, there is a bi-directional setup that affects both. In other words, the change in land cover can lead to modification of the microclimate, thus, change the hydrological cycle of the basin [11]. As a result, changing land cover also affects other landscape functions. For example; the infiltration capacity of the area varies due to changing land cover, and it changes surface flow dynamics [12]. In this context, land cover change analysis can be an effective method in order to interpret long-term environmental effects of dam projects.

Nowadays, satellite images are mostly preferred as a data set in land cover change analysis. The most important reason for this preference is that the reflection values processed on the raster data can be classified by different methods in line with their closeness to each other. Since the archival images are free of charge and easy to reach, the images by Landsat satellites are frequently preferred, however, these records also do not cover the data of pre-1970s. This is the greatest constraint on the use of satellite images in long-term analyzes. For this reason, it is aimed to develop an alternative method that can be used in the analysis of land cover change, especially when there is no effective data such as the satellite image for past. In addition, the effects of the dam project and the findings obtained with this alternative method applied in Hasanlar Dam in Düzce province were interpreted.

2. MATERIAL AND METHOD

Hasanlar Dam and HEPP (Hydroelectric Power Plant) located in Düzce province were determined as study area (Figure 1). The construction of the dam on the Küçük Melen stream, located between the Düzce and Yığılca districts, was started in 1965 [13]. The maximum water level of the dam is 271.30 m. and the crest elevation is 70.80 m. [14].

Materials used within the scope of this study are:

- Topographic maps numbered G26b1 of 1960, 1982 and 2013, provided in raster format by General Command of Mapping,
- ArcGIS 10.2, a GIS (Geographical Information System) based software used for digitizing topographic maps, storing and mapping all data, and analyzing,
- Literature review regarding the field of study and the subject,
- Interviews with officials and local people made during the area survey.

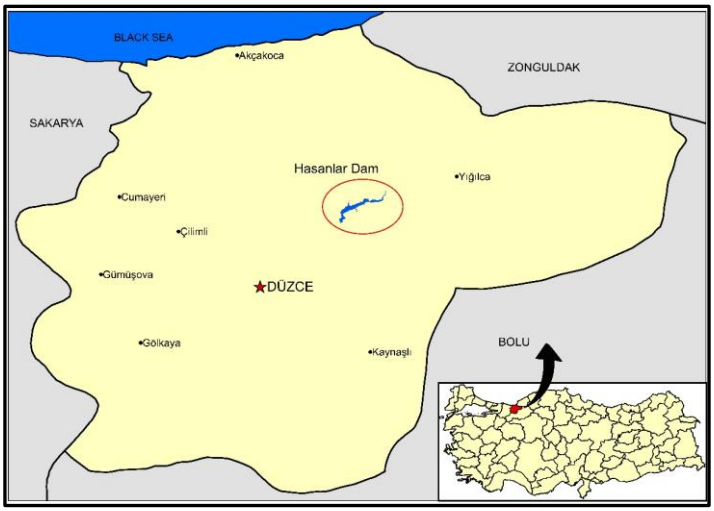

Figure 1. The location of study area

During the literature review, the largest damages and land cover changes by the dam projects were found out to be in the riverine ecosystem. For this reason, when determining the boundaries of the study area, it was meant to determine the ecological border closest to the shore line. In this context, the "direct drainage area" defined by Zielenski (2002) [15] was accepted as the boundary. The direct drainage area defines areas that are wedge-shaped on both sides of the main stream following the determination of the basin boundaries of the side streams, which has more than two branches, connected to the main stream, and which do not belong to any sub-basin boundary. These areas are not included in the sub-basin boundaries as they consist of the aspects which directly faced to the main stream. In other words, the surface flow in these areas is directed to the main stream. Zielenski argues that these areas have a sub-basin character when evaluated together. The boundaries of the study area are shown in Figure 2 starting from this point of view.

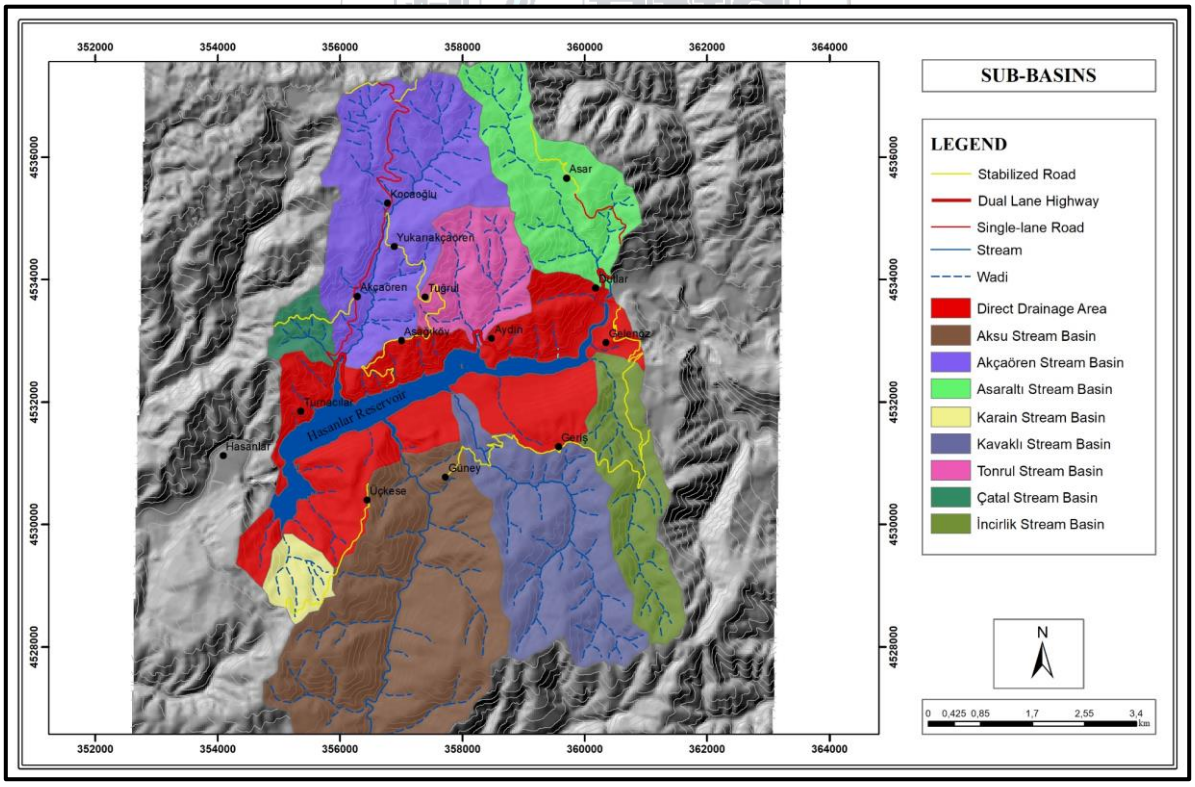

Figure 2. Direct drainage area for Hasanlar reservoir

In the mapping of the land cover for the relevant years, four classes were used in the study due to the limited information contained in the 1:25000 scale topographic maps. These are; forest, orchard, water surface, and non-vegetated area. In order to be able to perform the change analysis, the vector data required were obtained by

manual on-screen digitization of the topographical maps. However, in this method, the digitization is followed by a grid method in order to eliminate the user-related differences. In this context, the area was divided into 250x250 m. flags (each square= 6.25 ha) and a land cover class was assigned for each square (Figure 3). Thus, the size of the change was not area-based but unit-based. The determination of the land cover is considered as a process consisting of two stages. In the first stage; it is aimed to determine whether the relevant square belongs only to aquatic or terrestrial ecosystems. For this purpose, the class which was bigger was assigned. Thus, the grids forming the surface of the water were identified and the only thing left was the reclassification of the terrestrial ecosystem, which contains the forests, orchards, and non-vegetated areas classes. In the second stage, this process was carried out by applying the same method. Since there were two classes in the first stage, the area that holds 50% of the overall size was looked for to make the assignment, whereas, in the second stage there were three classes, therefore the area with the largest size was assigned directly.

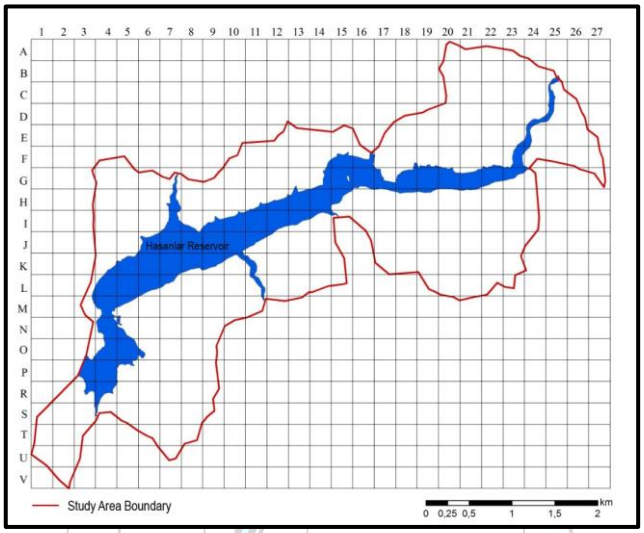

Figure 3. Applying grid method to the study area

An analysis of change in land cover was periodically examined as a 53-year process between 1960-1982 and 1982-2013, then between 1960 and 2013, which would most commonly reflect the change.

3. RESULTS

The area size distributions of the land cover structure for the related years, which were formed by applying the method, are shown in Table 1. There are only two classes that consist of forest and non-vegetated area in the 1960 land cover, which is a date before the start of the dam construction. In the 1982 land cover, even though it has a very small percentage with 2% the orchards have been seen and so four classes have presence at the area. It appears that four classes retain their existence in 2013 which is the latest land cover. On the other hand, the spatial distributions of the land cover classes are shown in Figure 4 which contains the maps by the years.

Table 1. The area size distributions of the land cover classes by the years

Land Cover Based On the Years (Unit/Percentage)	**Forest**	**Orchard**	**Non-vegetated Area**	**Water Surface**
1960	159 / 59%	-	111 / 41%	-
1982	122 / 45%	6 / 2%	101 / 38%	41 / 15%
2013	140 / 52%	67 /25%	22 / 8%	41 / 15%

3.1. Land Cover Change Analysis in 1960-1982 Period

It can be seen from the matrix in the Table 2 that the reservoir observed with 41 units was formed in the year 1982 by transforming 37 units from the non-vegetated area and 4 units from the forest. Forest areas lost 37 units, despite gaining 9 units from the non-vegetated area. The losing of 28 units on the forest class is remarkable. In addition, the orchards started to be seen at the area with a small area size like 6 units by transforming 5 units from the forest and 1 unit from the non-vegetated area at the end of this temporal period. The spatial distributions of the changes in the period are shown in Figure 5.

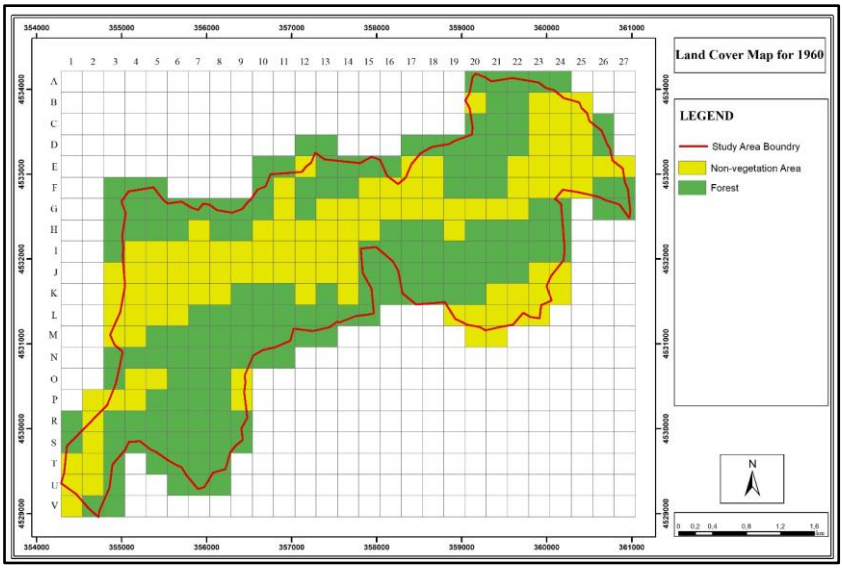

(a)

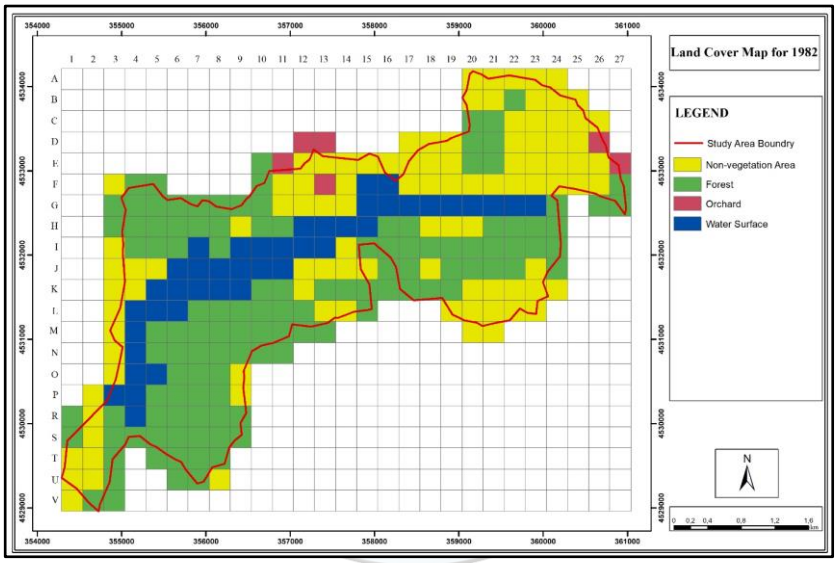

(b)

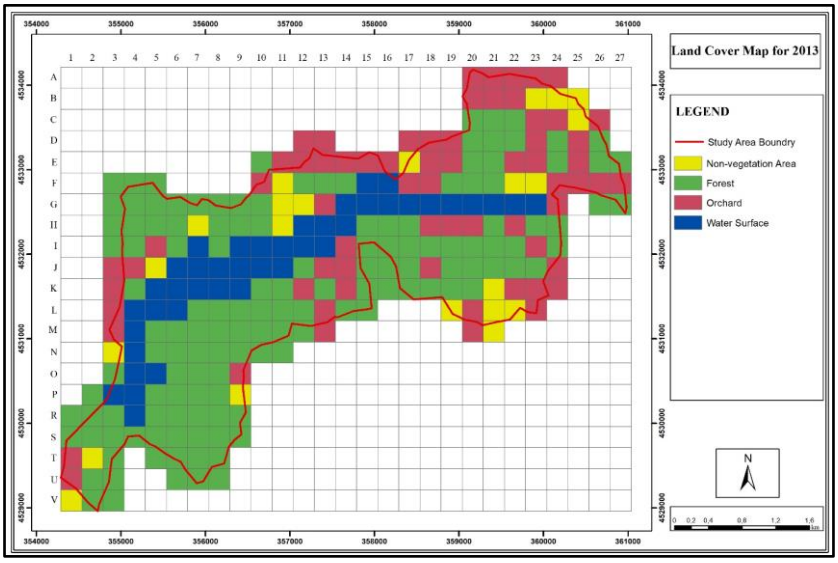

(c)

Figure 4. Land cover maps by the years a)1960, b)1982, c)2013

Table 2. The area size change of the land cover classes in 1960-1982 period

Changes in 1960-1982 (by Units)	**Forest**	**Orchard**	**Non-vegetated Area**	**Water Surface**	**The situation of 1960**
Forest	113	5	37	4	159
Orchard	-	-	-	-	-
Non-vegetated Area	9	1	64	37	111
Water Surface	-	-	-	-	-
The situation of 1982	122	6	101	41	**Total**:270

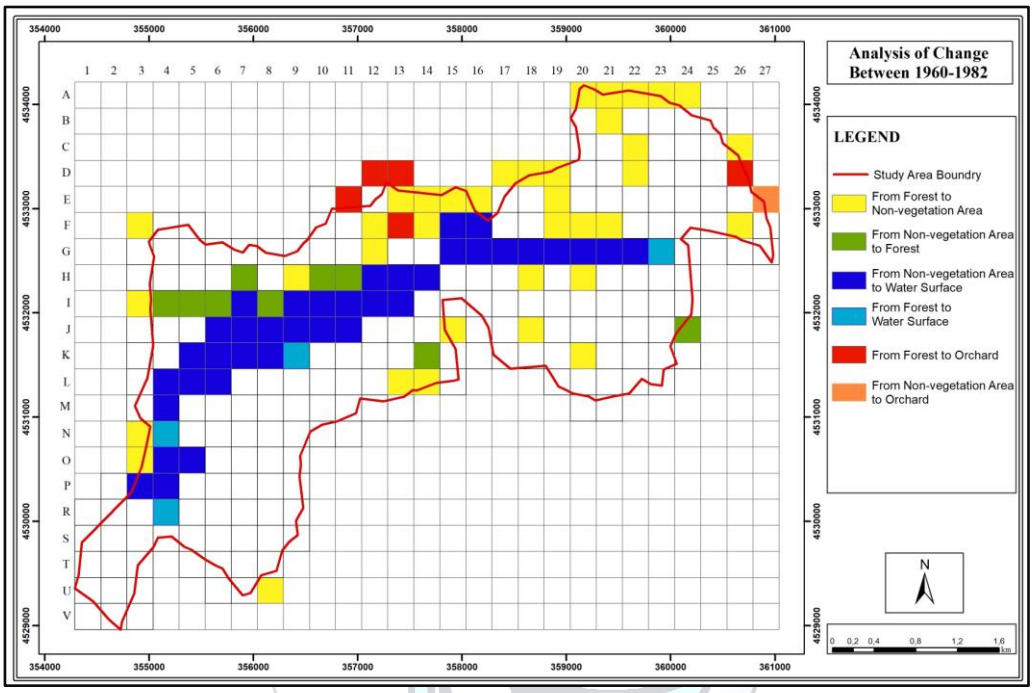

Figure 5. The units which show a change in 1960-1982 period

3.2. Land Cover Change Analysis in 1982-2013 Period

It has been determined that the non-vegetated areas rapidly transformed into forest and orchard areas in this temporal period. Only 22 units of non-vegetated area has been left by 2013. Besides the orchards reached 67 units by gaining 54 units from non-vegetated areas (Table 3). The spatial distributions of the changes in the period are shown in Figure 6.

Table 3. The area size change of the land cover classes in 1982-2013 period

Changes in 1982-2013 (by Units)	**Forest**	**Orchard**	**Non-vegetated Area**	**Water Surface**	**The situation of 1982**
Forest	110	10	2	-	122
Orchard	3	3	-	-	6
Non-vegetated Area	27	54	20	-	101
Water Surface	-	-	-	41	41
The situation of 2013	140	67	22	41	**Total**:270

3.3. Land Cover Change Analysis in 1960-2013 Period

This is the longest period analyzed in the frame of data at the study. Therefore, analyzing the period demonstrates the most general change between the land cover classes. It is almost impossible not to focus on non-vegetated areas in this analysis. 37 units of this class have been submerged, 37 units have turned into orchard and 17 units have gained forestry qualities (Table 4). The spatial distributions of the changes in the period are shown in Figure 7.

Table 4. The area size change of the land cover classes in 1960-2013 period

Changes in 1960-2013 (by Units)	**Forest**	**Orchard**	**Non-vegetated Area**	**Water Surface**	**The situation of 1960**
Forest	123	30	2	4	159
Orchard	-	-	-	-	-
Non-vegetated Area	17	37	20	37	111
Water Surface	-	-	-	-	-
The situation of 2013	140	67	22	41	**Total**:270

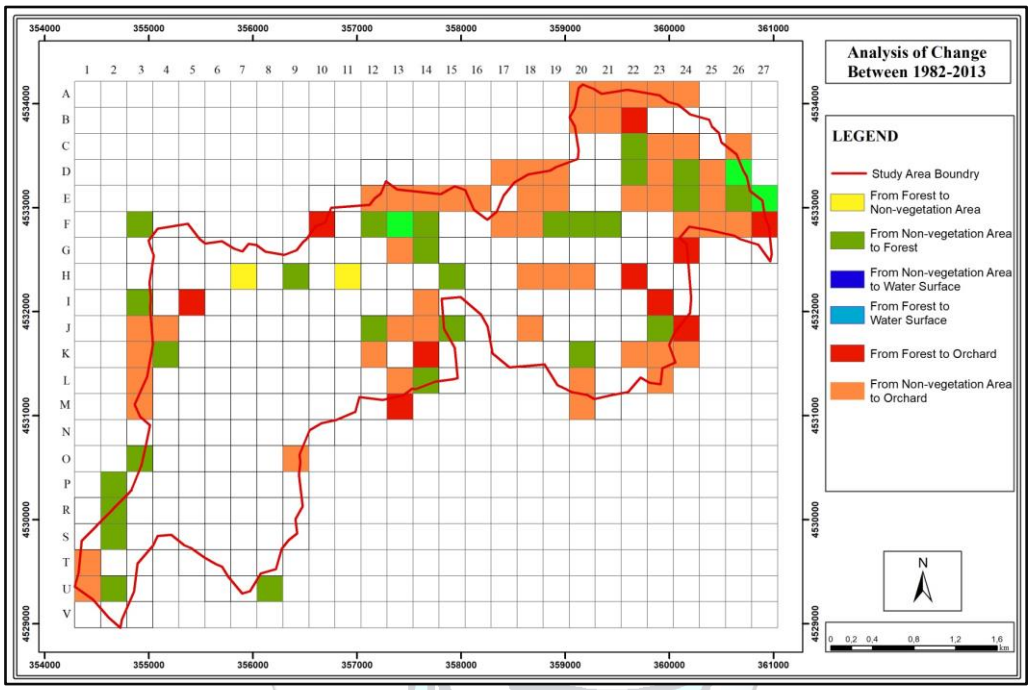

Figure 6. The units which show a change in 1982-2013 period

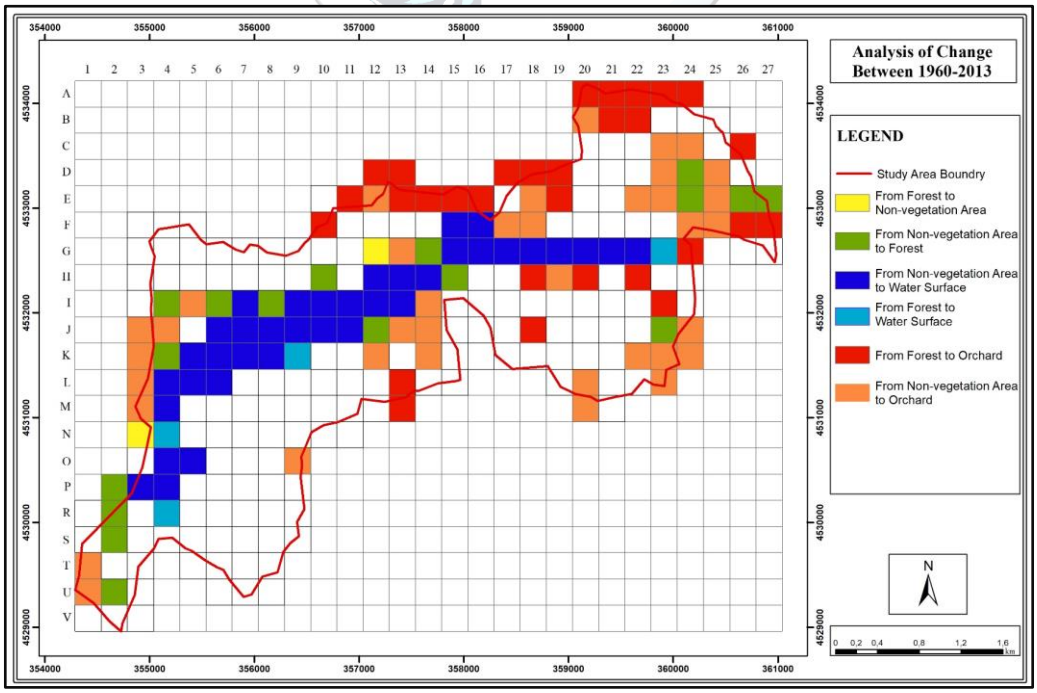

Figure 7. The units which show a change in 1960-2013 period

4. DISCUSSION AND CONCLUSION

Although it has some weaknesses, the method that been proposed in this study has an efficient use in order to monitor the temporal land cover change in general terms. As the study area expands, this efficiency increases. The method is likely to provide a good alternative when old dated aerial photos or satellite images can not be reached. The weaknesses of the method can be summarized as follows:

- Enable to create a limited number of classes
- Having low sensivity with regards to the size of changing areas

On the other hand, assessment of the environmental impacts of the Hasanlar Dam by interpreting the results is another output of the study. Interpretations in this context are as follows:

- The changes in the forest and non-vegetated area indicate the modification of microclimate in the study area with the reservoir.
- Increasing rapidly orchard areas which were not found before the dam construction, is an indirect anthropogenic effect of the dam project. Because, the changing climate conditions have become suitable for orchards and transportation to irrigation water has become easier.

ACKNOWLEDGMENT

This study is a part of master thesis of the corresponding author.

REFERENCES

[1]. Öztürk, T., "Çoruh havzası su kaynaklarını geliştirme projelerinin çevresel etkileri," TMMOB Su Politikaları Kongresi, 2009, s. 220-226.
[2]. Baxter R.M., "Environmental effects of dams and impoundments," Annual Review Ecological Systems, vol. 8, pp. 255-283, 1977.
[3]. Kocabaş, M., Başçınar, N., Kutluyer, F., Önder, A.,"HES'ler ve balıklar," Türk Bilimsel Derlemeler Dergisi, 6(1), s.128-131, 2013.
[4]. Yurtseven, İ., "Nehir Tipi Hidroelektrik santrallerin havzalar üzerindeki ekohidrolojik etkileri," Journal of the Faculty of Forestry, Istanbul University, 61(1), s. 55-62, 2011.
[5]. "Dams and devolopment: A new framework for decision-making," The Report of the World Commission on Dams, London, Uk, Earthscan Publications, 2000.
[6]. Dynesius, M. and Nilsson C., "Fragmentation and flow regulation of river systems in the northern third of the world," Science, vol. 266, pp. 753-762, Nov. 1994.
[7]. Berkün, M., Aras, E. and Koç, T., "Barajların ve hidroelektrik santrallerin nehir ekolojisi üzerinde oluşturduğu etkiler," TMH- Türkiye Mühendislik Haberleri, 6(452), pp. 41-48, 2008.
[8]. Aksungur, M., Ak, O., Özdemir, A., "Nehir tipi hidroelektrik santrallerin sucul ekosisteme etkisi: Trabzon örneği," Journal of Fisheries Sciences, 5(1), pp. 79-92, 2011.
[9]. Lovett, R.A., "As salmon stage disappearing act, dams may too," Science, vol. 284, pp. 574-575, April 1999.
[10]. "10 Soruda Hidroelektrik Santraller," WWF Türkiye Yayını, 2013.
[11]. Obahoundje, S., Ofosu, E.A., Akpoti, K. and Kabo-bah, A.T., "Land use and land cover changes under climate uncertainty: modelling the impacts on hydropower production in Western Africa," Hydrology, 4(2), 2017.
[12]. Bewket, W. and Sterk, G., "Dynamics in land cover and its effect on stream flow in the Chemoga watershed, Blue Nile basin, Ethiopia," Hydrological Processes, vol. 19, pp. 445-458, 2005.
[13]. DSİ website. [Online]. Available: http://www2.dsi.gov.tr/baraj/detay.cfm?BarajID=43
[14]. Hasanlar HES Proje Tanıtım Dosyası, Ankara.
[15]. Zielinski, J., "Watershed Vulnerability Analysis," Center for Watershed Protection Tech. Rep., 2002.

Journal Homepage : http://dergipark.gov.tr/ejens
EJENS
European Journal of Engineering and Natural Sciences
CODEN: EJENS
DergiPark AKADEMİK

Determination of Turbidity in Filyos Stream Water by Artificial Neural Network

Berna Aksoy[1]*, İsmail Hakkı Özölçer[1], Emrah Doğan[2], Onur Dündar[1]
[1]*Zongyldak Bulent Ecevit University, Department of Civil Engineering, 67100, Zonguldak, Turkey.*
[2] *Sakarya University, Department of Civil Engineering, 54100, Sakarya, Turkey.*
**Corresponding Author email: berna.oaksoy@beun.edu.tr, brnaksoy@hotmail.com*

Abstract

Water is in an endless cycle, which is source of life for human beings. During this cycle, substances that are contaminated in water cause physical, chemical or biological alteration of the water's natural features, that leads to water pollution and therefore causes the environmental balance to deteriorate over time. This quality changes cause deteriorations in ecosystem. For this reason, it is important to investigate the water quality in rivers and water reservoirs which are close to settlement areas. In this study, surface water quality measurements were carried out at downstream of the Filyos stream, which forms the largest sub-basin in the Western Karadeniz Basin, at intervals of thirty days in one year period between September 2015 and August 2016. In the scope of the study, zinc, chromium, calcium, aluminium, manganese and turbidity parameters measured in the laboratory and estimation of the turbidity parameter basaed on parameters of zinc, chromium, calcium, aluminium, manganese was performed by artificial neural networks

Key words

Filyos Stream, Heavy Metal, Turbidity, Artificial Neural Networks, Western Blacksea Basin

1. INTRODUCTION

Rivers and streams are used in many parts of the world for drinking water, agricultural irrigation and industrial purposes. Today, rapidly growing population, developing infrastructural deficiencies resulting from the expansion of industrial and residential areas and the inadequacy of treatment plants cause pollution of rivers and freshwater resources. The increasing rate of pollution destroys the balance of nature and reaches the dimensions that threaten human life.

Water quality changes cause the animal and plant species that exist in nature to change, thus causing the ecosystem to change. Therefore, investigations of water quality in rivers and water reservoirs close to their habitat are important.

Make observations and measurements over the river, prodives information to researchers and planner. When these researches are planned on a basin basis, sustainable management of water resources has considerable precaution.

A better understanding of the hydrodynamic properties of reservoirs has also gained momentum with advances in computer technology in recent years. Measurements in water quality models, such as mathematical and artificial neural network, can also be analyzed with methods. In this study, artificial neural networks were used and data obtained from water quality studies were estimated in this method.

In this study, surface water quality measurements were made at the observation station selected at the Filyos Stream (228 km), the largest sub-basin of the Western Black Sea Basin, at intervals of thirty days in one year period. Water quality parameters (turbidity, calcium, aluminium, manganese, chromium and zinc) measured and analysis were performed in the laboratory according to standart methods, After, estimation of the turbidity parameter based on parameters of calcium, aluminium, manganese, chromium and zinc was performed by artificial neural networks.

Figure 1. Subbasin of Western Blacksea Basin (URL-6)

2. MATERIALS AND METHODS

Surface water quality measurements were carried out at downstream of the Filyos stream, which forms the largest sub-basin in the western Karadeniz Basin, at intervals of thirty days (September 2015- August 2016) in one year period. (Figure 2).

Figure 2. Filyos downstream satellite image (Google Earth, 2017)

The collection, storage and delivery of water samples in accordance with standard methods has been carried out. During sampling, the sample containers of the water samples to be taken were rinsed with water, filled with no gaps and tightly closed. +4 °C prodected samples brought to the laboratory in six hours. Turbidity and ion analysis were performed in the laboratory according to the standart methods. Nexion 300D model ICP-MS was used in the analysis.

Figure 3. Nexion 300D model ICP-MS

An artificial neural network (AAN) model was prepaered for the samples which taken from downstream to estimate the turbidity according to month. MATLAB-based artifical neural network (ANN) toolbox was used for model analysis. AAN topology analysis was performed to determine the number of AAN hidden layer neurons in

the preparation phase. AAN performances for different hidden layer neuron numbers, R^2 (Determination coefficient) and MSE (Mean Squared Error) statistical performance analysis criteria were used. The hidden layer neuron counts were taken as 3, 4, 6, 8 and 10, respectively, and the AAN topologies were trained and tested.

The AAN analysis method used for estimating the turbidity parameter in the water is the multi-layered sensor (MDA) model; input layer, intermediate layers and output layer. In the models, Ca^{+2} Al^{+3} Mn^{+2} Cr^{+3} Zn^{+2} parameters are input and turbidity is used as output parameter.

3. RESULTS AND DISCUSSION

The results of the parameters analyzed in the laboratory according to standard methods are given in Table 1.

Table 1.Laboratory Analysis Results

Months	Turbidity	Ca^{+2}	Al^{+3}	Mn^{+2}	Cr^{+3}	Zn^{+2}
1	98.6	52.31	7.65	0.217	0.087	0.246
2	86.4	50.68	10.96	0.147	0.135	0.547
3	95.6	51.64	12.8	0.351	0.426	0.372
4	78.4	52.31	17.5	0.438	0.258	0.254
5	68.3	54.86	25.4	0.372	0.324	0.212
6	69.1	55.16	15.24	0.371	0.355	0.127
7	46.7	55.13	4.327	0.326	0.132	0.59
8	28.12	55.23	4.641	0.108	0.033	0.658
9	63.25	55.25	2.142	0.642	0.284	0.392
10	35.72	55.31	5.526	0.02	0.114	0.587
11	17.09	53.48	4.434	0.093	0.05	0.286
12	64.12	51.68	8.61	0.154	0.074	0.097

According to the obtained analysis results, the models in Table 2 for different input layers in AAN have been established. Weights, number of hidden layers and number of nodes were found by trial and error to obtain the most appropriate result between 1 input and 1 output while the model was being created.

Table 2. Models created for different input layers

Model No	Input Layer Variables	Output Layer
1	Ca^{+2}	Turbidity
2	Al^{+3}	Turbidity
3	Mn^{+2}	Turbidity
4	Cr^{+3}	Turbidity
5	Zn^{+2}	Turbidity

In this study, each parameter was tried as an input data value, and the turbidity as the output value was estimated.. The data were normalized between 0-1 before being given to the network. Accordingly, the YSA results will remain between 0-1. The model results are shown in tables for each parameter separately and the topologies with the best performance is charted.

Table 3. Zn^{+2} topology analysis for parameter

Model No	Number of Hidden Layer Neurons	R^2	MSE
1	3	0.9667	0.0021
2	4	0.9264	0.0047
3	6	0.9900	0.0006431
4	8	0.9030	0.0062
5	10	0.9821	0.0008031

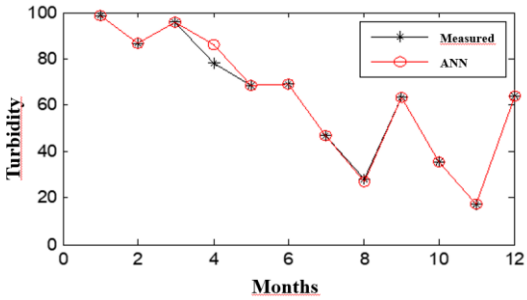

Figure 4. Zn^{+2} *parameter AAN performance*

Table 4. Cr^{+3} *topology analysis for parameter*

Model No	Number of Hidden Layer Neurons	R^2	MSE
1	3	0.9409	0.0038
2	4	0.9115	0.0057
3	6	0.9643	0.0023
4	8	0.9759	0.0016
5	10	0.9874	0.0008133

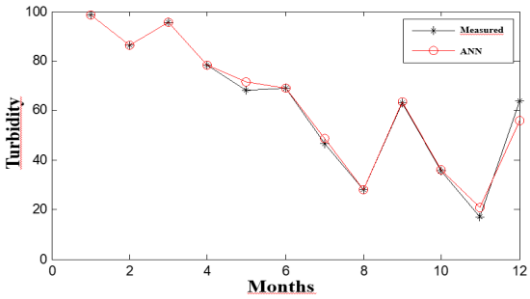

Figure 5. Cr^{+3} *parameter AAN performance*

Table 5. Ca^{+2} *topology analysis for parameter*

Model No	Number of Hidden Layer Neurons	R^2	MSE
1	3	0.9563	0.0028
2	4	0.8747	0.0081
3	6	0.9776	0.0021
4	8	0.9231	0.0052
5	10	0.9570	0.0028

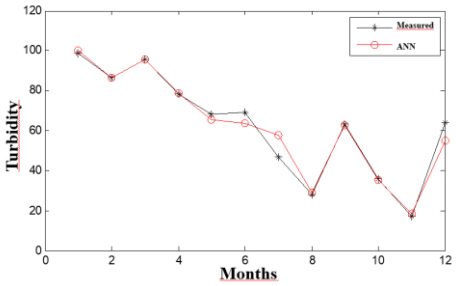

Figure 6. Ca^{+2} *parameter AAN performance*

Table 6. Al^{+3} topology analysis for parameter

Model No	Number of Hidden Layer Neurons	R^2	MSE
1	3	0.9426	0.0037
2	4	0.8761	0.0080
3	6	0.9722	0.0018
4	8	0.9473	0.0034
5	10	0.9608	0.0025

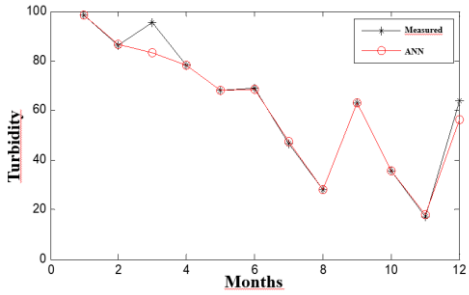

Figure 7. Al^{+3} parameter AAN performance

Table 7. Mn^{+2} topology analysis for parameter

Model No	Number of Hidden Layer Neurons	R^2	MSE
1	3	0.9642	0.0061
2	4	0.9198	0.0052
3	6	0.8762	0.0080
4	8	0.9642	0.0023
5	10	0.9335	0.0043

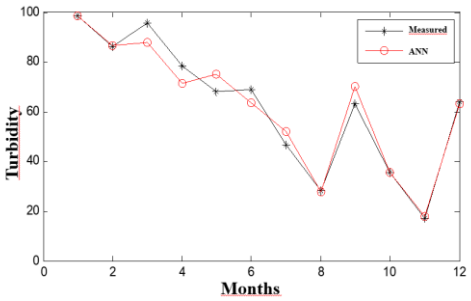

Figure 8. Mn^{+2} parameter AAN performance

4. CONCLUSIONS

Clarity is a magnitude that determines the natural structure of water Organic and inorganic materials etc. causes turbidity in the waterThe strength of the sulfur contaminant causes water turbidity. For this reason, the turbidity level of surface waters is measured as the degree of pollution. The measurement of the turbidity parameter in the surface water can be used to follow the pollution test in the water and the natural cleansing of the river. For this reason, the studies in which the pollution dimension is searched are the investigations that should be done routinely.

However, since turbidity depends on many parameters changing over time, it is difficult to be formulated For this reason, artificial neural networks come into play here. In this study, considering the ions affecting the turbidity,

AAN models were established and the parameters giving the best test performance were determined. As a result of the analyzes made, it has been observed that the Zn parameter has the best test performance. This is followed by the parameters Cr, Ca, Al, Mn, respectively. As it is clear from the graphs, it is determined that there are not very big differences between the results obtained from AAN and the measured values. It has been demonstrated that YSA can be successfully implemented and produces safe estimates.

REFERENCES

[1].APHA Standart Methods for the Examination of Water and Waste Water, 20th Ed., APHA, AWWA, WEF, Washington , D. C., 1998.
[2].Ay M, Su Kalitesi Parametrelerinin Yapay Zeka Yöntemleri İle Değerlendirilmesi, Doktora Tezi, Erciyes Üniversitesi, Fen Bilimleri Enstitüsü, İnşaat Mühendisliği Anabilim Dalı, Kayseri, 117, 2014.
[3].Bayram A, Harşit Çayı Su Kalitesinin Mevsimsel Değişiminin İncelenmesi Ve Askı Madde Konsantrasyonunun Yapay Sinir Ağları Yöntemi İle Tahmin Edilmesi, Doktora, Karadeniz Teknik Üniversitesi, Fen Bilimleri Enstitüsü, İnşaat Mühendisliği Anabilim Dalı, Trabzon, 163, 2011.
[4].Bayram A ve Kenanoğlu M, Temporal Variation of Total Nitrogen and Total Phosphorus in Surface Waters from the Lower Çoruh River Basin, Turkey, 3rd International Conference on Computational and Experimental Science and Engineering, 19-24 Ekim 2016, Antalya, Türkiye, 132(3): 712-716, 2017.
[5].Doğan E, Şengörür B ve Köklü R, Modeling Biological Oxygen Demand of the Melen River in Turkey Using An Artificial Neural Network Technique, Journal of Environmental Management, 90, (2): 1229-1235, 2009.
[6].İçağa Y, Bostanoğlu Y ve Kahraman E, Akarçay Havzası Su Kalitesi İstatistikleri. Yapı Teknolojileri Elektronik Dergisi, 2(1): 43-50, 2006.
[7].Kajiya T, Schellenberger F, Papadopulos P, Vollmer D and Butt H J, 3D Imaging of Water-Drop Condensation on Hydrophobic and Hydrophilic Lubricant-Impregnated Surfaces. Nature, 6: 1-10, 2016.
[8].Minarecioğlu N, Doğal Akarsularda Taşınan Katı Madde Miktarının Yapay Zeka Yöntemleri Kullanılarak Tahmin Edilmesi, Yüksek Lisans, Erciyes Üniversitesi, Fen Bilimleri, İnşaat Mühendisliği Anabilim Dalı, Kayseri, 68, 2008.
[9].Öztemel E, Yapay Sinir Ağları, 3. Baskı, ISBN: 9756797396, Papatya Bilim, İstanbul, 232,2016.
[10]. Sönmez A Y, Hisar O ve Yanık T, Karasu Irmağında Ağır Metal Kirliliğinin Tespiti ve Su Kalitesine Göre Sınıflandırılması. Atatürk Üniversitesi Ziraat Fakültesi Dergisi, 43(1): 69-77, 2012.

Journal Homepage : http://dergipark.gov.tr/ejens
EJENS
European Journal of Engineering and Natural Sciences
CODEN: EJENS
DergiPark AKADEMİK

Determination of The Hip Stem Loosening Using Vibration Method

Talip Celik[1]*, Yasin Kisioglu[1]
[1]*Kocaeli University, Department of Biomedical Engineering, 41380, İzmit/Kocaeli, Turkey.*
**Corresponding Author email: talip.celik@kocaeli.edu.tr*

Abstract

Aseptic loosening is a common problem in total hip replacement surgery. Routine radiological imaging techniques are used for postoperative diagnosis. The alternative technique is required to develop because of the low success rate in current diagnostic techniques. The purpose of this study is to develop the new method to diagnose the aseptic loosening of the stem using vibration technique. Two different experimental setups were established in this study, vibrational and cyclic loading tests. In the vibrational test, the bone-prosthetic models were vibrated from the distal femur at a certain frequency and then the vibration data were taken via accelerometer from the trochanter region of the femur. The vibration data were converted to the frequency domain for evaluations. The stability of the femur-prosthesis system was determined by evaluating the fundamental frequency change and harmonics generated at the FFT analysis. In the cyclic loading test, the femur-prosthesis system was forced to fatigue at a maximum amplitude of 1700 N and 1 Hz frequency. After every 5000 cycles in the test, the femoral prosthesis system was connected to the vibrational test and the loosening of the system was considered. After 115000 cycles, the harmonic frequencies were observed and the amplitude value of the fundamental frequency was decreased. The experiments were stopped when the stem was pulled out easily from the femur. As the degree of the loosening increased, the number of the harmonics increased and the fundamental frequency values decreased. In conclusion, the vibration method can be used as an alternative technique to determine the degree of the hip stem loosening.

Key words

Aseptic loosening, Total Hip Prosthesis, Vibration Technique, Cyclic Loading

1. INTRODUCTION

Orthopedic prostheses are frequently used for treatment in orthopedic surgery. The most common problem in the prostheses is aseptic loosening especially in hip prosthesis [1]. Because of this problem the prostheses dislocate and become unfunction. Hence, the revision surgery which is more difficult and costly is required.

An average of more than 1.2 million Total hip prosthesis (THP) surgeries are performed around the world and %10 of these surgeries are revised with the reason of the aseptic loosening [2]. The number of THP surgeries may estimate to increase with the long life expectancy through the developing technology and treatment opportunities. The radiology imaging methods are used for the detection of the loosening and the success of this method is very low [3].

In this study, the vibration method was evaluated to detect the loosening degree of THP. Two different test techniques have been established, the vibration and cyclic loading tests. The bone-prosthetic models were vibrated at a certain frequency and amplitude then the response of the bone-prosthetic system was evaluated in vibration test. In the cyclic loading test, the femoral prosthesis model was forced to be fatigue by cyclic loading. The harmonic frequency and amplitude changes were evaluated the loosening degree of the bone-prosthesis system.

2. MATERIALS AND METHODS

Fourth generation composite sawbone femur model (Sawbone Europe AB, Malmö, Sweden) and the pelvis model (Keklikoglu plastic Industry, Kayseri, Turkey) was used. Cementless Echelon stem and cup (stem length 160 mm, cup diameter 50 mm) was implanted in the femur and pelvis models. A metal stem head with a diameter of 26 mm was used together corresponding polyethylene inlay.

2.1. Vibration Test Method

The femur-stem-pelvis models were placed onto a test apparatus as seen in Figure 1. The pelvis model was fixated at three locations onto the sigma-profile. Rubber dampers were placed between the junctions of the test components. Four tension springs were used to stabilize the femur and pelvis joint. Two upper springs were simulated the gluteus medius muscle and two below springs were simulated the adductors magnus and longus (Figure 1). The springs were attached with the cords.

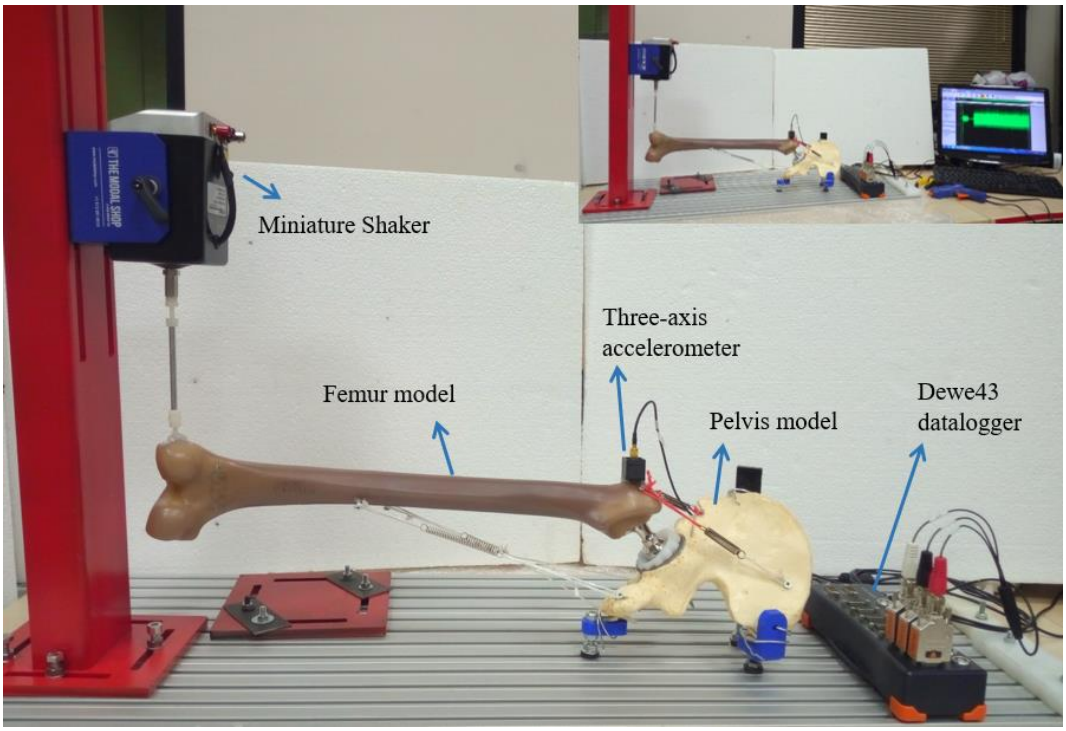

Figure 1. Vibration test setup

The femur-pelvis system were vibrated at the 200 and 250 Hz frequency via miniature shaker (The Modal Shop, Cincinnati, OH, USA) at the distal femur. Three-axis accelerometer (Measurement Specialties, Marmatek, Turkey) was placed at the greater trochanter of the femur. The vibration data were collected for ten seconds using DEWE43 datalogger (Dewesoft, Kumberg, Austria). 10 kHz low pass and 10 Hz high pass filters were used to prevent the noise. It was also used 50 Hz block filter to prevent the electric network noise. The vibration data were evaluated by performing Fast Fourier Transform (FFT) analysis. The occurrence of the harmonic frequency in the vibration data received from the system is an indication of the deterioration of the system integrity. In addition, the changing of the amplitude of the vibration data were evaluated in stabilized and unstable systems.

2.2. Cyclic Loading Test Method

In cyclic loading test, the femoral prosthesis model was forced to be fatigue by cyclic loading in universal test machine as seen Fig. 2. Distal femur was fixed with the clamps. The cyclic loads between 100 N and 1700 N in 1 Hz were applied on the stem head. The purpose of the cyclic loading is to damage the contact between the femur model and stem by simulating the real condition. Thus, the degree of the loosening and the deterioration of the connection between the femur and the stem can have been determined.

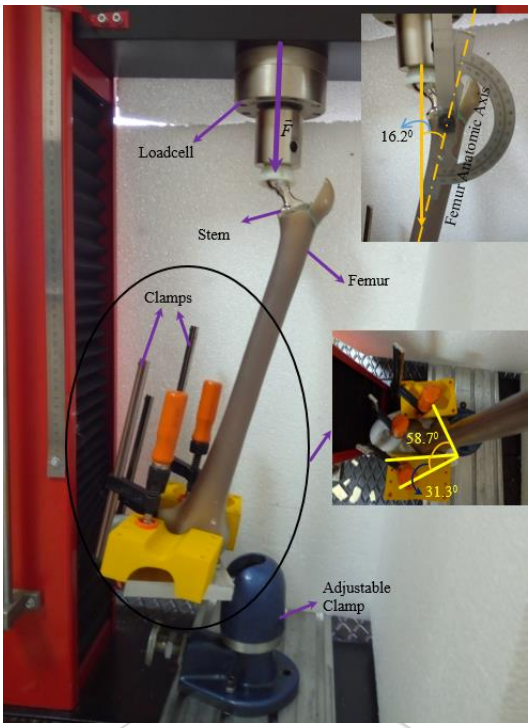

Figure 2. Cyclic loading test

3. RESULTS AND DISCUSSION

The stable femur-stem system was vibrated at 200 and 250 Hz to determine the stable system data. These data were the reference data to examine the loosening situations. The system was then applied the cyclic test to loosen the system. In 115000 loading cycle, the vibration data changed. The harmonic frequencies were observed and the amplitude of the main frequency was decreased. After each loading tests were applied in 5000 cycle loading, the vibration tests were executed. The stem completely loosened in the 125000 loading cycle. The graphs of stable and unstable systems were given in Fig. 3 and 4. The unstable system has three harmonic frequencies. Also, the amplitude of the main frequency in unstable system decreased with respect to the stable system.

The differences between the graphs provide important information about the system stability. The number of the harmonic frequencies indicate the contact status between the femur and stem. As long as the integrity of the system was distorted, the number of harmonics increased. The magnitude of the main frequency in the unstable system was lower in the stable one. Hence, this change in the magnitude of the main frequency is the indication of the system stability. The results of the stable and unstable systems were given in Table 1. The scoring system can be improved by these results and the stability of the system can be shown on the numerical value.

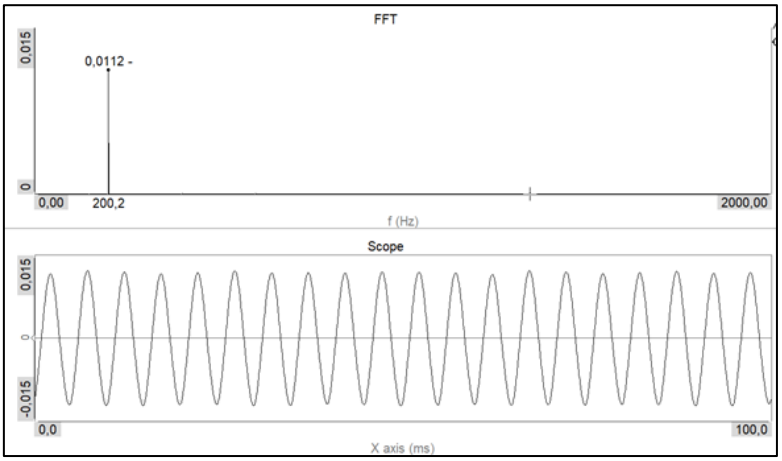

Figure 3. The amplitude-time graph and its FFT form in stable femur-stem system vibrating in 200 Hz frequency

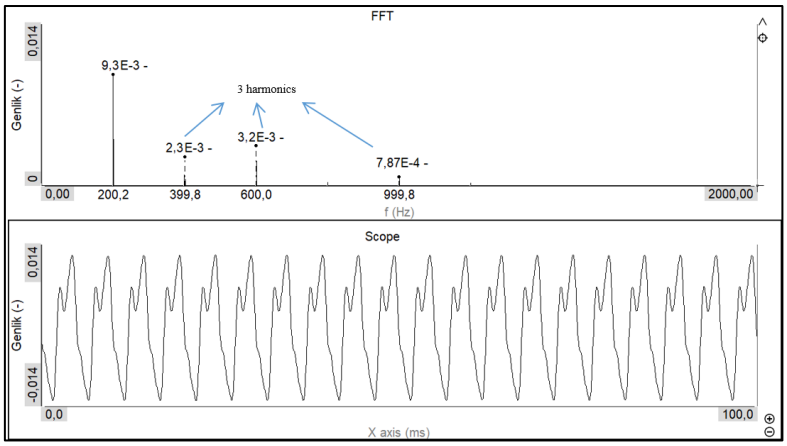

Figure 4. The amplitude-time graph and its FFT form in loosened femur-stem system vibrating in 200 Hz frequency

Table 1. The results of the stable and loosened femur-stem systems

	The magnitude of the main frequency (10^{-3})		**The number of the harmonic frequency**	
The number of the cyclic loading	200 Hz	250 Hz	200 Hz	250 Hz
Stable system	11.2	7.35	-	-
115000	11	7.25	1	2
120000	10	6.86	2	2
125000	9.3	6.39	3	3

Aseptic loosening of the hip stem is a major problem. The studies about the THP loosening were studied that the system is loose or stable [3-5]. In this study, the degree of the loosening was evaluated and it was shown the scoring system could be developed. Thus, the vibration method can be used as an alternative method in post-operative patient follow-up and the state of hip prosthesis stability can be determined.

The vibration method has been emphasized to be reliable and minimally invasive in many studies [3-6]. For this reason, it is a method that can be developed as an alternative to the currently used radiological imaging method with the low-success rate in determining aseptic loosening.

Rieger et al. [5] used the methods of counting peak amplitudes together with resonance frequency analysis to determine prosthesis stability. This method provides information about whether the system is loose or stable, but post-operative patient follow-up cannot be performed. Because the resonance frequency also depends on the mechanical properties of the parts that constitutive the system. Postoperative mechanical properties of human bone may change with reference to preoperative bone properties.

4. CONCLUSIONS

In conclusion, the vibration method can be used as an alternative method for determining the aseptic loosening of the hip prosthesis and the determination of the degree of the loosening. Besides, the prosthesis stability can be more useful with the numerical value that the scoring system will be developed.

ACKNOWLEDGMENT

This work supported by The Scientific and Technological Research Council of Turkey (TUBITAK) under project no 216M316. The corresponding author, Talip Çelik, thanks TUBITAK 2211-C Scholarship program.

REFERENCES

[1]. H. Malchau, P. Herberts, T. Eisler, G. Garellick, and P. Soderman, "The Swedish Total Hip Replacement Register " *J. Bone Joint Surg. Am.*, vol. 86-A, pp. 2-20, 2002.
[2]. K. E. Dreinhofer, "Indications for total hip replacement: comparison of assessments of orthopaedic surgeons and referring physicians," Annals of the Rheumatic Diseases, vol. 65, pp. 1346-1350, 2006.
[3]. A. P. Georgiou and J. L. Cunningham, "Accurate diagnosis of hip prosthesis loosening using a vibrational technique," Clinical Biomechanics, vol. 16, pp. 315-323, 2001.
[4]. L. C. Pastrav, S. V. N. Jaecques, I. Jonkers, G. Perre, and M. Mulier, "In vivo evaluation of a vibration analysis technique for the per-operative monitoring of the fixation of hip prostheses," Journal of Orthopaedic Surgery and Research, vol. 4, p. 10, 2009.
[5]. J. S. Rieger, S. Jaeger, C. Schuld, J. P. Kretzer, and R. G. Bitsch, "A vibrational technique for diagnosing loosened total hip endoprostheses: An experimental sawbone study," Medical Engineering & Physics, vol. 35, pp. 329-337, 2013.
[6]. A. A. Alshuhri, T. P. Holsgrove, A. W. Miles, and J. L. Cunningham, "Development of a non-invasive diagnostic technique for acetabular component loosening in total hip replacements," Medical Engineering & Physics, vol. 37, pp. 739-745, 2015.

Journal Homepage : http://dergipark.gov.tr/ejens
EJENS
European Journal of Engineering and Natural Sciences
CODEN: EJENS
DergiPark AKADEMİK

Investigation of Heat Transfer from Heated Square Patterned Surfaces in a Rectangular Channel with an Air Jet Impingement

Dogan Engin Alnak[1], Koray Karabulut[2]*, Ferhat Koca[1]
[1]*Sivas Cumhuriyet University, Department of Automotive Engineering, Technology Faculty, 58140, Sivas, Turkey.*
[2]*Sivas Cumhuriyet University, Department of Electric and Energ, Sivas Vocational High School, 58140, Sivas, Turkey.*
**Corresponding Author email: kkarabulut@cumhuriyet.edu.tr*

Abstract

Heat transfer is a very important precaution for proper design and safe operation of electronic packages and systems. Impinging jets are usually used to solve thermal problems of electronic components in industry due to providing a good heat transfer performance. In this study, cooling of copper plate with five square patterned surfaces inside a rectangular channel comprising of one open and three blocked sides was numerically investigated by using a single air jet flow. The numerical computations were performed by solving a steady, three-dimensional Navier-Stokes equation and an energy equation by using Ansys-Fluent 17.0 software program with k-ε turbulance model. Air was taken as working fluid with inlet temperature of 300 K. A constant heat flux with 1000 W/m^2 was applied to square patterned surfaces while the top and side surfaces were adiabatic. The study was carried out for different Reynolds numbers (Re) of 4000, 6000, 8000 and 10000 and different jet-to-plate distances (H/D_h) of 4, 6, 10 and 12. The numerical results agreed well with the numerical and experimental datas of study existed in literature. The results were presented as the variations of the mean Nu numbers and temperatures for each square patterned indentation surface. The temperature and velocity distributions of jet fluid flow and mean temperature and Nu values of whole five square patterned surfaces and value of air jet outlet temperature were also researched for different Re numbers and H/D_h ratios. It was seen that increasing the Re number increases the Nusselt number for all cases. Average Nusselt number increases of 59.28% from Re=4000 to Re=10000 for H/D_h=4. However, Nu number was less sensitive to H/D_h ratio in the range of H/D_h=4-12. Average Nusselt number decreases of 9.11% from H/D_h=4 to H/D_h=12 for Re=6000. The highest average Nusselt number was attained for Re=10000 and H/D_h =6.

Key words

Impingement Air Jet, Patterned Surface, Square Channel, Numerical Analysis

1. INTRODUCTION

Rapid improvement of technology leads electronic devices to have both more compact and higher processing power. The reliability of the electronic parts of a system is a primarily factor in the overall reliability of the system. Electronic components depend on transition of the electric current to implement their duties and they become potential regions for excessive heating, since the current flow through a resistance brings along heat generation. Unless properly designed and controlled, high rates of heat generation cause to high operating temperatures for electronic device, which endangers its reliability and safety. Besides, the high thermal stresses in the solder joints

of the electronic equipments mounted on circuit boards resulting from temperature variations are major reasons of defects. Therefore, thermal control has become increasingly important in the design and operation of the electronic devices. For this purpose, it is needed to develop new cooling techniques instead of conventional technology. Impinging liquid and gaseous jets are used widely because of their easy application and high heat transfer coefficient. Jet impingement is employed for heating, cooling and drying in cases where coefficients of high heat transfer are aimed. Thus, it is considered that jet impingement can be used for cooling of the electronic components generating high heat and having high performance. Because high heat producing electronics evolve, it becomes proof that using air cooling alone will not provide adequate performance. Jet impingement has the ability to take away large amounts of heat from these environments with high heat flux. In the one of the earliest investigations into jet impingement flow was carried out a review of literature that included several examples [1]. In an another review study, Carlomagno and Ianiro [2] did a detailed work of the effects of Reynolds number and jet to plate distance on the heat transfer and flow physics of the impinging jets. Argus et al. [3] researched jet flow and heat transfer by using only one jet, numerically. Popovac and Hanjalic [4] investigated cooling of a heated cubic plate using one impingement jet. Yang and Hwang [5] exhibited numerical simulations of flow properties of a turbulent slot jet impinging on convex surface with a semi-cylindrical. Mushatat [6] performed a numerical study in order to study heat transfer and turbulent flow characteristics of impinging slot jets. Zuckerman and Lior [7] numerically analyzed the effect of nozzle type on initial turbulance, pressure drop, shearing force of free jet and jet velocity profile. They also described various experimental and computational techniques from other authors. Before submitting your final paper, check that the format conforms to this template. Specifically, check the appearance of the title and author block, the appearance of section headings, document margins, column width and other features. Please make sure that the use of other languages in figures and tables is avoided.

Different from the literature, it was mainly carried out numerical investigation of heat transfer from heated square patterned surfaces, inside a rectangular channel having three closed and one open side by using an air jet with single slot in the present work. The slot jet was mounted next to closed side. Air jet geometry and channel were designed of similar to an implementation of cooling of electronic components inside various devices. The numerical computations were performed by solving a steady, three-dimensional Navier-Stokes equation and an energy equation by using Ansys-Fluent 17.0 software program with k-ε turbulance model. Air was used as working fluid with inlet temperature of 300 K. It was exerted to a constant heat flux ($\ddot{q}$) with 1000 W/m^2 on square patterned surfaces. The numerical results agreed well with the numerical and experimental datas of study existed in literature. The results were presented as the variations of the mean Nu numbers and temperatures for each square patterned indentation surface. The temperature and velocity distributions of jet fluid flow and mean temperature and Nu values of whole five square patterned surfaces and values of air jet outlet temperature were also investigated for different Re numbers and H/D_h ratios.

2. NUMERICAL METHOD

An easy way to comply with the symposium paper formatting requirements is to use this document as a template and simply type your text into it.

The aim of finite volume method is to break down the domain of the problem into a finite number of elements to be solved to find a solution for each of these sections and then by uniting these solutions to find a general solution to the problem. This method uses a technique which is based on the control volume for transforming heat flow equations into algebraic equations which can be solved numerically. In other words, this technique is based on the principle of taking the heat flow equations integration in each control volume. This integration result provides equations which characterize each control volume which occurs. For preparing the most appropriate grid model, a fine grid should be formed in regions where the change in variables such as velocity, pressure and temperature is bigger. Therefore, the finest grid was especially used for the channel surfaces with the indentation and in other zones a sparser grid was preferred. Convergence of the computations was stopped for the continuity and the momentum equations when residues were less than 10^{-6} and for the energy equation when residues were less than 10^{-7}. A grid structure which consisted of tetrahedral was used for simulation. Also, a standard k-ε turbulance model was performed for the selected model with square patterned surfaces in the numerical investigations.

The flow and heat transfer through the geometry are governed by the partial differential equation derived from the laws of conservation of mass, momentum and energy with steady state conditions without a body force, which are expressed as follows [8].

Continuity equation

$$\frac{\partial u}{\partial x}+\frac{\partial v}{\partial y}+\frac{\partial w}{\partial z}=0 \tag{1}$$

Momentum equation

x momentum equation

$$\rho\left(u\frac{\partial u}{\partial x}+v\frac{\partial u}{\partial y}+w\frac{\partial u}{\partial z}\right)=-\frac{\partial p}{dx}+\mu\left(\frac{\partial^2 u}{\partial x^2}+\frac{\partial^2 u}{\partial y^2}+\frac{\partial^2 u}{\partial z^2}\right) \tag{2.1}$$

y momentum equation

$$\rho\left(u\frac{\partial v}{\partial x}+v\frac{\partial v}{\partial y}+w\frac{\partial v}{\partial z}\right)=-\frac{\partial p}{\partial y}+\mu\left(\frac{\partial^2 v}{\partial x^2}+\frac{\partial^2 v}{\partial y^2}+\frac{\partial^2 v}{\partial z^2}\right) \tag{2.2}$$

z momentum equation

$$\rho\left(u\frac{\partial w}{\partial x}+v\frac{\partial w}{\partial y}+w\frac{\partial w}{\partial z}\right)=-\frac{\partial p}{\partial z}+\mu\left(\frac{\partial^2 w}{\partial x^2}+\frac{\partial^2 w}{\partial y^2}+\frac{\partial^2 w}{\partial z^2}\right) \tag{2.3}$$

Energy equation

$$u\frac{\partial T}{\partial x}+v\frac{\partial T}{\partial y}+w\frac{\partial T}{\partial z}=\left(\frac{k}{\rho c_p}\right)\left(\frac{\partial^2 T}{\partial x^2}+\frac{\partial^2 T}{\partial y^2}+\frac{\partial^2 T}{\partial z^2}\right) \tag{3}$$

In the equations, ρ is density, μ dynamic viscosity, p pressure, k thermal conductivity, T temperature, c_p specific heat and u, v, w are velocities of the x, y and z direction, respectively.

In the used standard k-ε turbulance model, the turbulence kinetic energy and its rate of dissipation and the viscous dissipation term are used.

Steady flow turbulence kinetic energy equation

$$\frac{\partial\left(\rho u k'\right)}{\partial x}+\frac{\partial\left(\rho v k'\right)}{\partial y}+\frac{\partial\left(\rho w k'\right)}{\partial z}=\frac{\partial}{\partial x}\left(\frac{\mu_t}{\sigma_k}\frac{\partial k'}{\partial x}\right)+\frac{\partial}{\partial y}\left(\frac{\mu_t}{\sigma_k}\frac{\partial k'}{\partial y}\right)+\frac{\partial}{\partial z}\left(\frac{\mu_t}{\sigma_k}\frac{\partial k'}{\partial z}\right)+\mu_t\phi-\rho\varepsilon \tag{4}$$

Turbulent viscosity

$$\mu_t=C_\mu.\rho.\frac{k'^2}{\varepsilon} \tag{5}$$

Turbulence kinetic energy

$$k'=\frac{1}{2}\left(\overline{u'^2}+\overline{v'^2}+\overline{w'^2}\right) \tag{6}$$

Viscous dissipation term

$$\phi=2\mu\left[\left(\frac{\partial u}{\partial x}\right)^2+\left(\frac{\partial v}{\partial y}\right)^2\right]+\mu\left(\frac{\partial v}{\partial x}+\frac{\partial u}{\partial y}\right)^2 \tag{7}$$

Turbulence kinetic energy disappearance equation

$$\frac{\partial\left(\rho u\varepsilon\right)}{\partial x}+\frac{\partial\left(\rho v\varepsilon\right)}{\partial y}+\frac{\partial\left(\rho w\varepsilon\right)}{\partial z}=\frac{\partial}{\partial x}\left(\frac{\mu_t}{\sigma_\varepsilon}\frac{\partial\varepsilon}{\partial x}\right)+\frac{\partial}{\partial y}\left(\frac{\mu_t}{\sigma_\varepsilon}\frac{\partial\varepsilon}{\partial y}\right)+\frac{\partial}{\partial z}\left(\frac{\mu_t}{\sigma_\varepsilon}\frac{\partial\varepsilon}{\partial z}\right)+C_{1\varepsilon}\mu_t\frac{\varepsilon}{k'}\phi-C_{2\varepsilon}\rho\frac{\varepsilon^2}{k'} \tag{8}$$

The model constants C_μ, $C_{1\varepsilon}$, $C_{2\varepsilon}$, σ_k and σ_ε have typically default values for used standard k-ε turbulance model [8]. The values of these constants have been arrived at by numerous iterations of data fitting for a wide range of turbulent flows. These are as follows;

C_μ =0.09, $C_{1\varepsilon}$ =1.44, $C_{2\varepsilon}$ =1.92, σ_k=1 and σ_ε=1.3.

Reynolds number is calculated by the equation given below;

$$Re=\frac{V_\infty.D_h}{\nu} \tag{9}$$

Here, D_h is the hydraulic diameter of the jet inlet

$$D_h = \frac{4A_c}{P} = \frac{4(aW)}{2(a+W)} \tag{10}$$

where A_c is the cross-section area of the jet inlet, P is the perimeter of the jet inlet.

The Nusselt number is evaluated as the conductive heat transfer rate of the fluid over the solid boundary equal to the convective heat rate as:

$$-k\left(\frac{dT}{dn}\right)_{surface} = h\left(T_\infty - T_s\right) \text{ and } Nu = \frac{h.D_h}{k} \tag{11}$$

Where h is the local heat transfer coefficient on the surface, n is the vertical direction to isotherm and the local Nusselt number is obtained as above.

3. GEOMETRIC MODEL

Perspective view of the channel having sizes was shown in Fig. 1. The boundary conditions can also be seen in this figure. The jet nozzle hydraulic diameter (D_h) was kept at 9.9 mm, the length (L) and width (W) of the channel were taken as 200 mm and 50 mm, respectively. 5.5x50 mm rectangular nozzle with an inlet velocity ranging between 6.23 and 15.58 m/s was used in the study. Uniform velocity profile for jet inlet was existed in the inlet of the rectangular nozzle. The channel height was determined at different measurements as $4xD_h$, $6xD_h$, $10xD_h$ and $12xD_h$. While space between two indentations was taken as D_h, indentation width and height were $2xD_h$ and D_h, respectively. There are five surfaces with square indentation and the constant heat flux ($\ddot{q}$) with 1000 W/m^2 was applied to only these surfaces for all simulations when the top and side surfaces were adiabatic. However, the Reynolds numbers (Re) of the jet ranged from 4000 to 10000.

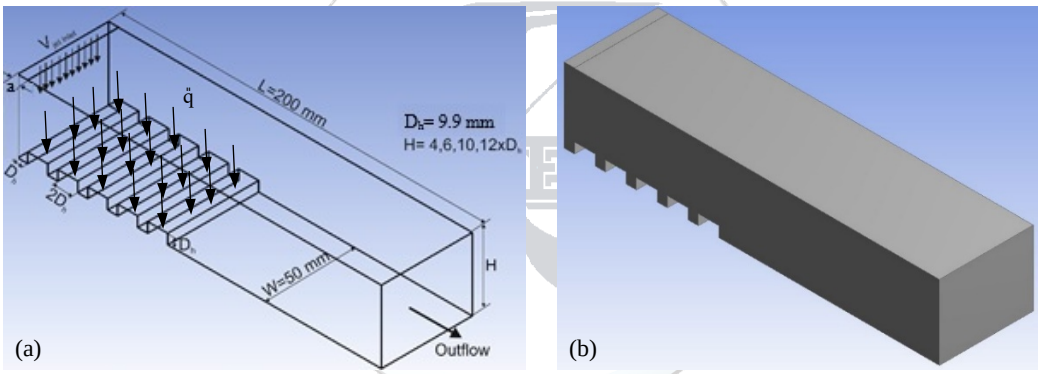

Figure. 1. Perspective view of the channel (a) Domain with boundary conditions and sizes (b) CFD simulation domain

The study was conducted under the following assumptions:

i) The flow field was assumed to be three-dimensional, steady-state and turbulent for the channel;
ii) Calculations were carried out for incompressible fluid;
iii) Air was used as working fluid for the cooling of indentation surface;
iv) Constant heat flux of 1000 W/m^2 was applied to indentation surfaces;
v) Thermal properties of the fluid were constant;
vi) There was no heat generation for both the jet fluid and the solid surfaces.

4. RESULTS AND DISCUSSION

Figure 2 exhibits a comparison of the effects of Re number with 6000 and 8000 on the Nu number as experimental and numerical for jet-to-plate distance (H/D_h) value of 6 between Kilic et al. [9] and the present study numerically. The comparison was performed for smooth copper plate surface that was used in [9] at Re numbers of 6000 and 8000. While the deviation of the Nu number between the experimental results of Kilic et al. [9] and the present numerical study is 3.99% at Re=6000, it is found as 1% for numerical results at the impingement region. However, difference between the experimental and numerical results increases for Re=8000 at the impingement region due to higher turbulance intensity. When the deviation of numerical results with experimental is 9.15% due to higher turbulance intensity in this region, the difference is 1.02% for the numerical results when compared the present study with Kilic et al. [9]. Therefore, it can be said that the results of the present study are well comparable with

experimental and numerical study results of the Kilic et al. [9] and the numerical study is reasonable and appropriate.

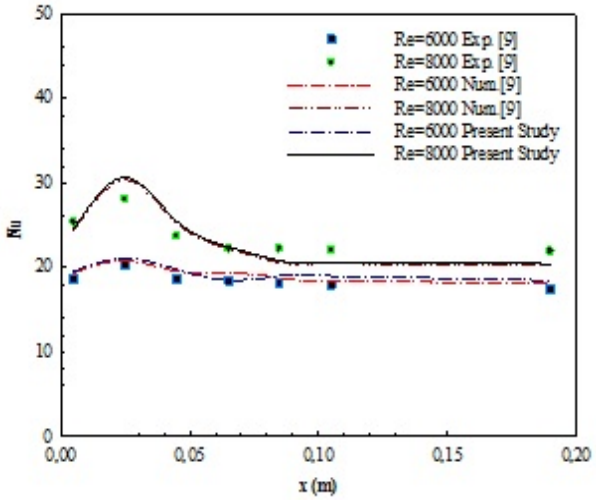

Figure 2. Comparison of the present results and those of Kilic et al. [9]

To determine the effect of the grid size on the mean Nu number and outlet temperature of jet air ($T_{out\text{-}jet}$), a grid independence test (as shown in Table 1) was carried out for H/Dh=4 and Re=4000. The test showed that 1714584 grids on a duct cross-section are adequate (< 0.01% difference compared with 1954741 grids). Mesh structure of the channel having square patterned surfaces was also shown in Fig. 3 with zoomed image in order to clearly see the mesh shape of the square pattern.

Table 1. Grid independence test results for Nu_m and $T_{out\text{-}jet}$

Mesh Numbers	Nu_m	$T_{out\text{-}jet}$ (K)
1525412	9.7189	324.648
1714584	9.7298	324.663
1954741	9.7297	324.665

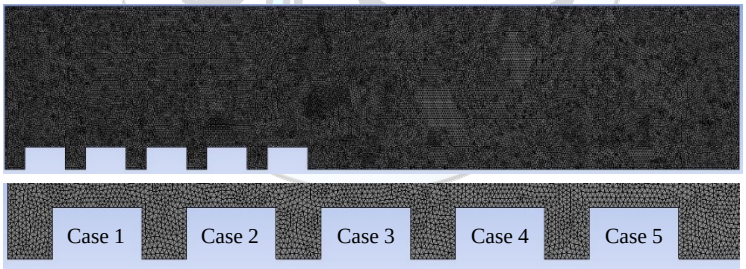

Figure 3. Mesh structure of the channel with circle patterned surface used in calculations

The effects of Reynolds number and H/D_h ratios on the Nusselt number variation for different location cases of rectangular patterned surfaces are shown in Fig. 4. Cases in the graphs indicates the location order of the rectangular surfaces beginning from the left side of the channel. Enhancement in Re number increases the Nu number on the surfaces of the rectangular patterned. Recirculations come into existence at the bottom of the left wall for all Reynolds numbers. These recirculations cause a change of direction of the jet flow. Therefore, values of the highest local Nu number were determined for the case 2 for all Re numbers. However, because the effect of recirculation increases on the location place of the highest local Nu number with increase of H/D_h ratio, the local Nu number values change according to ratio of H/D_h at the different cases from 1 to 5. Average Nusselt number increases of 59.28% from Re=4000 to Re=10000 for H/D_h=4. Besides, Nu number was less sensitive to H/D_h ratio in the range of H/D_h=4-12. Average Nusselt number decreases of 9.11 % from H/D_h=4 to H/D_h=12 for Re=6000 because of a decline of turbulance intensity. Also, the highest average Nusselt number was attained for Re=10000 and H/D_h=6.

Fig. 5 exhibits the mean surface temperatures of the square patterned for different jet-to-plate distances (H/D_h) of 4, 6, 10 and 12 and Re numbers. Increasing of the Re number provides to reducing of the mean surface temperatures by causing to enhance the turbulence intensity and so heat transfer. However, H/D_h increment from 4 to 12 sharply affects the surface temperature of the case 1 depending on directed of the jet flow thanks to recirculations. While the lowest surface temperature value was obtained for the case of 2, the case 5 was found to have the highest

surface temperature due to losing the jet effect and reduction of flow velocity toward exit of the channel for all Re numbers (Figs. 5a-d). A surface temperature increase of 1.83% was observed from the case 2 to case 5 for H/D_h=4 and Re=10000.

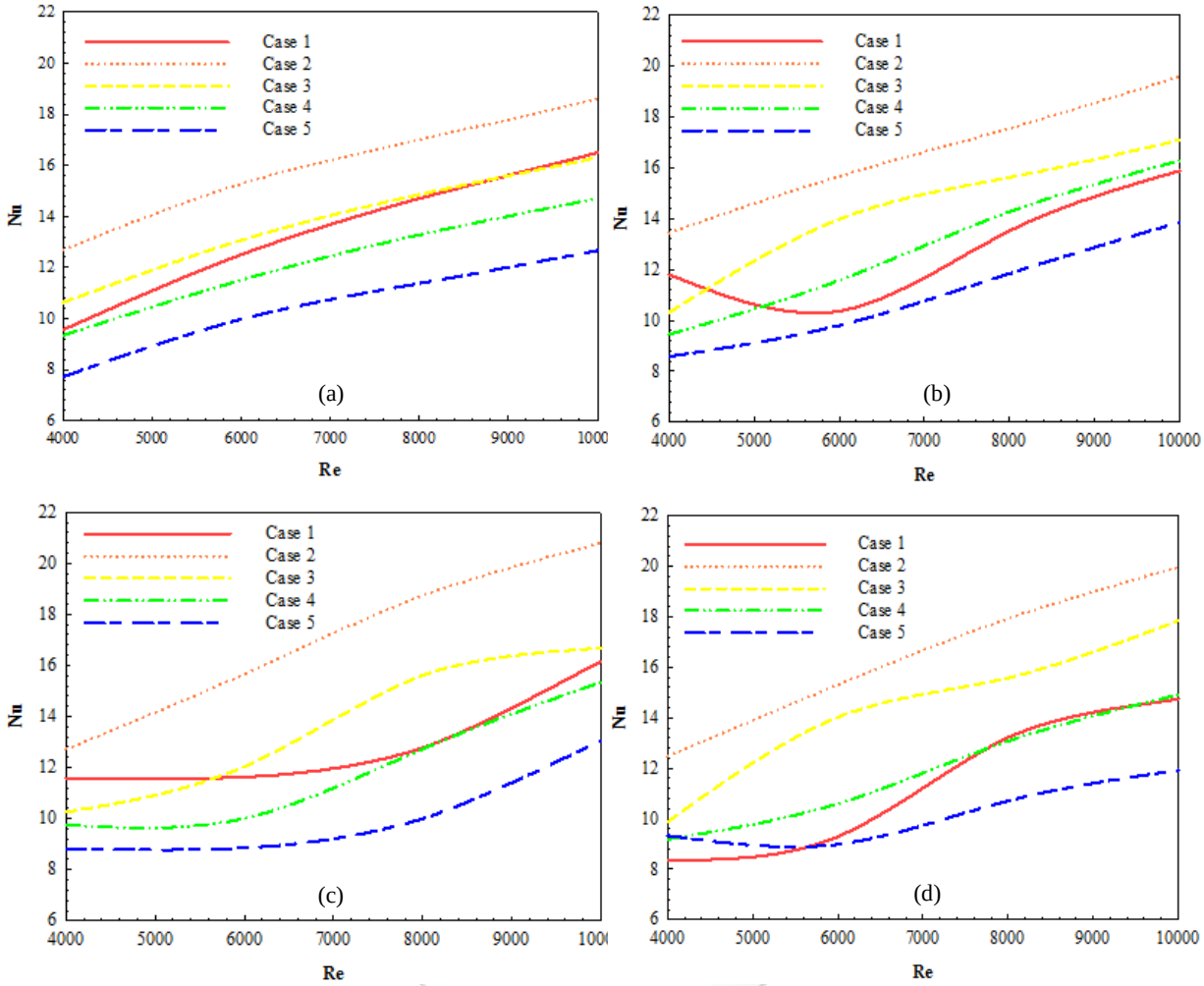

Figure. 4. Variations of mean Nu number versus different Re number for different H/D_h and cases (a) H/D_h=4 (b) H/D_h=6 (c) H/D_h=10 and (d) H/D_h=12

It can be seen in Figs. 6A and B, recirculations happen at the bottom of the left wall for analyzed Reynolds numbers. However, these occurred recirculations affect main jet flow and cause to change location of maximum heat transfer point. Besides, recirculation sizes decreases with increasing Re number from 4000 to 10000 due to prevention of expansion of recirculations by increasing jet flow velocity. When the velocity of jet flow is high at the impingement region, it reduces toward channel outlet. Therefore, surface temperatures of the square indentations increase. Because of the separation of the jet flow from the last square surface, recirculations occur. One can see that recirculations increase with increasing jet-to-plate distance H/D_h. Thus, thickness of thermal boundary layer enhances with enhancing recirculations, which causes to increase the temperature. Increasing channel height causes to decrease length of wall jet region. The reason for this is reducing of flow velocity at a longer channel height. Decreasing flow velocity, on the surface of copper indentation plate, causes an increase in temperature.

Mean Nu numbers and surface temperatures of square indentations and air jet temperature at the outlet of the channel for different Re numbers and H/D_h ratios are given in Table 2. When Nu_m increases with increasing of Re, it decreases with increasing H/D_h ratio from 4 to 12 due to reducing air jet velocity in the impingement region. However, mean surface temperatures of the square indentations enhance with enhancing jet-to-plate distance H/D_h but they decrease with increasing Re number. Besides, outlet temperature of the air jet decreases with enhancing Re number and H/D_h ratio.

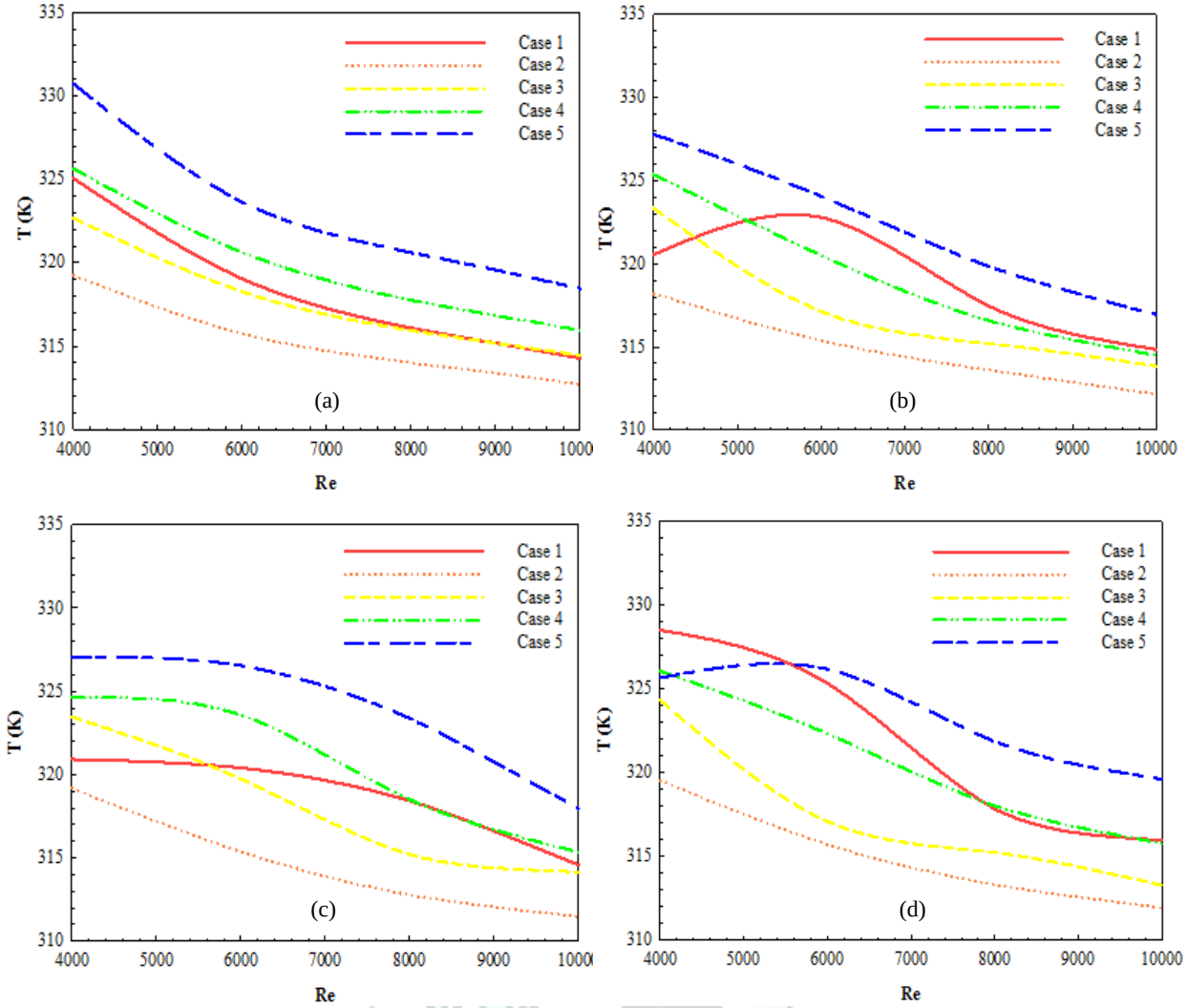

Figure. 5. Variations of mean surface temperature versus different Re number for different H/D_h and cases (a) H/D_h=4 (b) H/D_h=6 (c) H/D_h=10 and (d) H/D_h=12

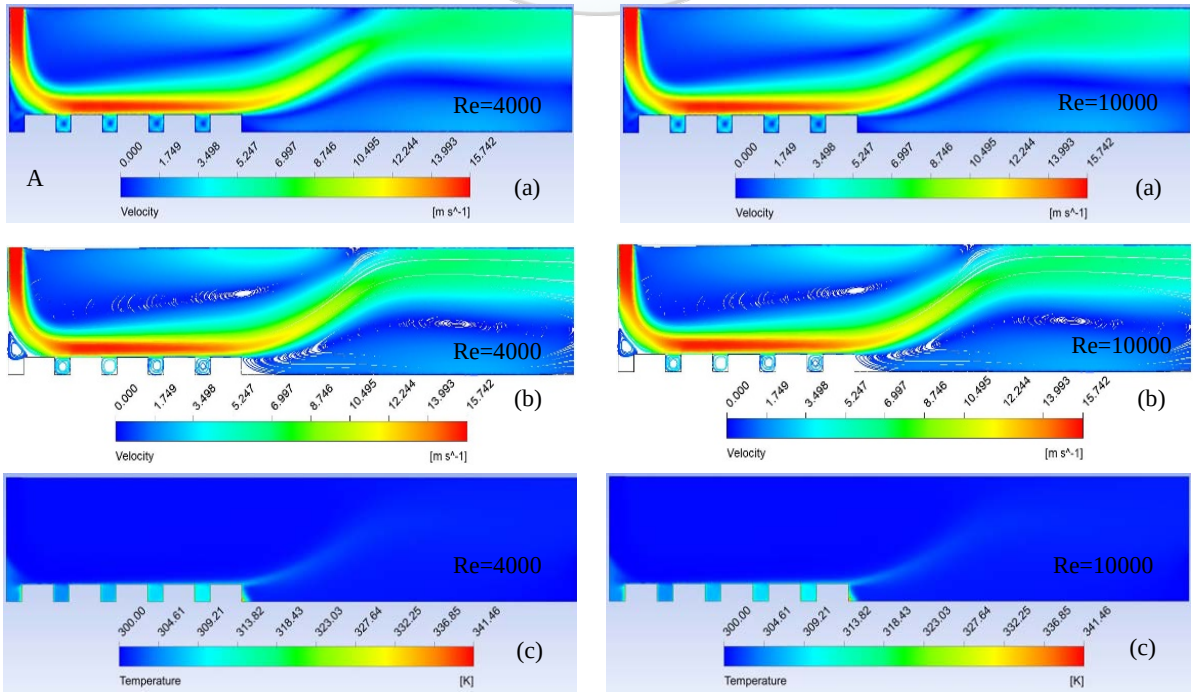

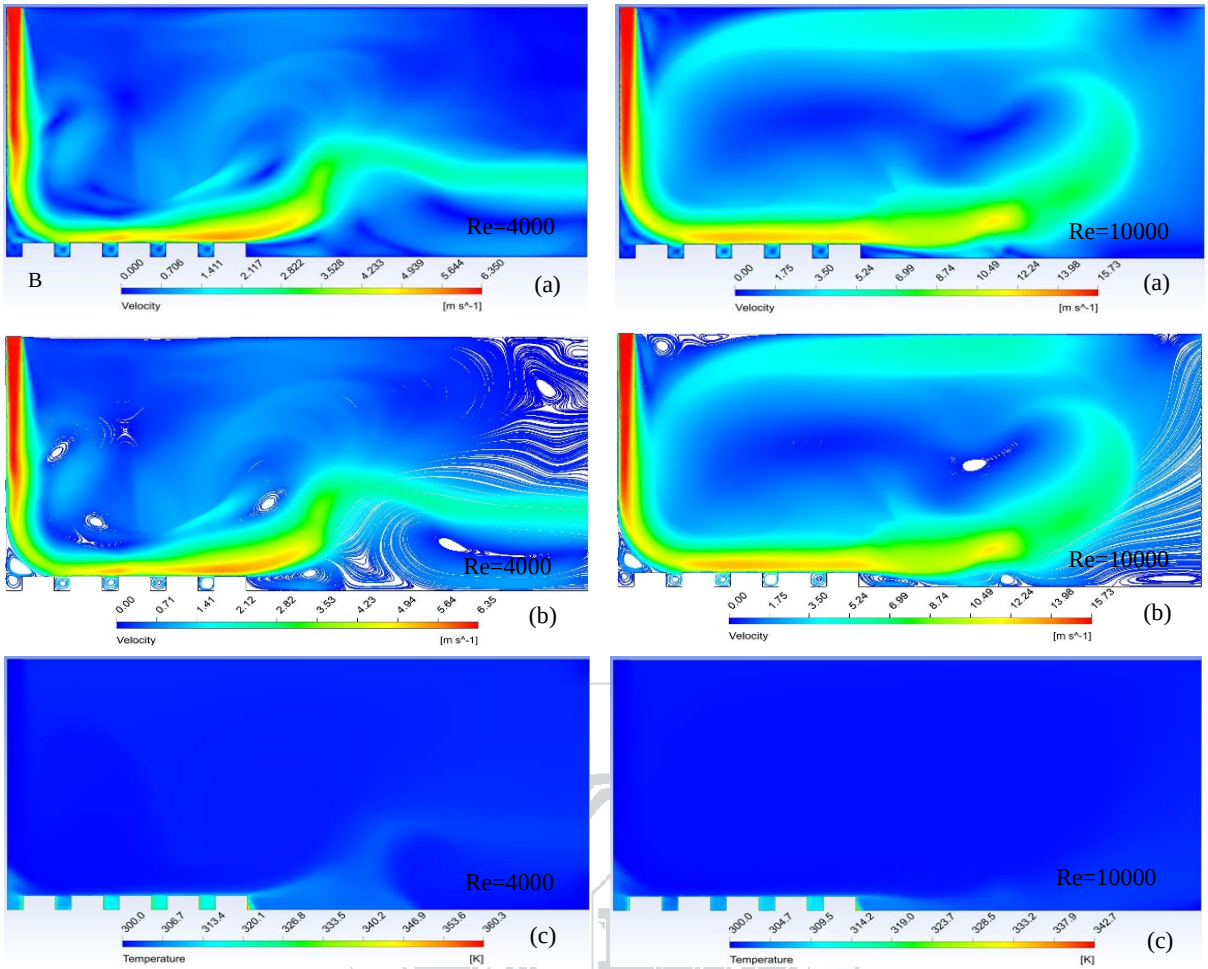

Figure. 6. A-H/D_h=4, B- H/D_h=10 a) Velocity b) Streamline c) Temperature distributions for different Re numbers

Table 2. Results of Nu_m, T_{sm} and $T_{out\text{-}jet}$ air for different Re and H/D_h

Square Surface	**Nu_m**		**T_{sm}**		**$T_{out\text{-}air\ jet}$**	
	H/D_h=4	**H/D_h==12**	**H/D_h==4**	**H/D_h==12**	**H/D_h==4**	**H/D_h==12**
Re=4000	9.7298	9.6675	324.663	324.802	302.564	302.541
Re=6000	12.2246	11.1108	319.454	321.312	301.698	301.691
Re=10000	15.4981	15.3918	315.171	315.293	301.001	301.043

5. CONCLUSION

The present study was conducted into the numerical research of heat transfer from a heated square patterned copper surface, inside a rectangular channel by using a single jet flow. The numerical results were compared with the numerical and experimental datas of study existed in literature and found they were in well agreement. The results were presented as the variations of the mean Nu numbers and temperatures for each square patterned indentation surface. The temperature and velocity distributions and streamlines of jet fluid flow and mean surface temperature and Nu values of whole square surfaces and values of air jet outlet temperature were also analyzed for different Re numbers and jet-to-plate distance H/D_h ratios. The following conclusions can be drawn from the numerical results;

-Increase in Reynolds number increases the heat transfer at all jet-to-plate distances. Average Nusselt number increases of 59.28% from Re=4000 to Re=10000 for H/D_h=4. Besides, Nu number was less sensitive to H/D_h ratio in the range of H/D_h=4-12. Average Nusselt number decreases of 9.11% from H/D_h=4 to H/D_h=12 for Re=6000 because of a decline of turbulance intensity. Also, the highest average Nusselt number was attained for Re=10000 and H/D_h=6.

-Recirculations occur at the bottom of the left wall for all Reynolds numbers. These recirculations cause a change of direction of the jet flow. Thus, values of the highest local Nu number were determined for the case 2 for all Re numbers.

- Occurred recirculation sizes decrease with increasing Re number from 4000 to 10000 due to prevention of expansion of recirculations by increasing jet flow velocity.

-When the velocity of jet flow is high at the impingement region, it reduces toward channel outlet. Therefore, surface temperatures of the square indentations increase.

- Increasing the channel height causes to decrease length of wall jet region. The reason for this is reducing of flow velocity at a longer channel height. Decreasing flow velocity, on the surface of copper indentation plate, causes an increase in temperature.

-In a conclusion, the heat transfer, including local and average Nusselt numbers, are significantly affected by jet Reynolds numbers; while it is less sensitive to jet-to-plate distance. Also, it is considered that geometry of air jet and channel used in this study can be employed to cool electronic components due to resembling various electronic equipment application.

REFERENCES

[1]. B. W. Webb and C. Ma, “Single-phase liquid jet impingement heat transfer”, Adv. Heat Transf., vol. 26 pp. 105–117, 1995.
[2]. G. M. Carlomagno and A. Ianiro, “Thermo-fluid-dynamics of submerged jets impinging at short nozzle-to-plate distance: a review”. Exp Thermal Fluid Sci., vol. 58, pp. 15–35, 2014.
[3]. E. Argus, M. A. Rady and S. A. Nada, “A numerical investigation and parametric study of cooling an array of multiple protruding heat sources by a laminar slot air jet”. Int J Heat Mass Transf., vol. 28, pp. 787–805, 2006.
[4]. M. Popovac and K. Hanjalic K, “Large-eddy simulation of flow over a jet-impinged wall-mounted cube in a cross stream”, Int J Heat Fluid Flow, vol. 28, pp. 1360–1378, 2007.
[5]. Y. T. Yang, C. H. Hwang, “Numerical simulations on the hydrodynamics of a turbulent slot jet on a semi-cylindrical convex surface”, Num Heat Transfer, vol. 46, pp. 995–1008, 2004.
[6]. K. S. Mushatat, “Analysis of the turbulent flow and heat transfer of the impingement cooling in a channel with cross flow”, Eng Sci, vol. 18, pp. 101–122, 2007.
[7]. N. Zuckerman and N. Lior, “Jet impingement heat transfer: physics, correlations, and numerical modeling”, Adv. Heat Transf., vol. 39, pp. 565–631, 2006.
[8]. FLUENT User's Guide, Fluent Inc. Lebanon, NH, 2003.
[9]. M. Kilic, T. Calisir, S. Baskaya, “Experimental and numerical study of heat transfer from a heated flat plate in a rectangular channel with an impinging air jet”, J Braz. Soc. Mech. Sci. Eng., vol. 39, pp. 329-344, 2017.

ACKNOWLEGMENT

The authors would like to thank Scientific Research Projects Coordination Unit of Sivas Cumhuriyet University (Sivas/Turkey) for their financial support to this research under project number TEKNO-021.

Journal Homepage : http://dergipark.gov.tr/ejens
EJENS
European Journal of Engineering and Natural Sciences
CODEN: EJENS
DergiPark AKADEMİK

The Usage of Modified Chitosan for the Removal of Hexavalent Chromium from Waste Water

Nuran Deveci Aksoy[1]*, Göknur Türsün[1]
[1]*Istanbul Technical University, Department of Chemical Engineering, 3426, Maslak/Istanbul, Turkey.*
**Corresponding Author email: nuran@itu.edu.tr*

Abstract

This study presents the results of chromate adsorption upon chitosan modified with thiourea, glutaraldehyde. Firstly modified chitosan was synthesized by using thiourea, glutaraldehyde and chitosan at different molar ratios and adsorption capacities were compared to the original chitosan. The modified chitosan showed higher Cr (VI) retention performance than the original chitosan. While the original chitosan had a percent removal of 32% at an initial concentration of 50 ppm, the percentage of chitosan removal improved to 99.9%. Kinetic and thermodynamic constants are determined at appropriate ambient conditions and adsorption is defined by appropriate adsorption isotherms. Langmuir isotherms were found to be suitable for characterizing the adsorption of chitosan with the modified Cr (VI) ions. Under appropriate experimental conditions, percentages of removal in Cr (VI) removal studies by adsorption using modified chitosan reached 99% and adsorption capacity of 442 mg/g was observed.Characterization of the modified chitosan and original chitosan were characterized by FTIR (Fourier Transform Infrared Spectroscopy), TGA (Thermal Gravimetric Analysis), XRD (X-ray Diffraction) and DSC (Differential Scanning Calorimetry).

Key words

Adsorption, Chitosan, Chromium(VI), Wastewater Treatmant

1. INTRODUCTION

The pollution of water resources due to the disposal of heavy metals has been an increasing worldwide concern for the last few decades. Heavy metals have a harmful effect on human physiology and other biological systems when they are found above the tolerance levels [1]. The presence of trivalent and hexavalent chromium in the environment is the cause of many well documented toxic effects. The maximum levels permitted in wastewater are 5 mg/L for trivalent and 0.05 mg/L for hexavalent chromium [2].

Chromium is a transition element which is located to Group VI-B of the periodical table and its toxic effect has been proven. Chromium exists in environment both as trivalent Cr(III) and hexavalent Cr(VI) forms. Hexavalent chromium is toxic and carcinogenic, while trivalent is relatively harmless [3]. High concentrations of Cr (VI) are present in the wastewater of leather, textile, mining and metal industries. These high concentration must be reduced below the permissible limits before Cr(VI) is discharged into the receiving enviroment [4]. Activated carbon is the world's most widely used adsorbent for heavy metal removal from waste water. Despite its

efficient use, active carbon is expensive. Due to the disadvantage, research interest into the production of alternative adsorbents to replace the costly activated carbon. Because of their low cost, natural materials such as chitosan, zeolites, clay and fly ash are classified as low-cost adsorbents [5].

In recent years, studies on the use of chitosan as an adsorbent in heavy metal removal have been investigated. Chitosan is a polymer with polysaccharide structure obtained by alkali deacetylation of chitin. Chitin is the second most common biopolymer after cellulose in nature.It is highly reactive as an adsorbent due to the inclusion of amine and hydroxyl groups in the structure [6]. The degree of deacetylation is one of the most important chemical properties that can affect chitosan performance in many applications. The degree of deacetylation, which determines the content of free amino groups in polysaccharides, can be used to differentiate between chitin and chitosan. FTIR analysis was used to determine the degree of deacetylation of chitosan [7]. Various techniques have been employed for the treatment of heavy metals, including chemical precipitation, mebran processes, ion-exchange and adsorption. Adsorption technique is economically suitable and technically practicable to remove hexavalent chromium from waste water as it requires less operative controls [8].

Briefly, the aim of this study was to investigate the Cr(VI) adsorption performance of chitosan modified with thiourea, glutaraldehyde.

2. MATERIALS AND METHODS

All the chemicals used were of analytical grade. A stock solution of chromium (VI) (100 mg/L) was prepared by dissolving 3.73 g of $K_2Cr_2O_4$ in 1000 mL distilled water. Desired concentrations were obtained by diluting the stock solution with distilled water. Chitosan was obtained from Sigma and and classified to average particle diameterof 0.125–0.250 mm.

2.1. Degree of Chitosan Deacetylation

The degree of deacetylation is one of the most important chemical properties that can effect chitosan performance in many applications. The degree of deacetylation, which determines the content of free amino groups in polysaccharides, can be used to differentiate between chitin and chitosan. To determine the deacetylation degree of chitosan, 1 g of chitosan 100 mL of 5% acetic acid solution was added. It was mixed at a speed of 150 rpm at a temperature of 30º for 6 hours to dissolve. At the end of the process a viscous solution was obtained and analyzed by FTIR (Fourier Transform Infrared) spectrometer. It is expected that the structure will be modified with thiourea in addition to the amine groups and the sulphide will have a positive effect on chromium removal [9].

Considering these situations, the strategy of modification has been determined. Different amounts of thiourea and glutaraldehyde were studied to investigate the effect of thiourea and glutaraldehyde content on the adsorption capacity.

2.2. Chitosan Modification

Chitosan is soluble in dilute mineral acids except sulfuric acid. For this reason, chemical stability should be increased by chemical treatments such as glutaraldehyde cross-linking for application in a chemical acidic environment. The process creates new bonds between the chains of chitosan, ensuring that the polymer is resistant to dissolution even in strong solutions such as hydrochloric acid solution [10]. In addition, the presence of chitosan amine groups is an important influence on the absorption of a good absorbent. It is possible to increase the adsorption capacity by increasing the amine groups [9].

Considering these situations, the strategy of modification has been determined. Different amounts of thiourea and glutaraldehyde were studied to investigate the effect of thiourea and glutaraldehyde content on the adsorption capacity. The thiourea and glutaraldehyde were reacted in 20 mL distilled water for 8 hours at 20 ºC [9]. Then, 1 g of chitosan was added and reacted for 72 hours. Modified chitosan filtration and washed several times with distilled water. Then, it was dried at 50 ºC for 24 hours. Dried chitosan samples are stored in a desiccator [9]. Different amounts of thiourea and

glutaraldehyde were studied to investigate the effect of thiourea and glutaraldehyde content on the adsorption capacity. The contents of the modified chitosan samples produced are listed in Table 1.

Table 1. Contents of Modified Chitosan Samples

Sample	Chitosan (g)	Glutaraldehyde (mL)	Thioürea (g)
KGT.1	1	1	-
KGT.2	1	2	-
KGT.3	1	4	-
KGT.4	1	8	-
KGT.5	1	1	1
KGT.6	1	2	1
KGT.7	1	4	1
KGT.8	1	8	1
KGT.9	1	1	2
KGT.10	1	2	2
KGT.11	1	4	2
KGT.12	1	8	2
KGT.13	1	1	4
KGT.14	1	2	4
KGT.15	1	4	4
KGT.16	1	8	4

2.3. Cr(VI) Adsorption Experiments

Stock solution of K_2CrO_4 (1000 ppm) was prepared and diluted as necessary to be used in batch adsorption experiments. The concentration of Cr(VI) was analyzed spectrophotometrically (Shimadzu UV 1240) at 540 nm using 1,5-diphenyl carbazide as the complexing agent [11,12].

The adsorption capacities of original chitosan and modified chitosan samples were determined under the conditions of 50 ppm initial Cr(VI) concentration, pH 2.0 and 1 g L^{-1} adsorbent dose. The removal extent and capacity were calculated from Eq. 1 and Eq. 2, respectively.

$$q_e = \frac{V_i C_i - V_e C_e}{W} \quad (1)$$

$$\text{Adsorption}(\%) = \frac{(A_0 - A)}{A_0} * 100 \quad (2)$$

where C_i and C_e are the initial and equilibrium Cr(VI) concentration of solution (mg L^{-1}), q_e is the equilibrium uptake capacity (mg g^{-1}), V is the volume of solution (L) and W is the mass of adsorbent (g). Where A_0 and A are the initial and final absorbance (nm) of the solution, respectively [13].

The effect of pH was studied within the range pH 1–8.0. Adjustments were made by small additions of 0.1 M HCl or 0.1 M NaOH. Cr(VI) solutions of 50 ppm were contacted with modified chitosan samples (0.4 g L^{-1}) and 250 ppm were contacted with modified chitosan samples (0.6 g L^{-1}) for 24 h. Time to reach equilibrium was investigated for initial concentrations (C_0) of 70 and 160 ppm. Samples were driven out at certain time intervals between 1 and 24 h and analyzed for residual Cr(VI) concentration. The effect of adsorbent dose was investigated within the range of 0.2 – 4 g L^{-1} using Cr(VI) solutions of 100 ppm and 250 ppm. Optimal conditions of pH, contact time and adsorbent dose were applied in isotherm studies. Cr(VI) solutions of different concentrations were

treated with modified chitosan samples, and collected data were fitted to Langmuir and Freundlich isotherm models.

2.4. Adsorbent Characterization

Identification of the crystalline species or impurities in original chitosan and the change in crystalline structure after modification with surfactant were provided by X-ray diffraction analysis. Thermalgravimetric analysis of original chitosan and modified chitosan samples was carried out by Perkin Elmer, Diamond TG/DTA in air atmosphere, within the temperature range of 30-1000 ºC with a heating rate of 10 ºC min^{-1}. The FTIR spectra of samples were recorded with Perkin Elmer Spectrum One Spectrophotometer within 4000–450 cm^{-1} as an average of four scans.

3. RESULT AND DISCUSSION

3.1. Chromium Removal with Chitosan and Modified Chitosan

3.1.1. Comparison of Original Chitosan and Modified Chitosan in Cr(VI) Removal

Firstly modified chitosan was synthesized by using thiourea, glutaraldehyde and chitosan at different molar ratios and adsorption capacities compared to the original chitosan were compared. The modified chitosan showed higher Cr (VI) retention performance than the original chitosan. While the original chitosan had a percent removal of 32% at an initial concentration of 50 ppm, the percentage of chitosan removal improved to 99.9%. The chrome Cr (VI) holding capacities and removal percentage of the original chitosan and modified chitosan are shown in Table 2.

Table 2: The Cr (VI) holding capacities and removal percentage of the original chitosan and modified chitosan

Sample Name	Amount of Retention (mg/g)	Removal Percentages (%)
KGT.1	46.62	89.24
KGT.2	45.36	90.73
KGT.3	48.45	96.91
KGT.4	49.94	99.88
KGT.5	47.22	94.44
KGT.6	47.47	94.93
KGT.7	48.45	96.91
KGT.8	47.59	95.18
KGT.9	44.37	88.75
KGT.10	48.45	96.91
KGT.11	47.09	94.19
KGT.12	48.95	97.90
KGT.13	47.34	94.69
KGT.14	46.97	93.95
KGT.15	49.97	99.95
KGT.16	49.32	98.64
Original Chitosan	16.43	32.85

The modified chitosan No. KGT.15 was synthesized to be used as an absorbent when the appropriate conditions for Cr (VI) removal were determined using the results.

3.1.2. Effect of pH on Cr(VI) Removal

pH is one of the important parameters affecting the adsorption capacity due to its influence on the surface properties of adsorbent and metal ionization. The results of experiments conveyed at different pH levels are shown in Fig.1.

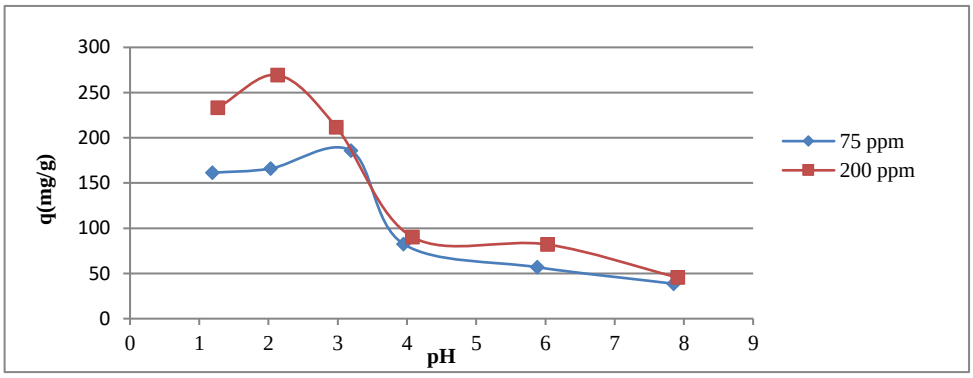

Figure 1.Determination of the appropriate pH range for adsorption of Cr (VI) ions on modified chitosan; t = 24 hours, T = 293 K

3.1.3 Effect of Contact Time on Cr(VI) Removal

The effect of contact time was examined in the range of 1h to 24 h for 70 and 160 ppm initial Cr(VI) concentrations, and the results are shown in Figure 2.

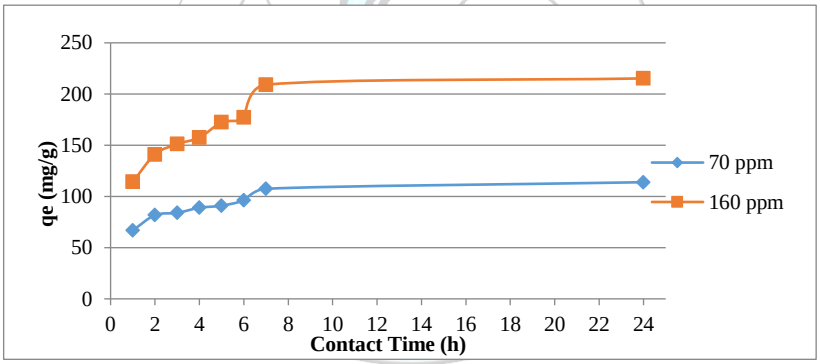

Figure 2. Determination of the equilibrium time of adsorption of Cr (VI) ions on modified chitosan; t = 24 hours, m = 0.03 g T = 293 K.

Figure 2 shows that the duration of the equilibrium is independent in the initial concentration. It was observed that the amount of retention increased at negligible level after the first seven hours. For this reason, it can be said that the seven hour contact period of Cr (VI) ions is sufficient for adsorption with modified chitosan.

3.1.4. Effect of Absorbent Dose on Cr(VI) Removal

Determination of the appropriate adsorbent dose is important for the efficiency and cost of the adsorption process. In the experiments, the effects on adsorption were investigated by changing the adsorbed dose at two different initial concentrations.The effect of the adsorbent dose on the amount of retention and percentages of removal is shown in Table 3 and Table 4.

Table 3. The effect of the adsorbent dose on the amount of retention and percentages of removal at C_0= 100 ppm

Adsoebent Dose (g/50mL)	Amount of Retention (mg/g)	Removal Percentages (%)
0.03	126.4	75.83
0.04	114.3	91.41
0.05	98.0	97.96
0.07	69.8	97.59
0.10	49.8	99.44
0.15	33.3	99.81
0.20	25.0	99.94

Table 4. The effect of the adsorbent dose on the amount of retention and percentages of removal at C_0= 250 ppm.

Adsoebent Dose (g/50mL)	Amount of Retention (mg/g)	Removal Percentages (%)
0.03	227.2	54.52
0.04	203.9	65.25
0.05	172.1	68.86
0.07	145.0	81.23
0.10	112.7	90.13
0.15	79.9	95.82
0.20	62.4	99.93

The difference between the percentages of removal increases with each step from 0.01 g to 0.07 g to the adsorbent dose. It is seen that the difference between the percentages of elimination in adsorbent dose increases after 0.07 g is negligible. It has been decided that the appropriate adsorbent dose should be between 0.07 g / 50 mL and 0.1 g / 50 mL.

3.2. Adsorption Isotherm Studies

As a result of the studies, the optimum environment conditions for hexavalent chromium removal from waste water with modified chitosan were determined as solution pH 1-3, adsorbent dose 1.4 (g / L) and contact time 7 hours. After selection of optimal operating conditions, isotherm studies were conducted to characterize the adsorption of Cr(VI) upon modified chitosan. It was studied with different initial concentrations at constant temperature to obtain isotherm graphs. Relationship between the adsorbate concentration of the equilibrium solution and the amount of adsorbent

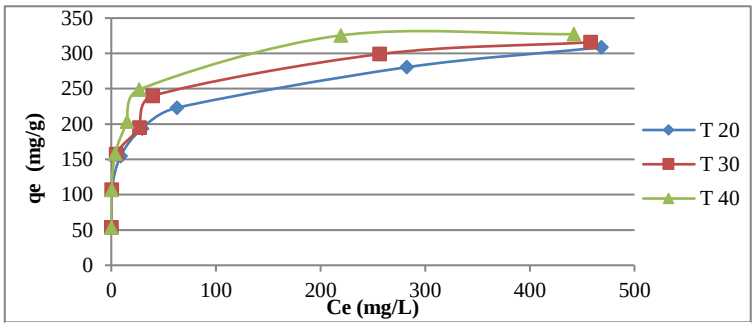

Figure 3: Determination of adsorption capacities at different temperatures; (C0) = 75, 150, 225, 300, 375, 675, 900 ppm.

material per unit adsorbent should be established. It should be determined again by changing the temperature to determine the effect of the change with temperature. For this purpose, five different

initial concentrations and three different temperatures were used. The relationship between the amount of retention and the concentration of solution in equilibrium is shown in Figure 3.

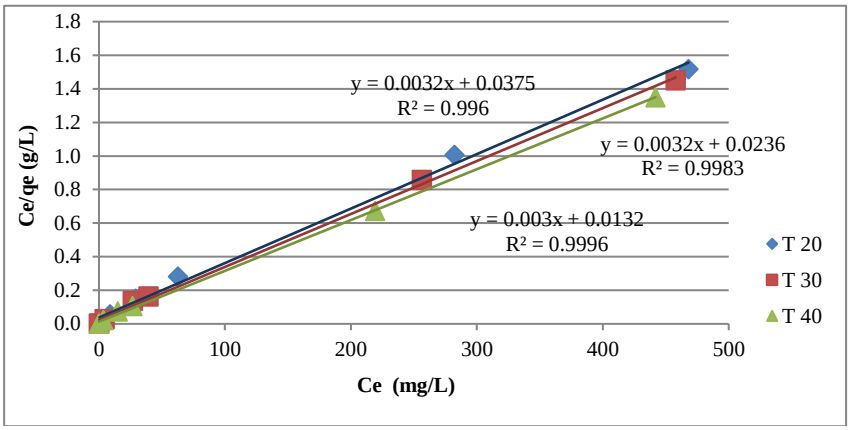

Figure 4. Langmuir constants for different temperatures in the adsorption of Cr (VI) ions with modified chitosan

To determine whether the obtained data correspond to Langmuir isotherms, a graph of C_e / q_e values versus C_e values was drawn. This is shown in Figure 4.

The correlation constant in the three different temperatures being greater than 0.96 indicates that the Langmuir isotherm is suitable for characterizing the adsorption of the Cr (VI) ions with the modified chitosan. Data were fitted to linearized forms of isotherm models and results are given in Table 5.

Table 5. Langmuir Constant

Sıcaklık	Sabitler				
	K_L (L/g)	a_L (L/mg)	q_m (mg/g)	R^2	Dağılma sabiti R_L
293	26.66	0.085	308.4	0.996	0.012
303	42.37	0.135	315.7	0.998	0.008
313	75.75	0.227	327.2	0.999	0.004

3.3. Characterization of Chitosan and Modified Chitosan

3.3.1. X-Ray Diffraction Analysis

X-ray diffraction of the original chitosan and modified chitosan is shown in Figures 5 and 6.

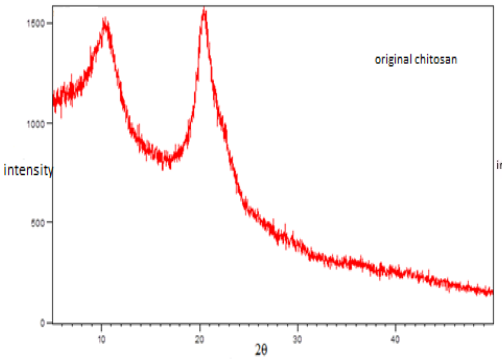

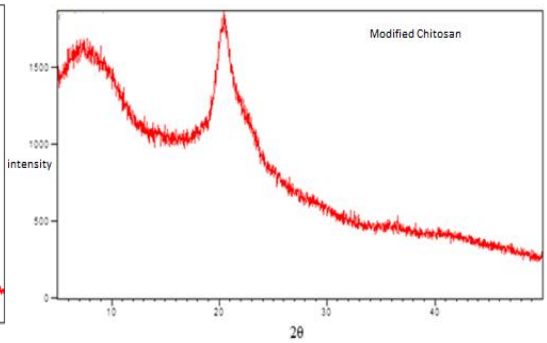

Figure 5. Original chitosan XRD pattern *Figure 6. Modified chitosan XRD pattern*

XRD analysis was also made for the proof of modification. The modification of chitosan with glutaraldehyde and thiourea showed a peak flattening at 11 ° with the resultant original chitosan, indicating a significant decrease in crystallinity as a result of chitosan cross-linking with

glutaraldehyde. The crystallinity of the chitosan polymer may play a limiting role in metal retention capacity. The crystallinity parameter of chitosan is an important parameter of accessibility to the inner region for both water and metal ions. Many studies have shown that reducing the crystallinity results in an improvement in metal ion retention properties [14,15].

3.3.2.Thermal Gravimetric Analysis of Adsorbents

Figure 7 shows the mass change graph due to the temperature obtained at 25 - 1000 ºC temperature by Thermal Gravimetric Analysis (TGA) method of chitosan and modified chitosan. In order to examine the thermal behavior of chitosan and modified chitosan in detail, differential thermogravimetric (DTG) curves of the materials are given in Figure 8.

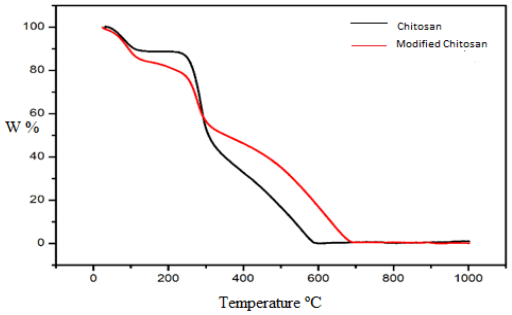

Figure 7. Chitosan and Modified Chitosan TGA Curve

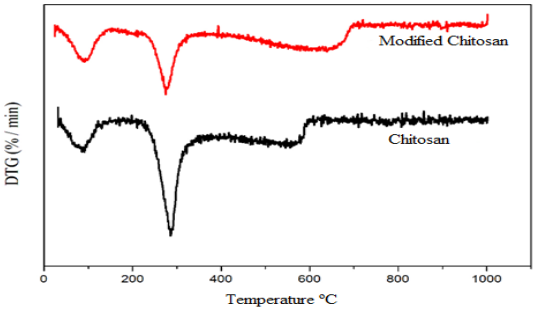

Figure 8. Chitosan and Modified Chitosan DTG Curve

Both samples showed mass loss at 100 ºC, while at the same time DTG curves both peaks at 100 ° C on both samples. When studies done in the literature are examined, the initial weight loss at about 100 ° C is due to the evaporation of water. The other weight loss at 200-500 ºC is due to the deterioration of the structure of the chitosan molecule [16]. Thermal gravimetric analysis gives information on the composition of chitosan and modified chitosan. On the other hand, information about the connections between the chitosan and the modified chitosan was needed. For this reason, analysis with XRD and FTIR and study with TGA was supported.

3.3.3.FTIR Analysis of Adsorbents

The chemical structures of the chitosan and modified chitosan and the changes in the functional groups of the compounds were investigated by FT-IR spectroscopy and the peak intensities were interpreted in accordance with the literature. The FTIR spectra of the original chitosan and modified chitosan are given in Figure 9.

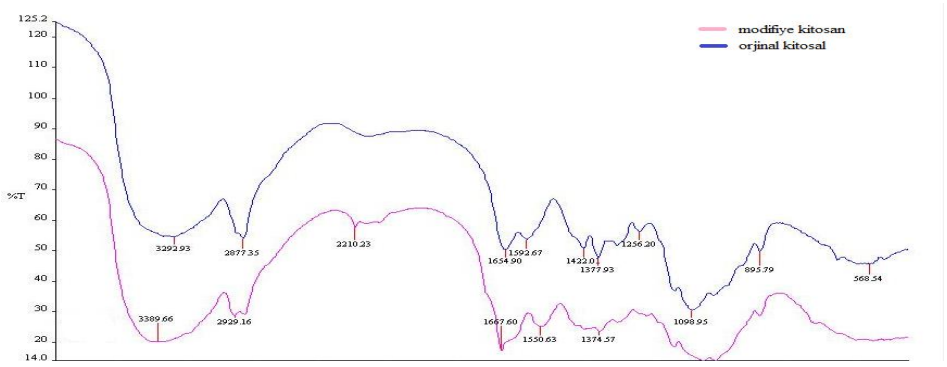

Figure 9. Original chitosan and modified chitosan FTIR spectrum.

The disappearance of the NH_2 band in the cross-linked chitosan as a consequence of the cross-linking mechanism with gulataldehyde at 560 cm^{-1} in the original chitosan is evidence of the cross-linking of chitosan [16].

4. CONCLUSIONS

In this work, chitosan was first modified with glutaraldehyde and thiourea. The modified chitosan showed better performance in chrome removal compared to the original chitosan. The effects of different experimental conditions on the adsorption process were investigated by studying different solution pH, temperature, initial concentration, contact time and adsorbent dose. As a result of the studies, the optimum environment conditions for hexavalent chromium removal from waste water with modified chitosan were determined as solution pH 1-3, adsorbed dose 1.4 (g / L) and contact time 7 hours. Langmuir isotherm has been identified as the most suitable isotherm. Chitosan and modified chitosan are characterized by XRD, FTIR and thermal gravimetric analysis.

5. REFERENCES

[1]. Özdede, A., ‘‘Investigation of removal conditions of some heavy metals from aqueous solutions using polypyrrole / chitosan composite polymer.’’, Graduate thesis, Dumlupınar University Institute of Science, Kütahya, 2013.
[2]. Acar, F. N.Malkoc, E. ‘‘The removal of chromium (vı) from aqueous solutions by fagus orientalis’’ Bioresource Technology, 94, 13-15, 2014.
[3]. Kumar, P. A., Ray, M., Chakraborty, S. ‘‘Hexavalent chromium removal from wastewater using aniline formaldehyde condensate coated silica gel.’’ *Journal of Hazardous Materials*, 143, 24-32, 2007.
[4]. Water Pollution Regulation Control Regulation, Official Gazette, Ankara, 1988.
[5]. Babel, S., Kurniawan, T. A. ‘‘Low-cost adsorbents for heavy metals up-take from contaminated water: a review,’’ Journal of Hazardous Materials, 97, 219-243,2013.
[6]. Crini, G., Badot, P. M. ‘‘Application of chitosan, a natural aminopoly-saccharide, for dye removal from aqueous solutions by adsorption processes using batch studies: a review of recent literature,’’ Progress in Polymer Science, 33, 399-447, 2008.
[7]. Khan, T. A., Peh, K. K., Chng, H. S. ‘‘Reporting degree of deacetylation values of chitosan: the influence of analytical methods,’’ J. Pharm Pharmaceut Sci, 5, 205-212, 2002.
[8]. He, C., Yang, Z., Ding, J., Chen, Y., Tong, X., Li, Y. ‘‘Effective removal of Cr(VI) from aqueous solution by 3-aminopropyltriethoxysilane- functionalized graphene oxide. colloids and surfaces a: physicochemical and Engineering Aspects’’, 520, 448-458, 2017.
[9]. Erdoğan, Y. A.‘‘Arsenic removal from various wastewaters with various adsorbents’’, Ph.D. thesis, ITU Institute of Science and Technology, Istanbul, 2015.
[10]. Guibal, E., Sweeney, N. V. O., Vincent, T., Tobin, J. M.,‘‘Sulphur derivatives of chitosan for palladium sorption, Reactive and Functional Polymers’’ 50, 149-163,2002.
[11]. Sıvri, N. ‘‘Hexavalent chromium removal from waste water in fixed bed examination’’. Master thesis, ITU Institute of Science and Technology, Istanbul.2015.
[12]. Abdullah, M. A., Chiang, L., Nadeem, M. ‘‘Comparative evaluation of adsorption kinetics and isotherms of a natural product removal by amberlite polymeric adsorbents’’, Chemical Engineering Journal, 146, 370-376.2009.
[13]. Monteiro, O. A., Airoldi, C. ‘‘Some studies of crosslinking chitosan–glutaraldehyde interaction in a homogeneous system,’’ International Journal of Biological Macromolecules, 26, 119-128.1999.
[14]. Sankararamakrishnan, N., & Sanghi, R. ‘‘Preparation and characterization of a novel xanthated chitosan’’., Carbohydrate Polymers, 66, 160-167. 2006.
[15]. Farmer, S., Selda, Ö. Z. E. K., Aksoy, S. A., Aksoy, K., & Fethiye, G. Ö. D. E., ‘‘Nanocrystalline PVA / chitosan nanofiber synthesis and characterization’’ SDU Science Magazine, 10.2015.
[16]. Çulcu. L.‘‘Investigation of adsorption of cyanide blue 62 used in textile industry on crosslinked chitosan’, Master thesis, Institute of Science and Technology, Istanbul.2015.

Journal Homepage : http://dergipark.gov.tr/ejens
EJENS
European Journal of Engineering and Natural Sciences
CODEN: EJENS
DergiPark AKADEMİK

Kinetics of Granulated Waste Tyre Pyrolysis via Thermogravimetry and Model-Free Methods

Peter T. Cherop[1]*, Sammy L. Kiambi[1], Paul Musonge[1]
[1]*Durban University of Technology, Department of Chemical Engineering, P.O Box 1334, Durban 4000, South Africa..*
**Corresponding Author email: tumwet2@gmail.com*

Abstract

There has been an increase in global consumption of waste tyres over the years. However only a portion of the total amount of waste tyres can be recycled or reused for other applications. Land-filling has been considered an alternative to address the problem of continued waste tyres accumulation, but huge space is needed for this and the reusable resources are wasted. This therefore has led to environmental and economic problem of disposal of the large mass of waste tyres. Waste tyre pyrolysis, which is the thermal decomposition in absence of oxygen, can be used to recover both energy and material. Thermogravimetric analysis (TGA) is the technique commonly used to evaluate the weight loss kinetics associated with the vaporisation of materials during pyrolysis. The purpose of this study was to establish the kinetics of thermal degradation of waste tyres by TGA and to compare the activation energies (E) obtained using two model-free methods. The experiments were carried out in a nitrogen environment and a temperature range of 20°C to 600°C at three heating rates. Results show that the pyrolysis process of the tyre crumb occurs in three stages as the various components of the tyre undergo decomposition. A mean activation energy of approximately 232 kJmol^{-1} was obtained using the two models.

Key words

Waste tyre, activation energy, thermal degradation, model-free.

1. INTRODUCTION

The amount of waste tyres dumped all over the world is roughly 1.5 billion [1], but only 15-20 % is reused whereas the remaining percentage is simply dumped into the earth [2]. The valorisation of waste plastics and tyres plays a big role in the reduction in fossil fuel consumption and helps to address the issue of climate change [3]. Due to the high calorific value of waste tyres (33-35 MJkg-1), recovery of energy is considered an alternative to recycle them [4]. Pyrolysis, which is the process of thermal degradation in absence of oxygen, can be potentially involved to recover energy from waste tyres. During pyrolysis, the organic volatile matter in the tyres is transformed into low-molecular weight products, whereas the inorganic constituents, are retained as solid residue [5].

Tyres are made up of more than 100 different substances such as rubber, steel, silica gel, carbon black etc. During tyre production, the rubbers commonly used are natural rubber (NR), butadiene rubber (BR),) and styrene-butadiene rubber (SBR).The degradation of these components occurs at different temperature ranges. The thermal degradation behaviour of waste tyres depends on the type of rubber as well as its contents [6, 7].

The study of kinetics of waste tyre pyrolysis has recently been an area of interest since understanding of kinetics of this process is important in the design and optimisation of industrial scale waste tyre recycling units. Model-free and model-fitting methods are commonly used to determine the kinetic parameters during solids decomposition [8-10].

The following expression is commonly used for thermal degradation of solids:

$$\frac{d\alpha}{dt} = k(T).f(\alpha) \tag{1}$$

where α is the degree of conversion, $k(T)$ the reaction rate constant, and $\frac{d\alpha}{dt}$ the conversion rate over time. The conversion degree, α is determined as:

$$\alpha = \frac{w_0 - w_t}{w_0 - w_f} \tag{2}$$

where w_0 is the initial weight of the sample, w_t the weight of the sample at a given temperature, and w_f the final mass of the sample.$k(T)$ is expressed according to Arrhenius law as :

$$k(T) = A.exp^{-\frac{E}{RT}} \tag{3}$$

where E is the activation energy, R the gas constant, and A the pre-exponential factor.Combining equations (1) and (3) yields:

$$\frac{d\alpha}{dt} = A\,.\,e^{-\frac{E_a}{RT}}.f(\alpha) \tag{4}$$

Equation (5) is the underlying equation used in determination of kinetic parameters in non-isothermal degradation of solid materials.

$$g(\alpha) = \int_0^{\alpha} \frac{d\alpha}{f(\alpha)} = \frac{A}{\beta}.\int_{T_0}^{T}.e^{-\frac{E}{RT}}\,dT \tag{5}$$

where $g(\alpha)$ is the conversion integral function.

The Friedman (FR) method [11] is one of the iso-conversional methods used to calculate the activation energy. The expression for FR equation is:

$$ln\left(\frac{d\alpha}{dt}\right) = Ln\left[\beta\left(\frac{d\alpha}{dT}\right)_{\alpha,i}\right] = Ln(A_\alpha) + Ln[\,f(\alpha)] - \frac{E_\alpha}{RT_{\alpha,i}} \tag{6}$$

where E_α and A_α represent the activation energy and pre-exponential factor at a specific conversion degree respectively. The slope in the plot of $Ln\left[\beta\left(\frac{d\alpha}{dT}\right)_{\alpha,i}\right]$ against $\frac{1}{T_{,i}}$ yields the activation energy. The Kissinger-Akahira-Sunose (KAS) method [12, 13] is expressed as folows:

$$ln\left(\frac{\beta}{T^2}\right) = ln\left(\frac{AE_a}{R\,g(\alpha)}\right) - \frac{E_a}{RT} \tag{7}$$

where the plot of $ln\left(\frac{\beta}{T^2}\right)$ versus $\frac{1}{T}$ gives a straight line. The slope from this plot is then used to determine the E

The aim of this study was to establish the non-isothermal kinetics of pyrolysis of waste tyres by applying two model-free methods to the TG/DTG data in order to determine the activation energies. The models used were KAS and FR.

2. MATERIALS AND METHODS

Tyre crumb from Mathe group, South Africa was used during this study. The elemental analysis of the tyre crumb was done using vario EL cube elemental analyser, while the thermogravimetric analysis was carried out in a Differential Scanning Calorimeter – Thermo Gravimetric Analyser SDT Q600. The tyre crumb samples were heated from 20°C to 600°C at three different heating rates in nitrogen (100 $mLmin^{-1}$) environment to prevent oxidation of the samples. Three heating rates of 2°C, 5°C, and 10°C min^{-1} were used to establish the behaviour of thermal degradation of the tyre crumb, while the TA Instruments software was used to extract the data that aided to plot the TG and DTG curves.

3. RESULTS AND DISCUSSION

3.1. Elemental Analysis

The elemental analysis results showed that the carbon content in the tyre crumb was 83.54 wt. % while the hydrogen content was 7.55 wt.%.The contents of nitrogen and sulphur were 0.35 wt.% and 1.84 wt.% respectively whereas the oxygen content (calculated by difference) was 6.73 wt.%.

3.2. Thermal Degradation of the Tyre Crumb

The TG/DTG thermograms of the tyre crumb thermal degradation for the heating rates of 2, 5 °C , and 10 °C min^{-1} are shown in Figures 1,2, and 3 respectively.

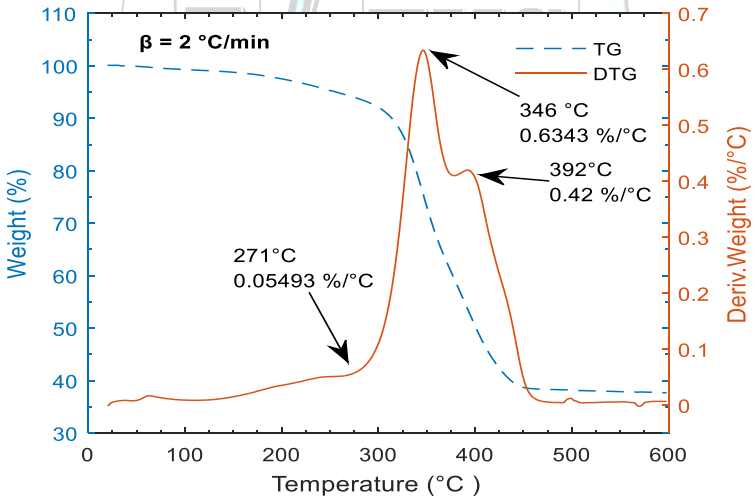

Figure 1.TG/DTG thermogram at 2 °C/min

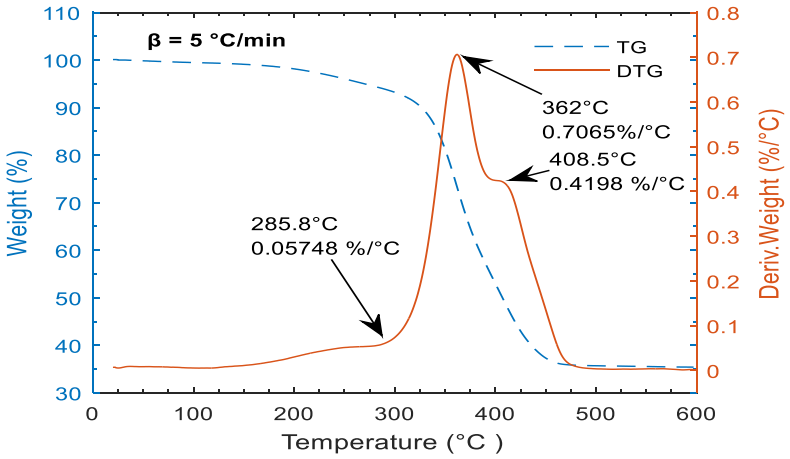

Figure 2. TG/DTG thermogram at 5 °C/min

The thermal decomposition started at about 270 °C and 285 °C and was complete at about 460 °C and 480 °C for the heating rates of 2 and 5 °C min^{-1} respectively. At the heating rate of 10 °C min^{-1}, the decomposition started at about 290 °C and was complete at about 495 °C. There was no further weight loss above the temperature of 500 °C for the three heating rates. Three stages of decomposition are notable from the peaks seen in the DTG curves i.e. removal of lubricants and oil in the waste tyre with a mean temperature peak value of about T_m = 285 °C, breakdown of NR with T_m = 367 °C and breakdown of BR and SBR with T_m = 411.0 °C. The TG/DTG thermograms indicate that the temperature peaks increase as the heating rates increase during the three-stage thermal degradation process.

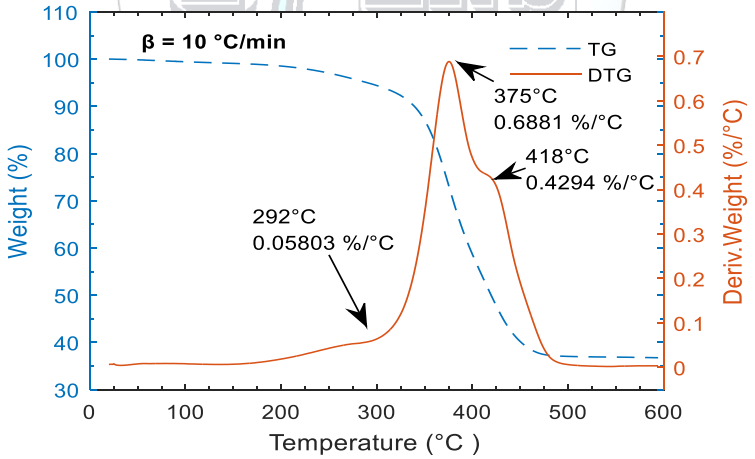

Figure 3. TG/DTG thermogram at 10 °C/min

3.3. Non-isothermal Kinetics of Tyre Degradation

The KAS and FR models were used to determine the activation energies. The two models aided to establish the relationship between the conversion degree and the activation energies. Using KAS model, the plot of $ln\left(\frac{\beta}{T^2}\right)$ against $\frac{1}{T}$ gave a slope of $-\frac{E}{R}$, from which the activation energy was determined while the plot of $ln\left(\frac{d\alpha}{dt}\right)$ versus $\frac{1}{T}$ was used to determine the activation energies by the FR model. The kinetic plots of tyre crumb thermal degradation using the two models are shown in Figures 4 and 5.

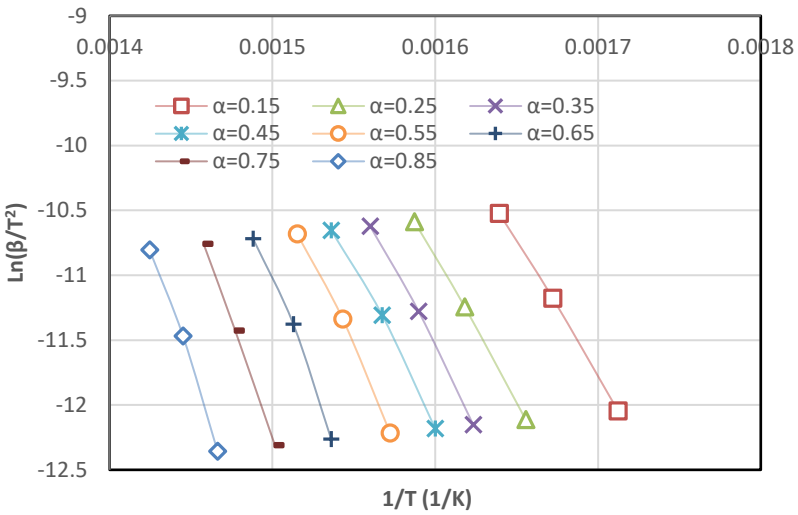

Figure 4. KAS plot at various conversion degrees

The degrees of conversion considered using the KAS and FR models ranged between 0.15 - 0.85. Figure 6 shows the variation of activation energy with conversion degree for the two models. The relationship between the activation energies obtained from KAS and FR models at same conversion degrees is shown in Figure 7. In both models, the activation energy increases with conversion degree up to α = 0.45 where the activation energy drops (Figure 6).The trend of increasing activation energy with conversion degree then continues without any further fluctuation. The mean activation energies obtained using KAS and FR models were 231.76 $kJmol^{-1}$ and 231.92 $kJmol^{-1}$ respectively. This clearly shows that the values obtained from the two models are similar and it indicates that the models used can accurately predict the non-isothermal thermal degradation of the tyre crumb. The similarity in E values from KAS and FR models is further justified by the linear relationship (Figure 7) between the E values from the two methods. The regression coefficient values obtained from the plots using the two models were high. The lowest R^2 values using the KAS and FR methods were 0.9895 and 0.9903 respectively while the highest values were 0.9998 and 0.9999.This indicates the thermogravimetric data fit well into the models used.

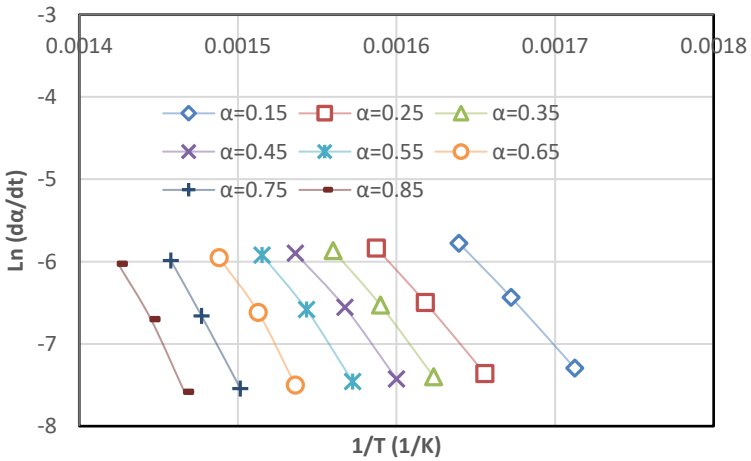

Figure 5. FR plot at various conversion degrees

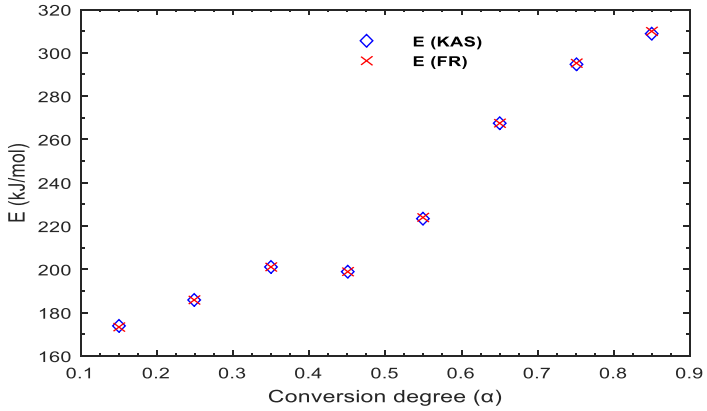

Figure 6. Activation energy versus conversion degree

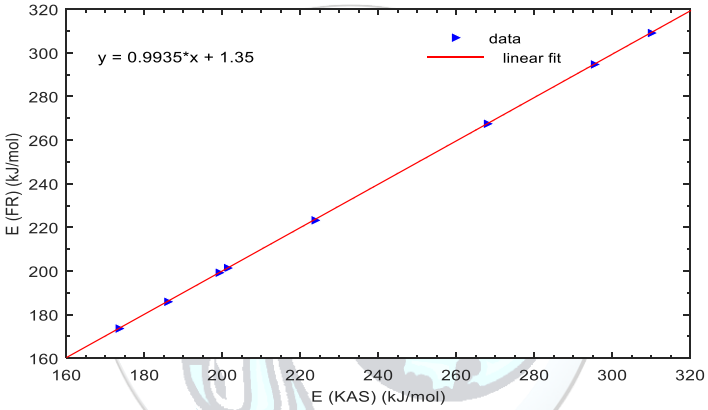

Figure 7. E_{FR} versus E_{KAS}

4. CONCLUSION

This study aimed to establish the thermal degradation process of the tyre crumb by applying two model-free methods to the thermogravimetric analysis data. The thermogravimetric analysis was carried out at heating rates of 2°C, 5°C, and 10°C min^{-1} in presence of nitrogen. Results show that the pyrolysis process of the tyre crumb takes place in three stages as the various components of the tyre undergo decomposition. The activation energy generally increases with increasing conversion degree in the early stages of thermal degradation. There is, however, a slight drop in activation energy at $\alpha = 0.45$, after which the trend of increasing activation energy with conversion degree continues. A mean activation energy of approximately 232 $kJmol^{-1}$ was obtained using the KAS and FR models, an indication that the values from the two models are similar. The data obtained from this kinetic study could play a big role in the optimisation of the design of industrial scale waste tyre pyrolysis units.

ACKNOWLEDGEMENTS

The first author appreciates the financial support of South Africa's National Research Fund (NRF) towards the Doctoral Fellowship.

REFERENCES

[1] Y. Su and B. Zhao, "Pyrolysis of waste tire powder and its comparison with Shenhua coal," in *Energy and Environment Technology, 2009. ICEET'09. International Conference on*, 2009, pp. 262-265.

[2] Y. Su and W. Deng, "A thermogravimetric study of waste tire powder," in *E-Product E-Service and E-Entertainment (ICEEE), 2010 International Conference on*, 2010, pp. 1-4.

[3] G. Lopez, R. Aguado, M. Olazar, M. Arabiourrutia, and J. Bilbao, "Kinetics of scrap tyre pyrolysis under vacuum conditions," *Waste Management,* vol. 29, pp. 2649-2655, 2009.

[4] F. A. López, T. A. Centeno, F. J. Alguacil, and B. Lobato, "Distillation of granulated scrap tires in a pilot plant," *Journal of Hazardous Materials,* vol. 190, pp. 285-292, 2011.

[5] I. de Marco Rodriguez, M. F. Laresgoiti, M. A. Cabrero, A. Torres, M. J. Chomón, and B. Caballero, "Pyrolysis of scrap tyres," *Fuel Processing Technology,* vol. 72, pp. 9-22, 2001.

[6] D. Y. C. Leung and C. L. Wang, "Kinetic study of scrap tyre pyrolysis and combustion," *Journal of Analytical and Applied Pyrolysis,* vol. 45, pp. 153-169, 1998.

[7] S. Seidelt, M. Müller-Hagedorn, and H. Bockhorn, "Description of tire pyrolysis by thermal degradation behaviour of main components," *Journal of Analytical and Applied Pyrolysis,* vol. 75, pp. 11-18, 2006.

[8] A. Anca-Couce, A. Berger, and N. Zobel, "How to determine consistent biomass pyrolysis kinetics in a parallel reaction scheme," *Fuel,* vol. 123, pp. 230-240, 2014.

[9] S. Vyazovkin and D. Dollimore, "Linear and nonlinear procedures in isoconversional computations of the activation energy of nonisothermal reactions in solids," *Journal of chemical information and computer sciences,* vol. 36, pp. 42-45, 1996.

[10] É. de Godois Baroni, K. Tannous, Y. J. Rueda-Ordóñez, and L. K. Tinoco-Navarro, "The applicability of isoconversional models in estimating the kinetic parameters of biomass pyrolysis," *Journal of Thermal Analysis and Calorimetry,* vol. 123, pp. 909-917, 2016.

[11] H. L. Friedman, "Kinetics of thermal degradation of char-forming plastics from thermogravimetry. Application to a phenolic plastic," in *Journal of Polymer Science: Polymer Symposia*, 1964, pp. 183-195.

[12] H. E. Kissinger, "Reaction kinetics in differential thermal analysis," *Analytical chemistry,* vol. 29, pp. 1702-1706, 1957.

[13] T. Akahira and T. Sunose, "Joint convention of four electrical institutes," *Res Rep Chiba Inst Technol,* vol. 16, pp. 22-31, 1971.

Journal Homepage : http://dergipark.gov.tr/ejens
EJENS
European Journal of Engineering and Natural Sciences
CODEN: EJENS
DergiPark AKADEMİK

Wastewater Treatment by Floating Macrophytes (*Salvinia Natans*) Under Algerian Semi-Arid Climate

Ayache Laabassi[1]* and Asma Boudehane[1]

[1]*Department of Ecology and Environment, Faculty of Natural and Life Sciences, University of Batna2, Algeria.*

**Corresponding Author email: laabassiayache@gmail.com*

Abstract

Macrophyte pond has developed strongly in the field of wastewater treatment for irrigation in rural areas and small communities. Their association allows, in some cases, to increase the hydraulic capacity while maintaining the highest level of quality.

The present work is devoted to the treatment of domestic wastewater under climatic conditions of Algeria (semi-arid) through a system using two tanks planted with *Salvinia natans*.

The performance study and treatment efficiency of the system overall shows that the latter provides a significant removal of nitrogen pollution: total Kjeldahl nitrogen NTK (85.2%), Ammonium NH_4^+-N (79%), Nitrite NO_2^--N (40%) also, a major meaningful reduction of biochemical oxygen demand BOD_5 was observed at the output of the system (96.9 %). As BOD_5, the chemical oxygen demand (COD) removal was higher than 95 % at the exit of the two tanks. A moderately low yield of phosphate-phosphorus (PO_4^{3-}-P) was achieved with values not exceeding 37 %. In general, the quality of treated effluent meets the Algerian standard of discharge and which allows us to select a suitable species in constructed wetland treatment systems under semi-arid climate.

Key words

Nutrient removal, Salvinia natans, semi-arid climate, Wastewater treatment

INTRODUCTION

In most countries of the world, there has been growing and irreversible interest of the public for the protection of the environment. In Algeria, for instance, the water pollution problem is quite serious and therefore, purification techniques including constructed wetlands (CWs) using macrophytes are currently widely used for treatment of wastewater. CWs become an interesting alternative for the treatment of wastewater, seen the great benefits that they exhibit, they are less expensive to build and operate, are constructed directly on the wastewater discharge site, require little mechanized equipment and ultimately are less sensitive to changes in pollutant loads [1].

The main functions of CWs include surface water storage, holding and recycling nutrients, providing wildlife habitats, stabilizing shorelines, controlling and buffering storm related flooding, recharging groundwater,

providing treatment for pollutants in water [2]. Furthermore, CWs can effectively remove organic matter, suspended solids, metals, and excess nutrients (such as nitrogen, phosphorus, etc.) through various processes including filtration, sedimentation, biological and microbiological adsorption, and assimilation [3].

Macrophyte-based wetland systems (MBWS) are reported to be effective for the treatment of primary, secondary and tertiary urban wastewater, domestic, stormwater, agricultural and industrial wastewater [4, 2, 5], however, the challenge is to maximize efficiency the lowest possible cost [6]. The choice of plants is an important issue in

the filters planted with macrophytes because they have to survive the potential toxic effects of sewage and their variability. The use of local plants with economic and environmental interests in the sewage systemmakes them more exciting.

Aquatic plants, emergent or free floating, acquire more and more importance in the world especially in countries with hot climates where the photosynthetic efficiency is important. The produced biomass is valued using biomethanation or by incorporation in animal nutrition [7]. Floating or emergent aquatic plants, such as water hyacinth (*Eichhornia crassipes* (Mart) Solms), water lettuce (*Pistia stratiotes L.*), *Salvinia natans* (L.), cattail (*Typha latifolia L.*), bulrush (*Scirpus validu .L.*), are able to treat wastewater with high purification yields [8, 9, 10].

2. MATERIALS AND METHODS

2.1. Experimental device and methods

The experiment was carried out under semi-arid conditions at the town of Merouana (35°37'43''N, 05°54'42'E) located 500 km East of Algiers (Fig. 1), which has a semi-arid to arid Mediterranean climate with an average rainfall of about 240mm per year and an average temperature of about 5 to 38°C. The experimental device used for the present study depicted in Figure 2. Thre biofiltration unit, comprised two tanks of 75 liters capacity (50 cm(L) x 50 cm(W) x 60 cm(H)). The tanks are filled to 5 cm in depth and 30 cm with respectively gravel (5-10mm) and soil with silty clay-sandy texture (31% clay, 20% silt and 49% sand). The tanks were planted with *S. natans* (36.5 g per tank).

The systems supplied by raw domestic wastewater (25 liters/day) acquired from Merouana municipal sewage treatment works, and Table 1 summarizes its physicochemical characteristics. Tanks inclined at 10° to the surface such that water can be directly downstream, and fitted with a drain at the bottom for percolating water collection (effluent). Wastewater passes from a tank to another through a 4-cm (outside diameter) perforated PVC pipe. The experiment lasted eight months from April to November 2015.

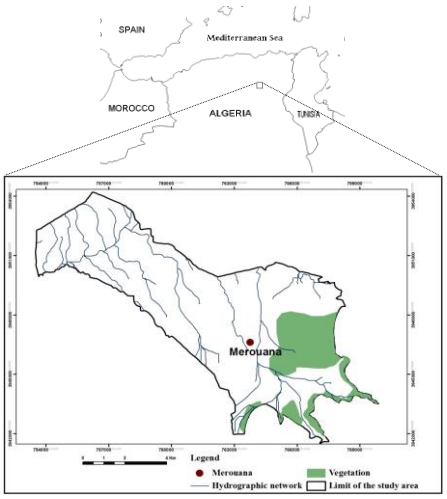

Figure 1. Location map of analyzed area.

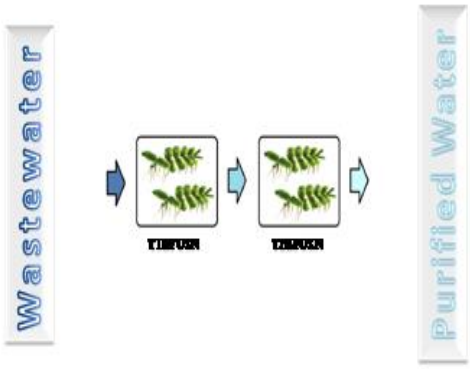

Figure 2. Macrophyte-biofiltration system used for wastewater treatment. T1 BFUSN, T2 BFUSN(Tanks 1 and 2 of second biofiltration unit planted with Salvinia natans).

.2.2. Wastewater quality monitoring and statistical analyses

The CWs placed in operation in April 2015. Their removal efficiency and treatment performance evaluated in eight sampling campaigns, which took place in the eight-month period from April to November 2014.

Wastewater samples (influent and effluent) were collected and stored in glass bottles, transported to the laboratory and analyzed immediately for biochemical oxygen demand (BOD_5), chemical oxygen demand (COD), total Kjeldahl nitrogen
(TKN), nitrate-nitrogen (NO_3-N), nitrite-nitrogen (NO_2-N), ammonium-nitrogen (NH_4-N) and phosphate–phosphorus (PO_4-P) according to French standard methods [11]. In addition, measurement of temperature (T) and pH had done using a portable instrument (ProfiLine pH 3110, WTW). We used at least five repetitions of each sample to achieve sufficient accuracy.
Treatment efficiency of chemical parameters was calculated as the percentage of removal for N and P as follows:

Removal efficiency (%) = $\left(\frac{Ci-Ce}{Ci}\right) x\ 100$, where Ci and Ce are the influent and effluent concentrations in mg/L.

Data analyzed using one-way ANOVA and least significant difference tests (LSD at alpha = 0.05) to find differences among means of the different physicochemical parameters of wastewater before and after treatment. Statistical analyses carried out using STATGRAPHICS Centurion XV (Manugistics, Rockville, MD, USA)

3. RESULTS AND DISCUSSION

Constructed wetlands (CWs) using macrophytes are currently widely used for treatment of wastewater. In order to investigate whether the CWs using emergent macrophyes (EM) and floating macrophytes (FM) were effective for the treatment of domestic wastewater, we carried out the present study the aquatic plant species, namely *S. natans* an FM

Overall, our results indicate that the biofiltration system (FM) is highly effective in the treatment of domestic wastewater (Tables 1, 2 and Fig. 3a-i).

3.1. Mean physicochemical parameter variation

Table 1 summarizes results of the measured physicochemical proprieties of wastewater before and after biofiltration treatment. Figure 3, however, displays the seasonal variation of all these parameters throughout the eight-month period of experience. In contrast to the mean values of the wastewater temperature, which showed only slight spatial variations along the biofiltration unit and generally ranged from 18.2 to 24.6ºC depending on the season (Fig. 3a), all the studied parameters were showed a significant variation after wastewater biofiltration (Table 1).

As revealed by Figure 3b, the mean pH value of input water used in this study was 7.2 and ranged from 7 to 7.5. However, at the outlet of biofiltration units, the pH values were ranging from 7.1 to 8.3. This decrease in pH values was statistically significant ($P<0.01$).

In contrast to the slight decrease observed in the mean values of wastewater temperature at the outlet the biofiltration unit, can be explained by the fact that water surface was fully hedged by *S.natans* (Fig. 3a and Table 1), the mean values of pH were significantly increased (Table 1). Similar results observed in previous studies [12- 13]. Both decrease in temperature and increase in pH can be explained by the algal growth observed at the surface of each tank since foliar cover may preserves the tank surface against summer drying and offer shade to bacteria and the fact that algae can absorb CO_2 faster than it can be replaced by bacterial respiration [12].

3.2. Pollutant removal efficiency

Table 2 presents the variation of mean removal efficiency along the various biofiltration unit for all the pollutants. Overall, we calculate the removal for each constituent based on its concentrations at the inlet and outlet of the biofiltration unit. As displayed by Table 2, with the exception of nitrate (NO_3-N), the biofiltration system exhibited high percentages of removal efficiency of nitrogen from wastewater namely in term of NH_4-N, and TKN.

Regarding nitrogen pollution, our results indicate high average removal efficiencies of the biofiltration system, particularly for ammonium (NH_4-N) and TKN. Consistent with this, in aquatic ecosystems, the decrease in NH_4-N content was usually explained by the transformation of NH_4-N into NO_3-N (the so-called nitrification), which is favored by aerobic conditions, plus a subsequent denitrification [14]. Another possible way is volatilization as NH_3, which is inducible by the increase of pH [15]. Under natural growth conditions, NH_4-N is probably the main N source preferred for most aquatic macrophytes as revealed by results of numerous studies [16-17].

Table 1. *Physicochemical parameter and pollutant concentration statistics*

		INLET	OUTLET BFUSN	F	LSD5%
pH	Mean	7.18 (c)	7.41 (bc)	5.50**	0.29
	SD	0.17	0.23		
	Min	7.0	7.1		
	Max	7.5	7.75		
T °C	Mean	21.13 (a)	19.94 (ab)	1.63 n.s	n.s
	SD	2.25	2.10		
	Min	18.2	17.3		
	Max	24.6	23.3		
NH_4-N	Mean	64.36 (a)	13.38 (bc)	264.3***	5.51
	SD	8.46	2.29		
	Min	51.84	10.42		
	Max	76.18	16.46		
NO_3-N	Mean	2.43 (b)	3.61 (b)	25.77***	10.11
	SD	0.93	2.32		
	Min	1.4	1.0		
	Max	3.9	6.9		
NO_2-N	Mean	0.128 (a)	0.083 (ab)	3.73*	0.056
	SD	0.05	0.06		
	Min	0.08	0.02		
	Max	0.20	0.22		
TKN	Mean	102.4 (a)	15.84 (b)	97.43***	86.52
	SD	22.81	11.01		
	Min	69.6	6.40		
	Max	131.3	40.1		
PO_4-P	Mean	10.95 (a)	6.86 (b)	10.66***	3.85
	SD	1.47	1.90		
	Min	8.9	5.1		
	Max	13.2	11.1		
BOD_5	Mean	311.3 (a)	8.31 (b)	43.7***	302.07
	SD	129.7	3.65		
	Min	112.4	4.2		
	Max	466.1	15.5		
COD	Mean	981.7 (a)	40.56 (b)	209.08***	935.64
	SD	171.4	4.47		
	Min	683.5	33.2		
	Max	1230.1	47.1		

Table 2. Removal efficiency (%) of different nutriments for the three units

		BFUSN	F	LSD5%
NH_4-N	Mean	79.0 (a)	18.18***	3.45
NO_3-N	Mean	17.1 (a)	n.s	n.s
NO_2-N	Mean	40.0 (a)	n.s	n.s
TKN	Mean	85.2 (a)	4.32*	7.75
PO_4-N	Mean	36.9 (a)	n.s	n.s
BOD_5	Mean	96.9 (a)	n.s	n.s
COD	Mean	95.7 (a)	5.04*	1.25

*, **, *** indicate significant differences at P<0.05, 0.01 and 0.001 respectively. n.s, not significant. Different small letters mean significant differences (P < 0.05) among treatments.

The lower removal of NO_3-N in the outlet water compared to wastewater, on some individual occasions, bear witness to the great nitrifying activity. In agreement, aquatic macrophytes have well-developed internal air spaces (aerenchyma) throughout the plant tissues that ensures the transfer of oxygen to the roots and rhizomes [18]. The oxygen that diffuses through the roots stimulates growth of nitrifying bacteria in the rhizosphere [19]. In general, the positive removal efficiencies of BFUSN can probably due to macrophytes uptake [20] and/or the process of denitrification [21].

Nitrite concentrations of the inflow and the outflow are of secondary importance for the evaluation of the overall annual nitrogen removal of the wetland [22]. In general, the low outflow concentrations (< 1mg/L) been brought about by nitrification of NH_4-N to NO_3-N and NO_2-N at aerobic plant roots, with subsequent rapid denitrification to the atmosphere in the anaerobic parts of the substrate or is immobilized by plant uptake, adsorption, and precipitation [23].

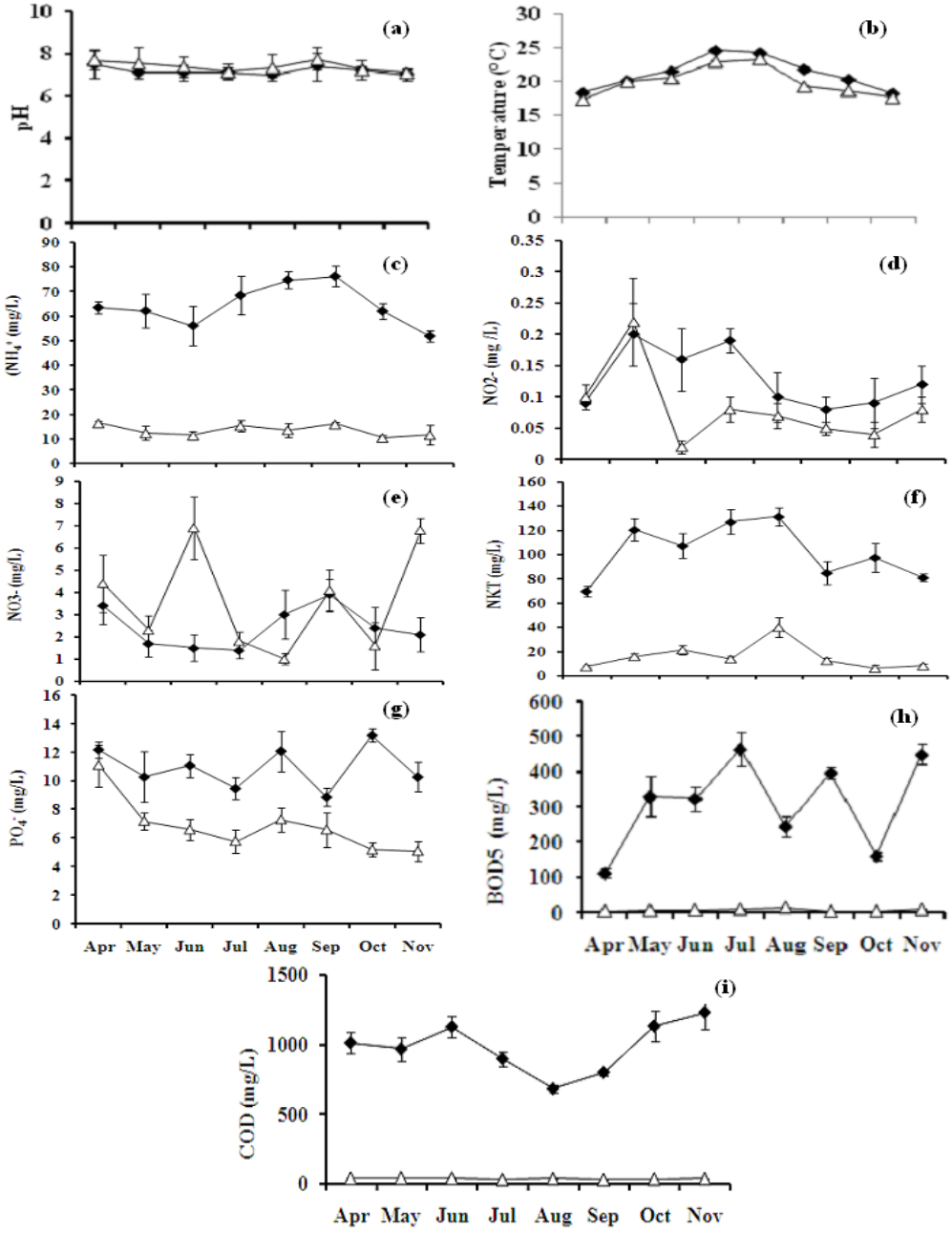

Figure 3. Time-course of change in Temperature (a), pH (b), NH_4-N (c), NO_2-N (d), NO_3-N (e), TKN (f), PO_4-P (g), BOD_5 (h), COD (i) throughout the period of study (Mean ± SD).

The high levels of TKN removal efficiencies in all the treatments are probably due to macrophytes that play a major role in eliminating TKN through nitrification, metabolism, and storage processes [24, 25, 26]. TKN removal efficiency increases with increase in pH [27-28].

In addition, it appears from the same figure that the concentration of the main forms of nitrogen (NH_4-N, NO_3-N and TKN) and PO_4-P as well as BOD_5 and COD in wastewater showed highly significant decreases ($P<0.001$) after biofiltration (Table 1 and Fig. 3).

Table 2 also showed the variation in removal of orthophosphate from the wastewater in the various experimental devices. Overall, there is no significant difference in the removal efficiency of PO_4-P among the biofiltration unit. The efficiencies of removal in BFUSN increase by 09-60.6% with an overall average of 36.9%. It is worth noting that even though PO_4-P concentrations increased in the outlet waters on some individual occasions.

The moderately high level of phosphorus monitored as orthophosphate (PO_4-P) could be due to direct use of PO_4-P by plants [29] or attributed to adsorption on the soil particles and precipitation reactions [30]. However, it also added that release of orthophosphate and clogging of the system could explain this low average reduction.

The average concentrations and overall efficiency elimination of BOD_5 in the influent and effluent throughout the study period displayed in Figure 3h and Table 2 respectively. The removal of BOD_5 found higher (96.9 %).

Otherwise, the higher reduction of BOD_5 can be attributed to several mechanisms (physical and biological processes) including sedimentation and filtration associated with settleable solids or filterable material, in addition to oxidation mainly by aerobic bacteria (protozoa, rotifers, etc.) attached to plant roots [31].

The load of domestic wastewater chemical oxygen demand (COD) fluctuates greatly between 683.5 mg/L and 1230.1 mg/L with a mean value of 981.7 mg/L. Thus, at the outlet of the three units follows fluctuations in domestic wastewater with significant picks (Fig. 3i). Overall, compared to domestic wastewater, the treated wastewater quality is significantly better. The removal rates of COD (95.7 %).

Like BOD_5, COD reduction is almost entirely due to physical processes such as filtration and adsorption rather than biological processes associated with the microbial community or with the plants [32]. These findings are in agreement with some studies reported in the literature, which found better COD removal whether using floating macrophytes [33-28].

4. Conclusion

This work provides an opportunity to highlight the potential of floating plants (*S. natans*) to treat the domestic wastewater under semi-arid conditions. Overall, our result indicates that the bioinfiltration unit provide a significant removal of the organic (BOD_5, COD) and inorganic (TKN, NH_4-N and PO_4-P) pollutants from domestic wastewater. The effluent quality was lower than the Algerian standards related to effluent quality for agricultural reuse purposes, therefore, it is possible to reuse the treated wastewater for restricted irrigation and can be environmentally friendly. The good results given by *S. natans* (rare plant) involve its use in wastewater treatment in order to preserve this kind of plants. Finally, the use of this kind of biofiltration system for the treatment of other types of water pollution (e.g. microorganisms and heavy-metal pollution) is required.

REFERENCES

[1].**H. Brix,** Do macrophytes play a role in constructed treatment wetlands? *Water Science and Technology*, 35 (5), 11–17, 1997

[2].**S. R. Jing, Y. F. Lin, D. Y. Lee, T. W. Wang,** Using constructed wetland systems to remove solids from highly polluted river water. *Water Science & Technology: Water Supply*, 1(1), 89-96, 2001.

[3].**J. Josimov-Dunđerski, A. Belić, M. Jarak, L. Nicolić, M. Rajić, A. Bezdan,** Constructed Wetland – The Serbian Experience. *Carpathian Journal of Earth and Environmental Sciences*, 7, 2, 101–110, 2012.

[4].**I. Galfati, E. Bilal, A. Beji Sassi, H. Abdallah, A. Zaier,** Accumulation of heavy metals in native plants growing near the phosphate treatment industry, Tunisia. *Carpathian Journal of Earth and Environmental Sciences*, 6, 2, 85–100, 2011.

[5].**I.U. Khan, N.U. Khan, M.Q. Khan, M.J. Khan, M.J. Khan, H.U. Rahman,** Phyto-Extraction Of Municipal Wastewater's And Applied Solution Of Copper, Lead And Zinc, Using High Bio-Mass Crops, Zea Mays And Brassica Napus. *Carpathian Journal of Earth and Environmental Sciences*, 9, 1, 107–116, 2014.

[6]. **Y. Zimmels, F. Krizhner, A. Malkovskaja,** *Application* and features of cascade aquatic plants systems for sewage treatment. *Ecological Engineering*, 34, 147–161, 2008.

[7].**R.D. Sooknah, A.C. Wilkie,** Nutrient remo val by floating aquatic macrophytes cultured in anaerobically digested flushed dairy manure wastewater. Ecological Engineering, 22, 27–42 (2004).

[8].**K.R. Reddy, K.L. Campell , D.A. Graetz, K.M. Portier,** Use of biological filters for treating agricultural drainage effluents. *Journal of Environmental Quality*, 11, 591–595, 1982.

[9].**A. Jampeetong, H. Brix,**. Nitrogen nutrition of Salvinia natans: Effects of inorganic nitrogen form on growth, morphology, nitrate reductase activity and uptake kinetics of ammonium and nitrate. *Aquatic Botany*, 90, 67–73, 2009a.

[10]. **J. Vymazal,** Horizontal sub-surface flow and hybrid constructed wetlands systems for wastewater treatment. *Ecological Engineering*, 25(5), 478–90, 2005.

[11]. **AFNOR.** *Qualité de l'eau—Recueil, normes et réglementation*. In: Edition DRSIPHC628.161/QUA, editor, 2008.

[12]. **Y.F. Lin, S.R. Jing, T.W. Wang, D.Y. Lee,** 2002. Effects of macrophytes and external carbon sources on nitrate removal from groundwater in constructed wetlands. *Environmental Pollution*, 119, 420–423, 2002.

[13]. **J. Coleman, K. Hench, K. Garbutt, A. Sexstone, G. Bissonnette, J. Skousen,** Treatment of domestic wastewater by three plant species in constructed wetlands. *Water, Air and Soil Pollution*, 128, 283–295, 2001.

[14]. **R.H. Kadlec, R.L. Knight,** *Treatment Wetlands***.** Lewis. Boca Raton, p. 893, 1996.

[15]. **K.R. Reddy, D.L. Sutton,** Water hyacinths for water quality improvement and biomass production. *Journal of Environmental Quality*, 13, 1–8, 1984.

[16]. **A. Jampeetong, H. Brix,** Effects of NH_4^+ concentration on growth, morphology and NH_4^+ uptake kinetics of Salvinia natans. *Ecological Engineering*, 35, 695–702, 2009b.

[17]. **Y.Y. Fang, O. Babourina, Z. Rengel, X.E. Yang, P.M. Pu,** Ammonium and nitrate uptake by the floating plant Landoltia punctata. *Annals of Botany*, 99, 365–370, 2007.

[18]. **M. Abissy, L., Mandi,** Comparative study of wastewater purification efficiencies of two emergent helophytes: Typha latifolia and Juncus subulatus under arid climate. *Water Science and Technology*, 39 (10–11), 123–126, 1999.

[19]. **H.M. Zhang, X.L. Wang, J.N. Xiao, F.L. Yang, J. Zhang,** Enhanced biological nutrient removal using MUCT-MBR system. *Bioresource Technology*, 100, 1048-1054, 2009.

[20]. **F.E. Matheson, M.L. Nguyen, A.B. Cooper , T.P. Burt, D.C. Bull,** Fate of ^{15}N-nitrate in unplanted, planted and harvested riparian wetland soil microcosms. *Ecological Engineering*, 19, 249–264, 2002.

[21]. **S.P. Faulkner, C.J. Richardson,** *Physical and chemical characteristics of freshwater wetland soils*. In: Hammer, D.A. (Ed.), Constructed Wetlands for Waste Water Treatment. Municipal, Industrial and Agricultural. Lewis Publishers Inc., Chelsea, MI, 1989.

[22]. **P. Kuschk, A. Wiebner, U. Kappelmeyer, E. Weißbrodt, M. Kästner, U. Stottmeister,** Annual cycle of nitrogen removal by a pilot-scale subsurface horizontal flow constructed wetland under moderate climate. *Water Research*, 37, 4236-4242, 2003.

[23]. **G. Shalla, K. John, R. Paul, M. Angus,** The nutrient assimilative capacity of maerl as a substrate in constructed wetland systems for waste treatment. *Water Research*, 34, 2183–2190, 2000.

[24]. **R-Y. Wang, N. Korboulewsky, P. Prudent, V. Baldy, G. Bonin,** Can verticalflow wetland systems treat high concentrated sludge from a food industry? A mesocosm experiment testing three plant species. *Ecological Engineering*, 35,230–237, 2009.

[25]. **G. Maltais-Landry, F. Chazarenc, Y. Comeau, S. J. Brisson,** Effects of artificial aeration, macrophyte species and loading rate on removal efficiency in constructed wetland mesocosms treating fish farm wastewater. *Journal of Environmental Engineering and Science*, 6, 409–414, 2007.

[26]. **J. García,, E. Ojeda, E. Sales, F. Chico, T. Piriz, P. Aguirre, R. Mujeriego,** Spatial variations of temperature, redox potential, and contaminants in horizontal flow reed beds. *Ecological Engineering*, 21, 129–142, 2003.

[27]. **E.J. Olguín, D. Rodríguez, G. Sánchez, E. Hernández, M.E. Ramírez,** Productivity, protein content and nutrient removal from anaerobic effluents of coffee wastewater in Salvinia minima ponds, under subtropical conditions. *Acta Biotechnologica*, 23, 259–270, 2003.

[28]. **G.S. Mishra, A. Mitra, R. Banerjee, M.M. Ghangrekar,** Comparative pretreatment method for efficient enzymatic hydrolysis of Salvinia cucullata and sewage treatment in ponds containing this biomass. Clean Technologies and Environmental Policy, 16, 1787-1794 (2013)

[29]. **O. Urbanc-Berčič, A. Gaberščik,** The relationship of the processes in the rhizosphere of common reed Phragmites australis (Cav.) Trin. ex Steudel to water fluctuation. *International Review of Hydrobiology*, 89, 500–507, 2004.

[30]. **S.C. Reed, R.W. Crites, E.J. Middlebrooks,** *Natural Systems for Waste Management and Treatment.* Second ed. McGraw-Hill Inc., New York (1995)

[31]. **K.R. Reddy, W.F. DeBusk,** *Nutrient storage capabilities of aquatic and wetland plants*.In: Reddy K.R. and W.H. Smith, editors.Aquatic plants for water treatment and resource recovery.Orlando, Florida: Magnolia Publishing. p. 337–353, 1987.

[32]. M.P. Ciria, M.L., Solano, P. Soriano, Role of macrophyte Typha latifolia in a constructed wetland for wastewater treatment and assessment of its potential as a biomass fuel. Biosystems Engineer-ing, 92(4), 535-544 (2005)

[33]. M. Kumari, B.D. Tripathi, Effect of aeration and mixed culture of Eichhornia crassipes and Salvinia natans on removal of wastewater pollutants. *Ecological Engineering*, 62, 48– 53, 2014.

Journal Homepage: http://dergipark.gov.tr/ejens

EJENS
European Journal of Engineering and Natural Sciences

DergiPark AKADEMİK

CODEN: EJENS

Generation of a Multi-Layered Diffusion Coating on an Interstitial-Free Steel

Fikri Erdem Şeşen*, Omer Serdar Özgen

Istanbul Technical University, Faculty of Chemistry-Metallurgy, Department of Metallurgical and Materials Engineering, 34469, Istanbul, Turkey

Corresponding Author email: sesen@itu.edu.tr

Publication Info

Abstract

Boronizing and titanium diffusion were applied to an interstitial-free steel substrate separately and one after another. Boronizing was carried out in a liquid environment by applying an electric current, but titanium diffusion was performed in a closed chamber containing solid chemicals. The generated single-layered and multi-layered diffusion coatings were characterised by utilising an optical microscope, a scanning electron microscope equipped with an energy dispersive spectrometer, and a Vickers microhardness tester. Phase analysis was carried out by an x rays diffractometer. Some chemical reactions were supposed to occur regarding titanium diffusion process and the standard formation enthalpies of these reactions were calculated by using a database. Microstructural investigations revealed that titanium diffusion was able to be applied after boronizing, causing the formation of a titanium based diffusion layer over the previously generated boride layer. On the other hand, when a titanium diffused substrate was boronized, the titanium based diffusion layer acted as a diffusion barrier to the introduced boron atoms, preventing the formation of a boride layer. However, if boronizing duration and the current density applied during boronizing were increased to a certain degree, boron atoms could surpass this barrier in small quantities and form small discontinuous regions. It was observed that the hardness of a phase which was formed within the titanium based diffusion layer was more than 4000 HV in some regions when titanium diffusion was applied after boronizing. The standard formation enthalpies of the six assumed chemical reactions were negative, indicating that these can occur at 1000 °C at which titanium diffusion was applied. Moreover, most of the products of these reactions were detected in x rays diffraction analyses.

Key words

Boronizing, Interstitial-free steel, Titanium diffusion

1. INTRODUCTION

Surface modification techniques in several types are applied to steels in order to improve their hardness, mechanical strength, corrosion resistivity, resistivity to high temperature, etc. A group of these surface modification techniques involves the formation of an outer protective layer while another group is applied by diffusing an element through the cross-section of the substrate in a certain depth. The increase of the thickness is negligible in treatments related to diffusion. Boronizing (boron diffusion) is a type of latter-mentioned group of techniques. Boronizing is performed by diffusing elemental boron on to the substrate surrounded by a boronizing agent (source) which can be in solid, liquid, gaseous or even plasma state. Boronizing can be applied to almost all types of steels, titanium alloys and refractory metal alloys [1], [2].

Elemental titanium can be applied on to steel surface either as a protective coating or by diffusion. Titanium diffusion is generally performed before or after another surface treatment or as an intermediate stage between two different treatments [3].

Interstitial-free steel is a special type of steel possessing very little amount of alloying elements. Interstitials (carbon and nitrogen) are removed from solid solution through precipitation hardening. It is extensively used in cases where high ductility is desired [4].

This study aimed to investigate the resultant microstructure, phases and hardness that are achieved via boronizing and titanium diffusion applied separately or one after another. Moreover, some chemical reactions were introduced related to titanium diffusion process by the help of the x rays diffraction analysis results and the standard formation enthalpies of these reactions were calculated by using a database.

2. EXPERIMENTAL PROCEDURE

2.1. Samples

An interstitial-free steel was used as the substrate material. The chemical composition of the interstitial-free steel is given in Table 1. The steel plates were obtained after cold-rolling during the intermediate stages of the production held at Eregli Iron and Steel Works Co. (ERDEMİR) in Zonguldak, Turkey. The steel plates, having a thickness of 4 mm, were cut in to 50×23 mm dimensions and their surfaces were ground in order to eliminate any undesired matter before the diffusion coating processes.

Table 1. Chemical composition of the interstitial-free steel substrate

Element	C	Si	Mn	P	S	Cr	Ni	Mo	Al	Ti	V	B
wt. %	0.0088	0.0110	0.2130	0.0136	0.0089	0.0250	0.0470	0.0010	0.0286	0.0597	0.0083	0.0004

2.2. Diffusion Coating Processes

Boronizing was performed electrothermochemically in a bath containing 100% dehydrated sodium borax which was melt in a chamotte crucible placed in a pit-type furnace which was heated to 900 °C. An electric current having a density of 0.10 or 0.40 A/cm^2 was applied during boronizing which lasted 45 or 120 minutes.

Titanium diffusion was carried out thermochemically in a one-use closed cylindrical chamber that contained micro-sized titanium particles, ammonium chloride and aluminium oxide. The chamber was heated in an electric-resistant furnace to 1000 °C and kept at this temperature for 2 hours. After that, it was left to cool down to room temperature.

2.3. Characterisation

Microstructural investigation was done by using an Olympus GX71 Optical Microscope and a Jeol JSM-7000F Field Emission Scanning Electron Microscope equipped with an energy dispersive spectrometer. The samples were metallographically prepared in a standard manner before the

examinations. They were chemically etched with Nital3 solution before the optical investigations while coated with platinum and painted with silver chloride to be prepared for scanning electron microscope work. The phase analysis was carried out by utilising a Philips Pan Analytical X'Pert Professional type x rays diffractometer supplying CuKα radiation. The scanning was performed between 20 and 90 2θ values at a rate of 1° per min. The peaks on the patterns were identified manually by matching the related d values with the ones in the relevant indexes. A Future Tech FM 500 hardness tester was used in order to evaluate the hardness of the generated diffusion layers. A 50 gF load was applied for a dwelling time of 10 seconds. The standard formation enthalpies of the chemical reactions introduced about titanium diffusion process were calculated by using database HSC Chemistry Software v 6.12.

3. EXPERIMENTAL RESULTS

3.1. Results of Microstructural Investigations

A scanning electron microscope image showing the surface of the interstitial-free steel boronized at 900 °C for 45 minutes by applying a current density of 0.10 A/cm^2 is given in Figure 1. The stable boride phases of Fe_2B and FeB are visualised clearly in the image. Semi-quantitative chemical analysis values detected in the selected regions on the scanning electron microscope image are given in Table 2 in weight per cent.

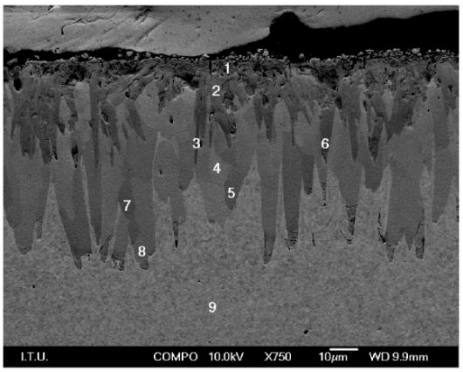

Figure 1. Scanning electron microscope image showing the surface of the interstitial-free steel boronized at 900 °C for 45 min by applying a current density of 0.10 A/cm^2

Table 2. Semi-quantitative weight per cent chemical analysis values detected in the selected regions numbered between 1 and 9

Region	1	2	3	4	5	6	7	8	9
B% wt.	17.50	18.22	18.94	11.69	9.97	18.48	10.70	9.73	-
Fe% wt.	82.50	81.78	81.06	88.31	90.03	81.52	89.30	90.27	98.95
C% wt.	-	-	-	-	-	-	-	-	1.05

Another scanning electron microscope image showing the surface of the titanium diffused interstitial-free steel is given in Figure 2. Semi-quantitative chemical analysis values detected in the selected regions on the scanning electron microscope image are given in Table 3 in weight per cent.

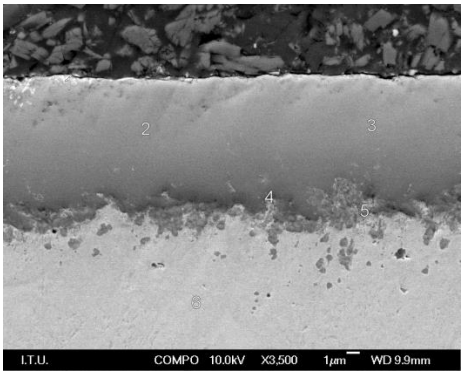

Figure 2. Scanning electron microscope image showing the surface of the interstitial-free steel titanium diffused at 1000 °C for 2 hours

Table 3. Semi-quantitative weight per cent chemical analysis values detected in the selected regions numbered between 1 and 6

Region	1	2	3	4	5	6
Al% wt.	7.08	1.30	-	2.85	2.32	-
Ti% wt.	46.88	98.70	100.00	72.03	71.53	-
Fe% wt.	46.05	-	-	25.12	26.15	100.00

The surface of the interstitial-free steel first boronized at 900 °C for 45 minutes by applying a current density of 0.10 A/cm^2 and then titanium diffused at 1000 °C for 2 hours can be viewed in another scanning electron microscope image given in Figure 3. Semi-quantitative chemical analysis values detected in the selected regions on the scanning electron microscope image are given in Table 4 in weight per cent.

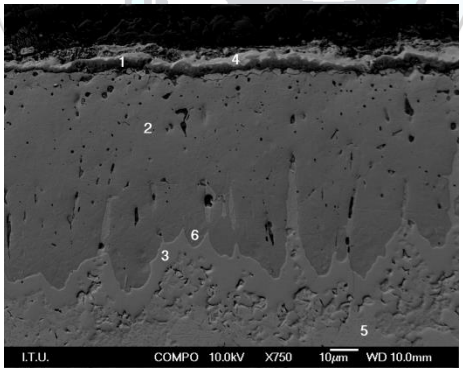

Figure 3. Scanning electron microscope image showing the surface of the interstitial-free steel first boronized at 900 °C for 45 min by applying a current density of 0.10 A/cm^2 and then titanium diffused at 1000 °C for 2 hours

Table 4. Semi-quantitative weight per cent chemical analysis values detected in the selected regions numbered between 1 and 6

Region	B% wt.	O% wt.	Al% wt.	Si% wt.	S% wt.	Ca% wt.	Ti% wt.	Mn% wt.	Fe% wt.	Ni% wt.
1	-	23.56	11.08	-	0.29	-	54.07	-	11.00	
2	6.70	-	-	-	-	-	-	2.32	90.99	
3	-	-	-	-	-	-	-	2.24	97.76	
4	-	6.19	2.44	0.92	-	1.21	72.98	-	7.45	8.80
5	-	-	-	-	-	-	-	1.92	98.08	
6	-	-	-	-	-	-	-	2.75	97.25	

The outer layer of the surface of the interstitial-free steel first boronized and then titanium diffused, by applying the above-mentioned parameters, can be visualised in more detail in the scanning electron microscope image given in Figure 4. Semi-quantitative chemical analysis values detected in the selected regions on the scanning electron microscope image are given in Table 5 in weight per cent.

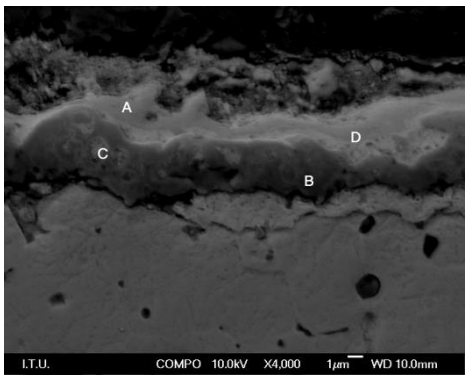

Figure 4. Scanning electron microscope image focusing on the outer surface (titanium based diffusion layer) of the interstitial-free steel first boronized at 900 °C for 45 minutes by applying a current density of 0.10 A/cm^2 and then titanium diffused at 1000 °C for 2 hours

Table 5. Semi-quantitative weight per cent chemical analysis values detected in the selected regions named A-D

Region	B% wt.	O% wt.	Al% wt.	Si% wt.	P% wt.	Ca% wt.	Ti% wt.	Fe% wt.	Ni% wt.
A	-	10.90	5.79	0.95	-	1.94	69.69	6.83	3.89
B	23.61	-	2.98	-	-	-	59.85	13.56	-
C	-	-	-	-	22.44	-	33.52	36.44	7.44
D	-	5.59	4.13	1.05	-	0.99	65.91	10.52	11.81

Another optical micrograph presenting the microstructure of the surface of the interstitial-free steel which was first titanium diffused at the above-mentioned parameters and then boronized at 900 °C for 45 minutes by applying a current density of 0.10 A/cm^2 is given in Figure 5. As can be seen in the micrograph, boronizing could not be accomplished after titanium diffusion.

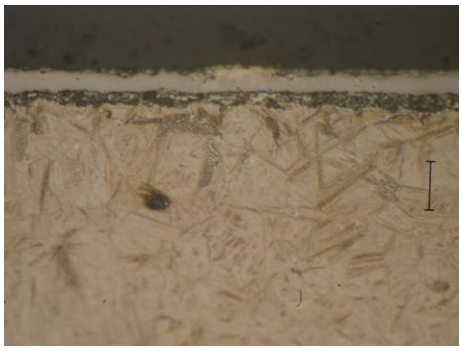

Figure 5. Optical micrograph showing the surface of the interstitial-free steel first titanium diffused at 1000 °C for 2 hours and then boronized at 900 °C for 45 min by applying a current density of 0.10 A/cm^2 (Scale length: 10 µm)

The inhibiting effect of titanium based diffusion layer is visualised more clearly in Figure 6 where an optical migrograph showing two different surfaces of the interstitial-free steel which was first titanium diffused, then one surface cropped and finally boronized is given.

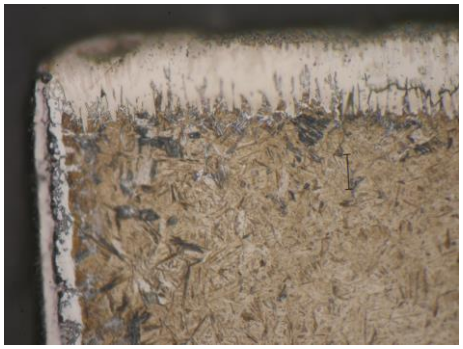

Figure 6. Optical micrograph of the interstitial-free steel showing the horizontal surface which was only boronized and the vertical surface which was first titanium diffused and then boronized (Scale length: 20 µm)

When the boronizing duration and the current density applied during boronizing carried out after titanium diffusion were increased to a certain degree, boron atoms were able to surpass the already generated titanium based diffusion layer. This phenomenon is visualised in an optical micrograph given in Figure 7 and a scanning electron microscope image given in Figure 8. Semi-quantitative chemical analysis values detected in the selected regions on the scanning electron microscope image are given in Table 6 in weight per cent.

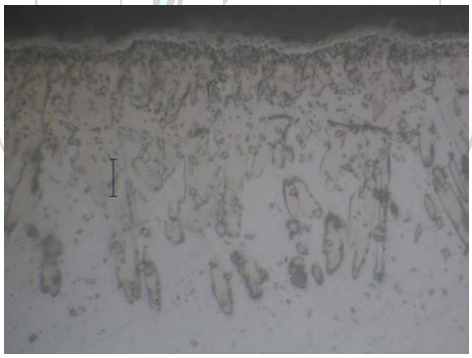

Figure 7. Optical micrograph of the surface of the interstitial-free steel titanium diffused at 1000 °C for 2 hours and then boronized at 900 °C for 120 min by applying a current density of 0.40 A/cm^2 (Scale length: 10 µm)

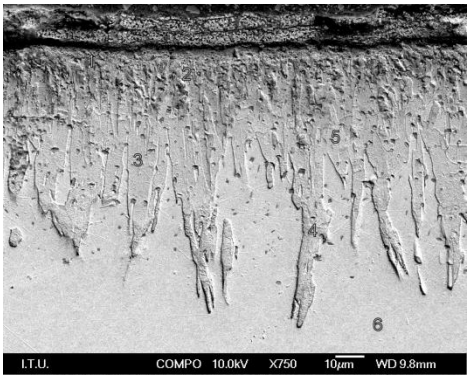

Figure 8. Scanning electron microscope image of the surface of the interstitial-free steel first titanium diffused at 1000 °C for 2 hours and then boronized at 900 °C for 120 min by applying a current density of 0.40 A/cm^2

Table 6. Semi-quantitative weight per cent chemical analysis values detected in the selected regions numbered between 1 and 6

Region	1	2	3	4	5	6
B% wt.	31.22	2.11	-	-	-	-
Al% wt.	0.51	-	-	0.29	0.38	-
Ti% wt.	48.13	0.34	0.20	0.56	0.37	-
Fe% wt.	20.15	97.55	99.80	99.16	99.25	100.00

3.2. Results of X Rays Diffraction Analyses

The pattern of the x rays diffraction analysis, obtained by scanning the diffusion layer formed on the surface of the interstitial-free steel that was boronized at 900 °C for 45 minutes by applying a current density of 0.10 A/cm^2, is shown in Figure 9. Stable boride phases of Fe_2B and FeB were detected on the scan as well as a metastable boride phase of Fe_3B. The pattern of the x rays diffraction analysis, obtained by scanning the diffusion layer formed on the surface of the interstitial-free steel that was titanium diffused at 1000 °C for 2 hours, is given in Figure 10. Phases of titanium iron, iron nitride and titanium nitride were detected in the scan in different stoichiometric ratios. The pattern of the x rays diffraction analysis, obtained by scanning the diffusion layer formed on the surface of the interstitial-free steel that was first boronized at 900 °C for 45 minutes by applying a current density of 0.10 A/cm^2 and then titanium diffused at 1000 °C for 2 hours, is presented in Figure 11. Stable boride phases of Fe_2B and FeB, iron nitride, titanium iron, titanium nitride and boron nitride were detected in the scan. Finally, the pattern of the x rays diffraction analysis, obtained by scanning the diffusion layer formed on the surface of the interstitial-free steel that was first titanium diffused at 1000 °C for 2 hours and then boronized at 900 °C for 120 minutes by applying a current density of 0.40 A/cm^2, is given in Figure 12. Stable boride phases of Fe_2B and FeB, metastable boride phase of Fe_3B, boron nitride, titanium diboride, titanium nitride and iron nitride in three different stoichiometric ratios were detected in the scan.

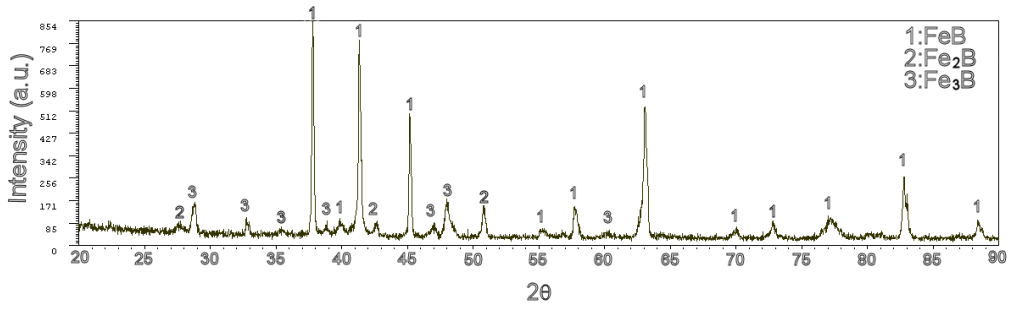

Figure 9. X rays diffraction pattern of the surface of the interstitial-free steel boronized at 900 °C for 45 min by applying a current density of 0.10 A/cm^2

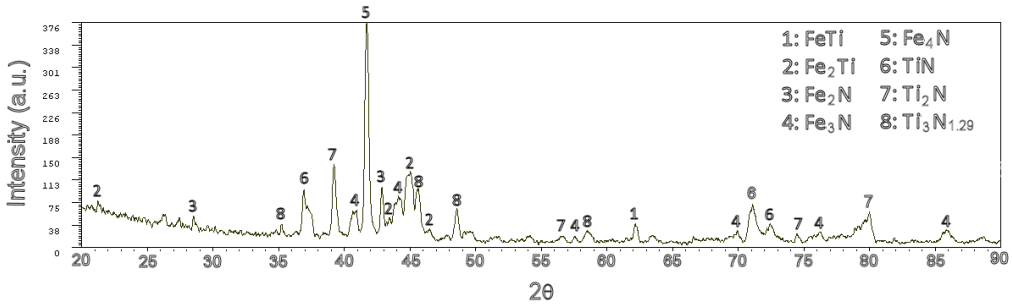

Figure 10. X rays diffraction pattern of the surface of the interstitial-free steel titanium diffused at 1000 °C for 2 hours

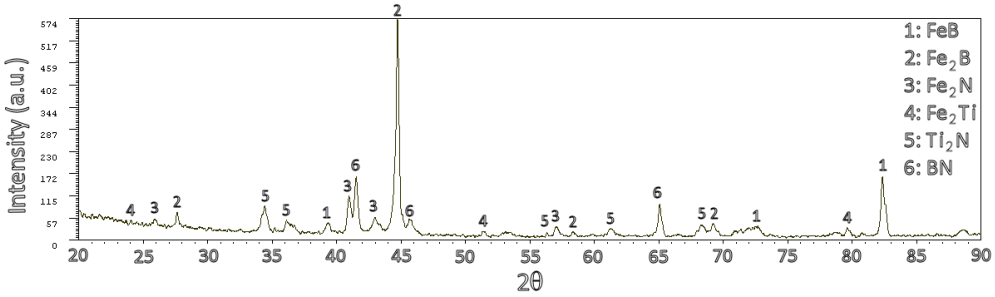

Figure 11. X rays diffraction pattern of the surface of the interstitial-free steel first boronized at 900 °C for 45 min by applying a current density of 0.10 A/cm^2 and then titanium diffused at 1000 °C for 2 hours

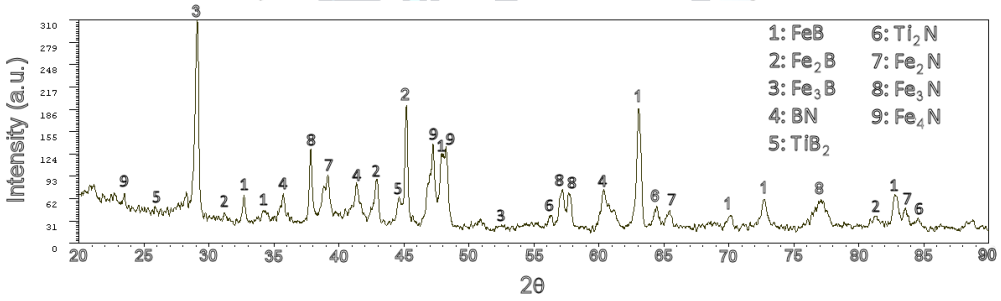

Figure 12. X rays diffraction pattern of the surface of the interstitial-free steel first titanium diffused at 1000 °C for 2 hours and then boronized at 900 °C for 120 min by applying a current density of 0.40 A/cm^2

3.3. Results of Hardness Measurements

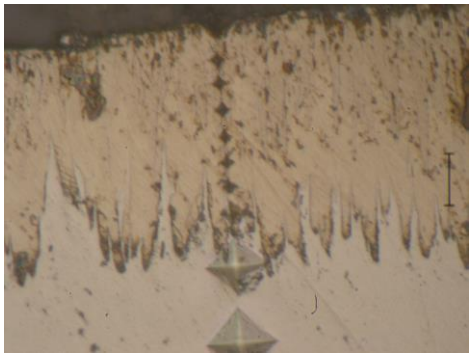

Figure 13. Optical micrograph presenting the difference of hardness between the substrate and the boride layer generated as a result of boronizing (Scale length: 20 µm)

An optical micrograph showing the boride layer generated as a result of boronizing after which Vickers hardness testing was applied is given in Figure 13 in order to present the hardness difference between the boride layer and the substrate considering the size of the indentation traces. The diagram shown in Figure 14 presents the change of hardness with respect to the distance from surface and the applied current density. Two other optical micrographs showing the outer layer of the diffusion coating on the surface of the sample which was first boronized and then titanium diffused are given in Figures 15 (a) and 15 (b). The size of the indentation traces indicates the extremely high hardness of a phase within the titanium based diffusion layer, which was formed as a result of titanium diffusion carried out after boronizing. Hardness values over 4000 HV were detected in this phase.

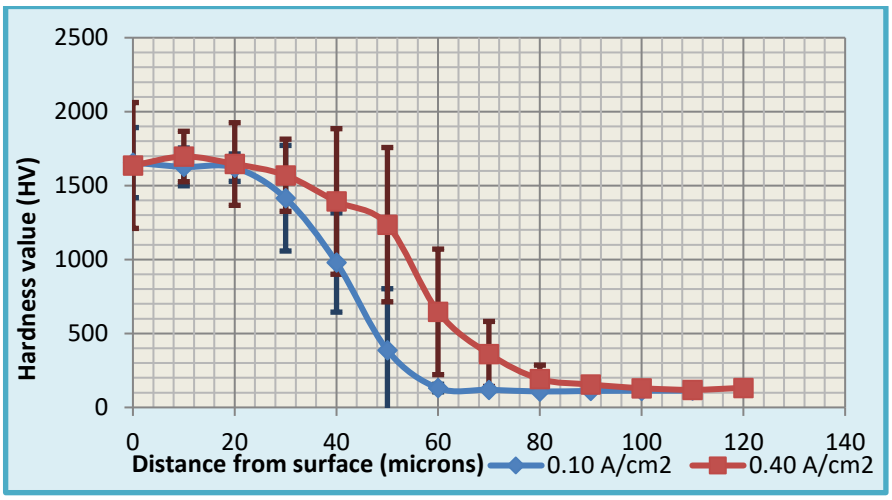

Figure 14. Change of hardness with respect to the distance from surface and the applied current density in case of merely boronizing at 900 °C for 45 min

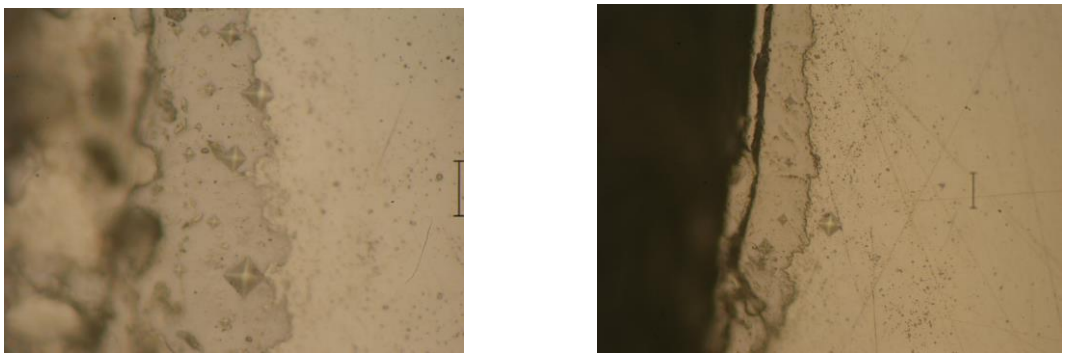

(a) (b)

Figure 15. (a) and (b) The outer layer of the diffusion coating generated as a result of first boronizing and then titanium diffusion. The size of the indentation traces indicates the existence of a very hard phase within the titanium based diffusion layer (Scale length: 20 µm)

3.4. Results of Thermodynamic Calculations

Six chemical reactions were supposed to occur related to titanium diffusion process. They are written on the right side of Figure 16 and the standard formation enthalpies of five of them with respect to temperature are presented in a diagram on the left side of Figure 16. It is already known that the standard formation enthalpy of the first chemical reaction is negative over approximately 380 °C indicating that ammonium chloride decomposes into ammonia and hydrochloric acid [5]. It is concluded that, at normal atmospheric pressure, all of these six chemical reactions can occur at 1000 °C at which titanium diffusion was performed.

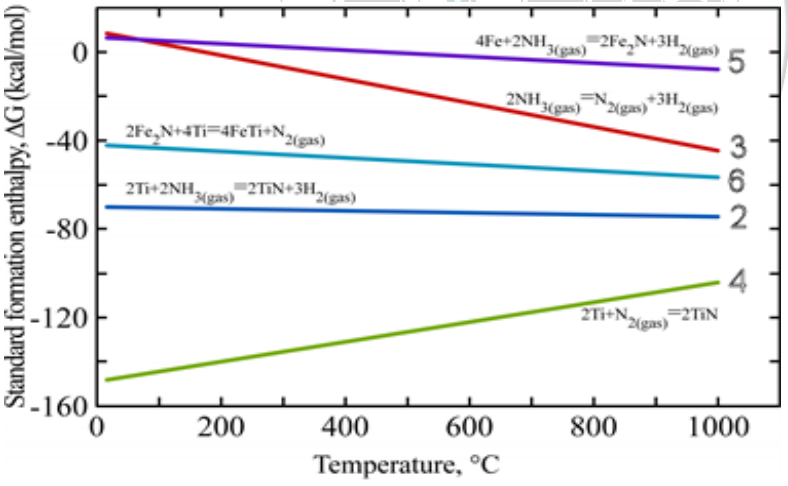

(1) $NH_4Cl=NH_{3(gas)}+HCl$

(2) $2Ti+2NH_{3(gas)}=2TiN+3H_{2(gas)}$

(3) $2NH_{3(gas)}=N_{2(gas)}+3H_{2(gas)}$

(4) $2Ti+N_{2(gas)}=2TiN$

(5) $4Fe+2NH_{3(gas)}=2Fe_2N+3H_{2(gas)}$

(6) $2Fe_2N+4Ti=4FeTi+N_{2(gas)}$

Figure 16. Six chemical reactions assumed to occur during titanium diffusion process and the standard formation enthalpies of five of them with respect to temperature

4. CONCLUSION

In this study, multi-layered diffusion coatings were generated via diffusion of boron and titanium on an interstitial-free steel and the mechanism of titanium diffusion was tried to be revealed by introducing six chemical reactions. Titanium was easily diffused over the already generated boride layer in case of first boronizing and then titanium diffusion, but boron atoms could surpass the already formed titanium based diffusion layer in small quantities only if boronizing duration and the current density applied during boronizing were increased. A metastable phase of Fe_3B was detected in the boride layer, as well as the stable phases of Fe_2B and FeB. Abundance of a very hard phase with a hardness degree of over 4000 HV was determined within the titanium based diffusion layer that was generated over the boride layer.

ACKNOWLEDGEMENTS

The authors would like to acknowledge Ereğli Iron and Steel Works Co. (ERDEMİR) for providing the interstitial-free steel plates and the Office of Scientific Research Projects in Istanbul Technical University for financial support with the project number 34558.

REFERENCES

[1] A. K. Sinha, *Heat Treating: Boriding (Boronizing) of Steels*, ser. ASM Materials Handbook. Materials Park, OH, USA: ASM Int., vol. 4, pp. 978-997, 1995.
[2] J. R. Davis, *Surface Hardening of Steel: Understanding the Basics*: Boriding. Materials Park, OH, USA: ASM Int., pp. 213-226, 2002.
[3] N. Gidikova, "Thermodiffusion Treatment of Steel with Ti Thermodynamics and Phase Composition," *Mater. Sci. & Eng. A*, vol. 222, pp. 84-90, 1997.
[4] K. Dutta and K. K. Ray, "Ratcheting Strain in Interstitial Free Steel," *Mater. Sci. & Eng. A*, vol. 575, pp. 127-135, 2013.
[5] "ID: C1-103 Material Safety Data Sheet: Ammonium Chloride," Chem. One, Houston, TX, USA, 2010.